A Data-Driven Model-Predictive Control Design for Power System Oscillation Damping

A dissertation submitted by

Wenjie Han

In partial fulfilment of the requirements

for the degree of

Doctor of Philosophy

in

Electrical Engineering

TUFTS UNIVERSITY

May 2021

Advisor: Professor Aleksandar M. Stanković

Abstract

In the big picture of smart grids, the wide deployment of smart meters and the development of information and communication technology (ICT) are bound to make vast and increasing quantities of data accessible. Accordingly, data-driven analysis has the potential to revolutionize how the modern power grid is modeled, monitored, and controlled.

The expected tremendous growth of power systems needed to integrate renewable sources, transportation, and storage significantly increases the system complexity and poses challenges on the security and reliability of the power supply. The potential for instability caused by oscillations is one of the key concerns. Conventional power system stabilizers (CPSSs) are widely utilized in modern power systems to provide supplementary damping torque via the excitation system. The parameters of CPSS are determined based on a small set of linearized models around specific operating conditions. This leads to the concern that the damping effects of CPSSs may degrade under a highly dynamic operating environment. The dependency of CPSSs on accurate modeling of the power system is another critical problem since the high-accuracy modeling task is made progressively more challenging in the increasingly distributed power system resources.

This dissertation proposes a data-driven control framework, referred to as ESO-Koopman-MPC (EKM), and presents a novel power system oscillation damping controller design based on this structure. The system dynamics are extracted from the measurements

of the system observables and applied to the synthesis of control actions in an equation-free manner without requiring explicit knowledge about the underlying power network. Dynamic mode decomposition with control (DMDc), based on the Koopman operator theory, connects the collected data to the analysis and control of the underlying nonlinear dynamical system. The discrepancy between the model identified by DMDc and the real plant is labeled as a total disturbance, estimated in real-time by an extended state observer (ESO), and mitigated via a linear MPC, assuming the total disturbance to be constant in the prediction horizon.

The design of the power system oscillation damping controller considers two control strategies, (1) integration of automatic voltage regulator (AVR) and PSS, and (2) only PSS. The data-driven damping controllers are illustrated on a single machine infinite bus system (SMIB), Kundur two-area system, and IEEE 39-bus system, with performances compared with the CPSSs. The simulation results verify the enhanced oscillation damping performances and voltage regulation abilities of the data-driven controllers.

Believe in our unbending striving

Believe in our youth that can conquer death

Believe in the Future: believe in Life.

---- *Shizhi, 1968*

Acknowledgements

Looking back at this moment, I am feeling an upsurge of emotions after studying for more than five years at Tufts. It is not just about an academic degree but great people that make me grow. It is not just about research but everyday life that teaches me to deal with all the good and bad.

First and foremost, my deepest gratitude goes to my advisor, Prof. Stankovic, for his invaluable advice, continuous support, and patience during my PhD study. He always gives me freedom and flexibility to dive into my interest, and whenever I get stuck, he is always there to listen and help. His immense professional knowledge and positive attitude have encouraged me in both my academic research and daily life. It is a great honor to work with him, and I will benefit from these experiences for my whole life.

I would also like to thank all the committee members, Prof. Andrija Sarić from the University of Novi Sad, Serbia, Prof. Usman Khan from ECE, and Prof. Eric Hines, from Civil and Environmental Engineering. Their suggestions and insightful comments inspire this dissertation and open our minds to think about potential applications.

Additionally, I would like to express gratitude to my colleagues, Dr. Clifford Youn, Dr. Gang Wang, Dr. Vanja Svenda, and Alex Sarić, for their helpful suggestions and discussions. I will never forget Boyang Lyu, Qiong Cao, Jie Yuan, and all my friends at Tufts for their accompany, help, and encouragement. Besides, I would also thank Miriam

Santi and George Preble for their life care, who I will turn to whenever I have any difficulties.

My appreciation also goes out to my family for their encouragement and support all through my studies. My parents, Shunjun Han and Xuemei Wang, give me unreserved love no matter when I made progress or mistakes. They are always there to listen, to comfort, to encourage, to make me strong again. Due to the characteristics of time, my parents do not have the opportunities for college educations. My education is their expectation and dream. Mom and Dad, I love you forever.

I am grateful to be such a lucky person surrounded by loving and great people. If I have any achievement, it also belongs to all of you.

Wenjie Han

May, 2021

Tufts University

Contents

List of Tables

List of Figures

Chapter 1

Chapter 2

Chapter 3

Chapter 4

Chapter 5

Chapter 1

Introduction

With the rapid development of the smart grid, the embedded information layer into the power network produces a massive amount of data, including measurements of the system observables and the control actions for generation, transmission, storage, and analysis in a fast and comprehensive way. In other words, modern power system technology comes into a big data era. The access to large quantities of data and the remarkable progress of information and communication technology (ICT) provides a new vision for power system monitoring and control.

In our work, a data-driven control framework is proposed and applied in the power system oscillations damping. The control framework involves,

- the dynamical system identification,
- online disturbance estimation, and
- a model predictive control (MPC) structure.

Different from the conventional workflow of controller design, the novel framework is in an “equation-free” manner and has the ability of online learning and self-adaption. For

cases where exact modeling is challenging, big data motivates the paradigm shift from a "model-based" to a "data-driven" perspective.

1.1 Research Background: The Big Data Era of Power Systems

The deployment of ICT in power systems makes an abundant source of information accessible, which covers the data from the process of electricity generation, transmission, distribution, and consumption. The data include electrical information from distribution stations, transmission lines, measurement devices, as well as non-electrical information such as regional economic management data, meteorological and marketing data, as shown in Figure 1-1.

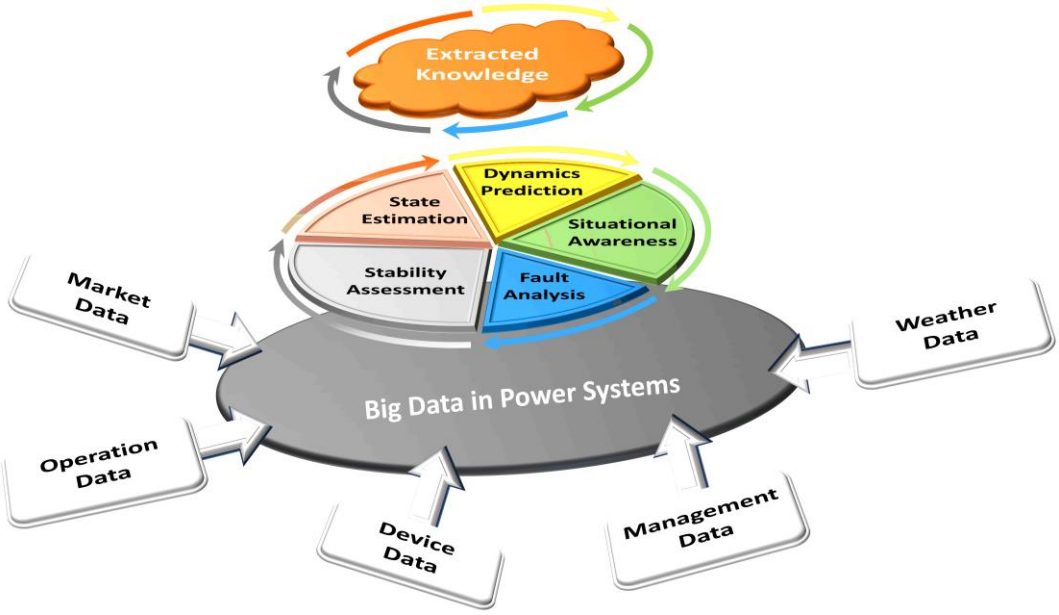

Figure 1 - 1 Data Sources and Analytics in Smart Grids

1.1.1 Data Collection Devices in Power Systems

The data in power systems are collected and transmitted by smart meters to provide information to utility companies, independent system operators (ISO), and consumers. The

measurements include the bus voltage, feeder current, power factor, active/reactive power flow, energy consumption over a period and total harmonic distortion, etc.

Smart meters involve but are not limited to the following list:

- **Advanced Metering Infrastructure (AMI):** AMI integrates smart meters, data management, and communication to provide bidirectional communication between the supply and demand side.
- **Phasor Measurement Unit (PMU):** PMUs provide real-time measurements in a sample rate of 30~60 samples/sec of multiple remote spots with global time synchronization.
- **Wide Area Monitoring System (WAMS):** WAMS is an application server to manage the information of distributed PMUs.
- **Remote Terminal Unit (RTU):** RTU is a microprocessor-based device that can transmit telemetry data.
- **Supervisory Control and Data Acquisition (SCADA):** SCADA provides system monitoring and emergency alarms.
- **Intelligent Electronic Device (IED):** IED monitors and records status changes in the substation and outgoing feeders.

1.1.2 The Characteristics of Big Data in Power Systems

The characteristics of the big data in power systems are in accordance with the universal *5V* big data model [1],

(a) Volume: The widespread application of smart meters and advanced sensor technology provide a considerable amount of data.

(b) Velocity: With the increasing sampling frequency of smart meters, the speed of data generation is growing. Table 1-1 demonstrates the amount of data from smart meters in a year under various collection frequencies, assuming 1 million devices and a 5 KB record per collection [2].

Table 1-1 Data Volume in Different Sampling Rates

Collection Frequency	1/day	1/h	1/30 min	1/15 min
Records Collected	365 million	8.75 billion	17.52 billion	35.04 billion
Volume of Data	1.82 TB	730 TB	1460 TB	2920 TB

(c) Variety: The diversity of data types in power systems is reflected in formats and dimensions; see Figure 1-1.

(d) Veracity: Veracity refers to the messiness or trustworthiness of data. The power system is tightly coupled with the ICT layer, forming a cyber-physical system (CPS). Measurements may contain errors and noises due to the imperfections in devices or mistakes in data transmission, i.e., communication delay [3], packet drop, etc.

(e) Value: The larger the data volume is, the lower the density of valuable information contained is.

1.2 Perspective Shift: Data-Driven Controller Design

As displayed in Figure 1-1, data-driven applications in power systems are developed by extracting valuable information from measurements, such as fault detection [4, 5, 6], predictive maintenance/condition-based maintenance and alarm [7, 8], transient stability analysis [9, 10, 11], state estimation [12], power quality monitoring [13], topology

identification [14], renewable energy and load forecasting [15, 16] and other areas such as load profiling, load disaggregation, non-technical loss detection; see [2] for a review.

This dissertation focuses on developing a data-driven control framework without any pre-knowledge about the underlying dynamics. If any known dynamics that partially describe the process to be controlled exist, the proposed data-driven framework has an interface to incorporate and leverage such pre-knowledge. The overall data-driven controller design workflow is shown in Figure 1-2.

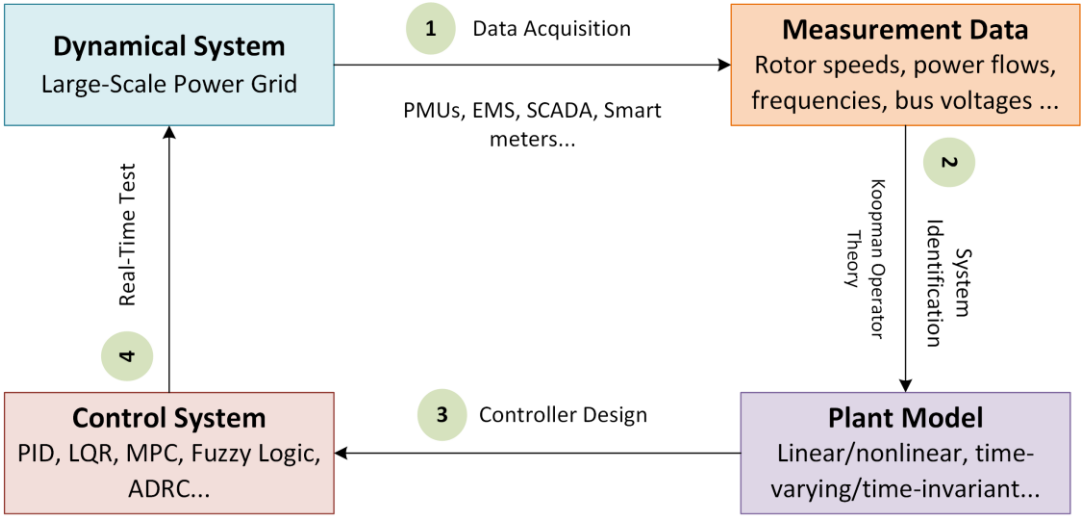

Figure 1 - 2 Workflow of Data-Driven Controller Design

1.2.1 Motivations of Data-Driven Controller Design

With a large-scale power system as an example, the dynamical system is intrinsically high-dimensional, nonlinear, and time-varying. We summarize three key factors that motivate the novel data-driven controller design in power system applications.

A. Power System Modeling Challenges

The following list draws out the main modeling challenges of power systems [17],

- Penetration of Renewable Energy Sources (RESs): The outputs of RESs are uncertain and intermittent.
- Distributed Generation Sources (DGS): DGSs are connected to distribution networks, right down to the level of individual homes, which results in two-way power flows that pose challenges to the operation of local networks.
- Component (particularly load) Variations
- Undocumented Alternations/Obsoleteness
- Models Existing only in the Form of Tabulated Data or Computer Code: A typical example is the application of advanced control and automation.
- Demand Response by Consumers: The consumers are offered increased flexibility to use smart appliances, for example, to align more closely with the output from intermittent RESs.
- Inter-Dependency of the Power Network and the ICT Infrastructure: The conventional modeling pays far more attention to the power grid than the communication network.

B. Bia Data in Power System

The big data era of power systems discussed in the last section provides large quantities of data, which is the backbone of data-driven technologies.

C. Development of Data-Driven Analytics

The history of data-driven discovery can be dated back to Johannes Kepler and Isaac Newton. The theoretical underpinnings of the celestial mechanics were developed based on a combination of empirical data-driven and analytical approaches. Data science is not replacing mathematical modeling but instead an augmenting tool in real applications.

The data science concept is dominated by two distinct outlooks: the machine learning community and the statistical learning community. From the viewpoint of controller design, the goal is to leverage the broad techniques to infer and compute models from observations. The identified model is expected to describe the measured dynamics accurately and can be generalized qualitatively and quantitively to the unmeasured parts in a wide working range.

1.2.2 Procedures of Data-Driven Controller Design

As shown in Figure 1-2, procedures of the data-driven controller design are,

Step 1: Dynamical Data Acquisition

Dynamical data in this dissertation is from numerical simulation of detailed power system models in Simulink. Short-time disturbances that are easy to be implemented in practice are exerted on the dynamical system to excite transients, and dynamical data is collected in the post-disturbance period. The measured variables are limited to observables available in the power system monitoring system.

Step 2: **Dynamical System Identification**

The dynamical system identification from the collected data depicts how the system states evolve and the impact of the forced controls on the system outputs, especially those target variables that we are interested in. The Koopman operator-based approach, dynamic mode decomposition with control (DMDc) introduced in Chapter 2, is applied in our work at this step. The quality and accuracy of the identified system are verified in terms of the system trajectory prediction performance.

Step 3: **Controller Design**

The approach of controller design depends on the format of the identified dynamical system. Owing to the linearity of the Koopman operator, the system identified by DMDc is linear and thus allows mature linear design techniques to be applied in highly nonlinear and complicated processes underlying.

Step 4: Control Performance Test and Analysis

The control performances of the data-driven oscillation damping controller and the model-based conventional power system stabilizer (CPSS) are compared on various test platforms, recommended by IEEE Task Force, in this dissertation.

1.3 Contributions

The contributions of this dissertation are summarized as:

- **Proposed a Data-Driven Control Framework**

This dissertation proposed a completely data-driven control framework, referred to as Extended State Observer-Koopman-Model Predictive Control (EKM); see Chapter 4. This control framework contains system dynamics extraction from the collected data, model-plant mismatch estimation and self-compensation by the extended state observer (ESO), and controller design in the MPC architecture. The control framework is not fixed, and the three basic components (1) Koopman operator-based system identifications, (2) ESO, and (3) MPC can be replaced by other appropriate techniques. For example, the controller design can follow the linear quadratic regulator (LQR), fuzzy-logic control, or other schemes.

- **Introduced ESO to Realize Online Disturbance Estimation**

The dynamical system identified from the collected data generally has prediction deviation from the true dynamics. The model-plant mismatch may derive from the limitations of identification approaches, data homogeneity, sensor noises, or the underlying system variations (parameter, external disturbance, etc.). An ESO is introduced to estimate the discrepancy between the identified model and the real plant from the system inputs and outputs measurements. The dynamics learned by DMDc are incorporated into the ESO design to reduce the estimation burden; see 3.4.2 Multi-Channel ESO.

The estimated discrepancy is then used to adaptively update the predictive model in the MPC structure in a real-time manner. The discrepancy is assumed to be constant in the MPC prediction horizon and compensated accordingly.

- **Designed Data-Driven Power System Oscillation Damping Controllers**

Power system oscillation damping controllers are designed following the proposed data-driven control framework, ESO-Koopman-MPC. To the best of our knowledge, this is the first time that a data-driven controller design is applied to the power system oscillation damping. The design takes some practical considerations into account, i.e., observables selection, dynamical data collection, control strategies of integration of automatic voltage regulator (AVR) & PSS and only PSS, etc. The data-driven damping controller is compared with CPSS on different-scale platforms. The damping effects of critical oscillatory modes and the terminal voltage regulation abilities of the EKM-based controllers are superior under various scenarios.

This dissertation has a conference paper [18] published and a journal paper still under peer-review [19]. Besides, the author also has publications [3, 20] on the power system

frequency control considering the communication delays, where active disturbance rejection control (ADRC) is applied to the automatic generation control (AGC). The core component, ESO, in ADRC inspires the estimation of the model-plant mismatch in this dissertation.

1.4 Work Outline

The remainder of this dissertation is organized as follows:

- Chapter 2 provides basics about the Koopman operator theory and two commonly used numerical approximation methods: Arnoldi-type method and dynamic mode decomposition with control (DMDc).
- Chapter 3 introduces ESO in both the nonlinear and linear format. Multi-channel ESO is proposed leveraging the dynamics identified by the DMDc to reduce the estimation burden in a linear form.
- Chapter 4 reviews the MPC theory first and proposes the ESO-Koopman-MPC (EKM) control framework. The online algorithm of EKM is presented in the last subsection.
- Chapter 5 describes the formulation of a data-driven oscillation damping controller with two control strategies considered: (1) integration of AVR and PSS; (2) only PSS. Simulation results of data-driven controllers on platforms of different scales are displayed and compared with CPSSs. At the end of this chapter, some discussions about ESO and the characteristics of the control framework are presented.
- Chapter 6 summarizes this dissertation and points out some directions to be explored in the future.

Chapter 2

Koopman Operator Theory

Past decades have witnessed significant advances and achievements in the development of the nonlinear dynamical system theory. Despite the intense research activity at a theoretical level, nonlinear system theory and control techniques have not been applied to real-world applications as much as hoped. In contrast, linear control theory still prevails the industrial processes since it provides a systematic framework that is often easy to be implemented. The gap between the theory and the practice generally results in suboptimal control to nonlinear problems and might not meet the growing demand for higher control performances or improved accuracy.

Additionally, the increasing complexity and diversity of the dynamical systems make the classical system modeling and the corresponding model-based control not amenable. However, these dynamical systems generate large quantities of data, motivating the development of innovative data-driven methods in nonlinear control theory. The Koopman operator introduced in this chapter offers a promising way to address the challenges mentioned above.

In this chapter, an overview of the Koopman operator in the context of dynamical systems and control theory is provided first, involving the basic definitions, properties, and

spectral analysis. Then, numerical methods to obtain approximations of the Koopman operator on a finite-dimensional basis are presented, and we mainly focus on two widely used algorithms: Arnoldi-type method and dynamic mode decomposition (DMD) with control (DMDc).

2.1 Data-Driven Viewpoint and the Koopman Operator

Koopman operator can be traced back to the seminal works by Koopman and von Neumann in the 1930s [21, 22]. This operator-theoretic perspective showed that nonlinear dynamical systems associated with Hamiltonian flows could be analyzed with an infinite-dimensional linear operator on the Hilbert space of observable functions. Although this composition operator has attracted considerable interest in statistical mechanics, its dual transfer operator, the Perron-Frobenius operator, has predominated in nonlinear systems theory for a long time.

Until the middle 2000s, the Koopman operator theory was revisited by Mezic in [23], and since then, Koopman analysis has been at the focus of recent data-driven efforts to characterize complex systems. Numerical approximation methods are proposed to compute the spectrum of the Koopman operator from data. In addition, the Koopman operator approach has been successfully applied to a wealth of real-world problems ranging from fluids dynamics, power grids, epidemiology to financial markets; the reader is referred for an extensive review in [24]. Overall, the Koopman operator theory is quite appealing to develop data-driven control schemes in the big data era.

2.1.1 Definition and Properties of the Koopman Operator

Koopman operator can be defined in both discrete-time systems (nonlinear dynamic map) and continuous-time systems (semigroups of flow maps).

- **Discrete-time Dynamical Systems**

Consider a discrete-time dynamical system represented as

$$x_{k+1} = T(x_k), \quad k \in \mathbb{Z} \tag{2-1}$$

where $x_k \in \mathfrak{M} \subseteq \mathbb{R}^n$ is the state sampled at $t_k = k\Delta t$ with sampling time Δt, and $T : \mathfrak{M} \to \mathfrak{M}$ is the nonlinear dynamic map. The system is typically described by its orbits $\{T^k(x_0)\}_{k=0}^{\infty}$, where x_0 stands for the initial condition.

Definition 2.1 Koopman Operator (Discrete-Time) For an arbitrary function of the states (observable) $g(x) : \mathfrak{M} \to \mathbb{C}$, there exists an infinite-dimensional linear operator $\mathrm{K}_{\Delta t}$ acting on the space $\wp$ of observable functions and advancing g to the next time step,

$$\mathrm{K}_{\Delta t} g(x_k) = g \circ T(x_k) = g(x_{k+1}), \quad \forall \mathrm{g} \in \wp \tag{2-2}$$

The Koopman operator embodies two main advantages. First, the Koopman operator provides a global description of nonlinear dynamical systems in terms of the evolution of observables. Second, the Koopman operator is a linear operator even though the underlying dynamical system is highly nonlinear, and the linearity is proved from the linearity of the composition operation, i.e.,

Linearity**:** Consider $\forall g_1, g_2 \in \wp, c_1, c_2 \in \mathbb{C}$

$$\begin{aligned} \mathrm{K}_{\Delta t}(c_1 g_1 + c_2 g_2)(x_k) &= (c_1 g_1 + c_2 g_2) \circ T(x_k) = c_1 g_1 \circ T(x_k) + c_2 g_2 \circ T(x_k) \\ &= c_1 \mathrm{K}_{\Delta t} g_1(x_k) + c_2 \mathrm{K}_{\Delta t} g_2(x_k) \end{aligned} \tag{2-3}$$

However, unless the function space $\wp$ is a finite set, the Koopman operator is generally infinite-dimensional, which makes the direct utilization of the Koopman operator unrealistic. Follow-up research efforts try to reduce the dimensionality by a finite-dimensional projection of the Koopman operator onto appropriate eigenspace.

- **Continuous-time Dynamical Systems**

In this case, we consider a continuous-time dynamical system $\dot{x} = f(x)$, and $f : \mathfrak{M} \to \mathbb{R}^n$ is a vector field on the state space. The flow map $F^t : \mathfrak{M} \to \mathfrak{M}$ transforms the initial state to the state at time $t \in \mathbb{R}^+$, i.e.,

$$F^t(x_0) = x_0 + \int_{x_0, \tau=0}^{t} f(x(\tau))d\tau = x_t \tag{2-4}$$

The one-parameter family of flow maps F^t generates the trajectory $\{F^t(x_0)\}_{t=0}^{\infty}$.

Definition 2.2 Koopman Operator (Continuous-Time) For an arbitrary function of the states (observable) $g(x) : \mathfrak{M} \to \mathbb{C}$, there exists a one-parameter semi-group of Koopman operators, denoted by $\{U^t\}_{t\geq 0}$, where each element in this semi-group satisfies

$$U^t g(x_{t_0}) = g \circ F^t(x_{t_0}) = g(x_{t_0+t}), \quad \forall g \in \wp \tag{2-5}$$

The linearity of the Koopman operator in the continuous-time case is still valid. The semi-group property of $\{U^t\}_{t\geq 0}$ follows from the semi-group property of the flow map in autonomous dynamical systems,

Semi-group property:

$$\begin{aligned} U^t U^s g(x) &= U^t g \circ F^s(x) = g \circ F^s \circ F^t(x) = g \circ F^{s+t}(x) \\ &= U^{s+t} g(x) \end{aligned} \tag{2-6}$$

A schematic representation of the Koopman operator is shown in Figure 2-1. The Koopman operator viewpoint maps (lifts) the dynamics from the original state-space to the space of observables, where the evolution rule is linear. In other words, the discrete-time or continuous-time dynamical system modeling T, f, F^t and the corresponding Koopman operators $K_{\Delta t}, U^t$ are different description formats of the same dynamics. The model-based T, f, F^t are generally finite-dimensional but nonlinear, while the data-driven operators $K_{\Delta t}, U^t$ are infinite-dimensional but linear.

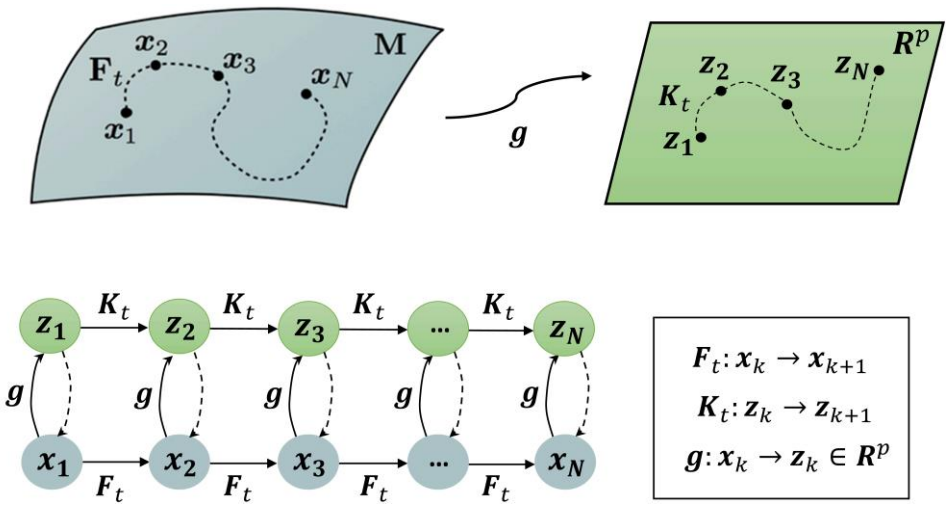

Figure 2- 1 Schematics of the Koopman Operator

Other properties of the Koopman operator, e.g., positivity, contractivity, and duality, are elaborated in [24]. Besides, some specific characteristics of the Koopman operator may depend on the choice of the state function space $\wp$. For example, in measurement-preserving dynamical systems, the Hilbert space of L^2 functions with respect to the invariant measures is usually considered as the function space. In this case, the Koopman operator is unitary with $UU^* = I$ (the "U" notation comes from this unitary property).

2.1.2 Spectral Analysis of the Koopman Operator

As discussed in the last section, the Koopman operator is linear. Thus, it is natural to consider its eigenvalues and eigenfunctions since they reveal a linear explanation of how the system observables evolve.

Definition 2.3 Eigenfunction and eigenvalue of the Koopman Operator $K_{\Delta t}$ (Discrete-time) A pair of eigenfunction $\varphi_j(x) \in \wp \backslash \{0\}$ and eigenvalue $\lambda_j \in \mathbb{C}$ of the Koopman operator $K_{\Delta t}$ associated with the discrete-time dynamic map T satisfies

$$K_{\Delta t}\varphi_j(x_k) = \varphi_j \circ T(x_k) = \varphi_j(x_{k+1}) = \lambda_j \varphi_j(x_k) \tag{2-7}$$

Example 2.1: Linear Time-Invariant System (Discrete-time)

A LTI system is considered with the state map $T(x) = Ax$, where A is the system matrix with eigenvalues λ_j and left (column) eigenvectors w_j with $w_j^T A = \lambda_j w_j^T$. Therefore, $\varphi_j(x) = w_j^T x$ and λ_j are a pair of eigenfunction and eigenvalue. The verification is as follows,

$$K_{\Delta t}\varphi_j(x) = \varphi_j \circ T(x) = w_j^T Ax = \lambda_j w_j^T x = \lambda_j \varphi_j(x) \tag{2-8}$$

Definition 2.4 Eigenfunction and eigenvalue of the Koopman Operator U^t (Continuous-time) The eigenfunction-eigenvalue pair of the continuous-time case associated with the flow map F^t is defined as follows

$$U^t \varphi_j(x) = \varphi_j \circ F^t(x) = e^{\lambda_j t}\varphi_j(x) \tag{2-9}$$

The Koopman operator generally has infinite eigenvalue-eigenfunction pairs. First, we assume all eigenvalues form a point spectrum. For the discrete-time case, if φ_1, φ_2 are eigenfunctions of the Koopman operator $K_{\Delta t}$ whose eigenvalues are λ_1, λ_2, then $\varphi_1^{c_1}\varphi_2^{c_2}$ is

also an eigenfunction with the eigenvalue $\lambda_1^{c_1}\lambda_2^{c_2}, \forall c_1, c_2 \in \mathbb{R}$. Similarly, in the continuous-time setting, eigenfunction $\varphi_1^{c_1}\varphi_2^{c_2}$ has the corresponding eigenvalue $c_1\lambda_1 + c_2\lambda_2$. On the other side, the Koopman operator may also admit a continuous spectrum such as the pendulum dynamics and some chaotic systems [25].

Eigenfunctions of the Koopman operator are a set of crucial measurement functions that behave linearly in the time domain and provide the basis for Koopman mode decomposition (KMD). When the system dynamics are integrable and defined in a compact space, the infinite set of Koopman eigenfunctions provides a complete basis of the function space $\wp$. Therefore, the Koopman mode expansion of $g \in \wp$ is expressed by

$$g = \sum_{j=1}^{\infty} v_j \varphi_j \tag{2-10}$$

The coefficients v_j are the Koopman modes related to the observable g.

In practice, the measurements of a dynamical system usually contain multiple observables. For example, we may have access to the time series of power generations and consumptions on several nodes in a specified power grid, or in the study of climate dynamics, there exist many recording stations of the atmospheric temperature at different locations around the globe. A vector-valued observable is denoted as

$$\vec{g}(x) = \begin{bmatrix} g_1(x) \\ g_2(x) \\ \vdots \\ g_p(x) \end{bmatrix} \in \mathbb{R}^p \tag{2-11}$$

Koopman mode expansion is then applied on each element $g_i, i = 1, 2, ..., p$, and we have $\vec{g} = \sum_{j=1}^{\infty} \vec{v}_j \varphi_j$. The vector $\vec{v}_j$ is the Koopman mode of the observable vector associated to

the eigenfunction φ_j. The evolution of the vector-valued measurements for a discrete-time system is thus governed by

$$K_{\Delta t}^k \vec{g}(x) = \sum_{j=1}^{\infty} K_{\Delta t}^k \varphi_j(x)\vec{v}_j = \sum_{j=1}^{\infty} \lambda_j^k \varphi_j(x)\vec{v}_j \tag{2-12}$$

Similarly, we have

$$U^t \vec{g}(x) = \sum_{j=1}^{\infty} U^t \varphi_j(x)\vec{v}_j = \sum_{j=1}^{\infty} e^{\lambda_j t} \varphi_j(x)\vec{v}_j \tag{2-13}$$

for continuous-time systems. Koopman mode $\vec{v}_j$ is the projections of the observable functions on the eigenfunction φ_j. The expansions in (2-12) and (2-13) are referred to as the Koopman mode decomposition (KMD). The linear dynamics offer a global linearization of nonlinear systems with no approximation.

The spectral analysis of the Koopman operator reveals characteristics of the underlying dynamics. Considering an example of the power network, the system instabilities can be connected to the Koopman eigenvalues growing in time, that is $\lambda_j > 0$ for continuous-time or $|\lambda_j| > 1$ for discrete-time. Besides, the entries of the Koopman mode $\vec{v}_j$ tell the relative amplitude of each node in terms of the unstable growth and hence predict which nodes are most susceptible to breakdown.

Example 2.2 Nonlinear system with single fixed point and a slow manifold

To further illustrate the concept of the Koopman operator and the Koopman linear expansion, we consider an example [26] with a single fixed point,

$$\begin{aligned} \dot{x}_1 &= \mu x_1 \\ \dot{x}_2 &= \lambda(x_2 - x_1^2) \end{aligned} \tag{2-14}$$

For $\lambda < \mu < 0$, the system exhibits a slow attracting manifold given by $x_2 = x_1^2$. System trajectories with randomly initialized states are shown in Figure 2-2, where $\lambda = -1, \mu = -0.05$.

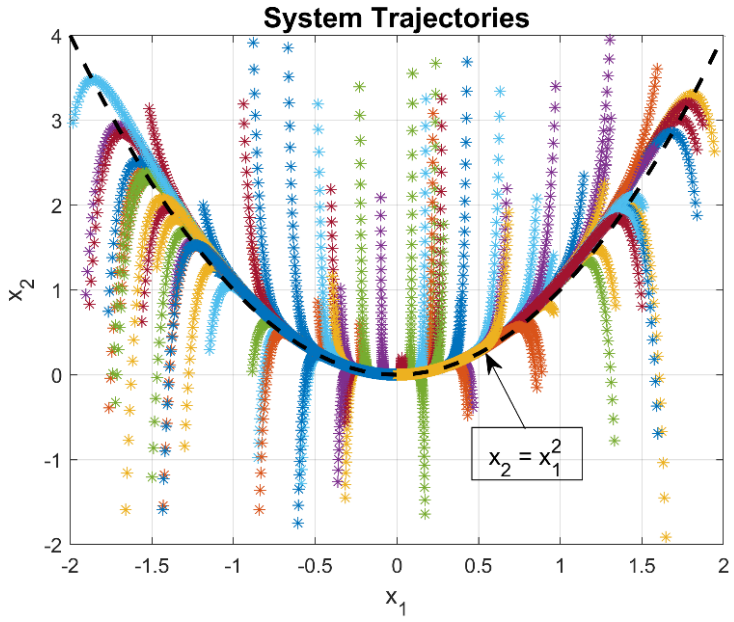

Figure 2-2 States Trajectories of the Nonlinear System in Example 2.2

The system measurements are assumed to be $\vec{g}(x) = [x_1, x_2, x_1^2]$ with a nonlinear augmented function (observable) x_1^2. In these coordinates, the dynamics of (2-14) becomes linear, shown below.

$$\frac{d}{dt}\vec{g}(x) = \begin{bmatrix} \dot{x}_1 \\ \dot{x}_2 \\ 2x_1\dot{x}_1 \end{bmatrix} = \begin{bmatrix} \mu x_1 \\ \lambda(x_2 - x_1^2) \\ 2\mu x_1^2 \end{bmatrix} = \begin{pmatrix} \mu & 0 & 0 \\ 0 & \lambda & -\lambda \\ 0 & 0 & 2\mu \end{pmatrix} \vec{g}(x) \tag{2-15}$$

The system matrix has left eigenvectors $\xi_1 = [0, -\frac{\lambda - 2\mu}{\lambda}, 1], \xi_2 = [1,0,0], \xi_3 = [0,0,1]$ and eigenvalues $\lambda, \mu, 2\mu$. The eigenfunctions correspond to eigenvalues λ, μ are

$$\varphi_\lambda = -\frac{\lambda - 2\mu}{\lambda} x_2 + x_1^2, \varphi_\mu = x_1 \tag{2-16}$$

The evolution trajectories of the eigenfunctions in (2-16) are displayed in Figure 2-3, where the slow manifold becomes flat. All eigen-observables define a subspace that remains invariant under the Koopman operator. In other words, the system matrix in (2-15) represents a finite-dimensional approximation of the Koopman operator. The selection of observables, in this case, is very clever but is not always easy for an arbitrary dynamical system. Ref. [27] leverages neural networks to discover representations of the Koopman eigenfunctions from data. Actually, the nonlinear system (2-14) is one of few dynamical systems for which a closed and finite-dimensional Koopman approximation exists and can be found analytically.

2.1.3 Koopman with Inputs and Control

Although the Koopman operator was initially proposed to study autonomous dynamical systems, a generalization called Koopman with inputs and control (KIC) [60] is extended to handle complex systems with external inputs. In this section, a discrete-time case is studied, i.e.,

$$x_{k+1} = f(x_k, u_k) \tag{2-17}$$

where $u_k \in \mathrm{N} \subseteq \mathbb{R}^m$.

We construct an augmented state space as the product of the original state space and the space of all control input sequences,

$$x^{Aug} = \begin{bmatrix} x \\ \mathcal{U} \end{bmatrix} \tag{2-18}$$

where $x^{Aug} \in \mathfrak{M} \times \ell(\mathrm{N})$ and $\ell(\mathrm{N})$ stands for the space of all control sequence $(u_i)_{i=0}^{\infty}, u_i \in \mathrm{N}$. The element in $\ell(\mathrm{N})$ is denoted as $\mathcal{U}$. Therefore, the dynamics in (2-17) can be rewritten as

$$x_{k+1}^{Aug} = \mathcal{F}(x_k^{Aug}) := \begin{bmatrix} f(x_k, \mathcal{U}(0)) \\ \mathcal{S}\mathcal{U} \end{bmatrix} \tag{2-19}$$

where $\mathcal{S}$ is a left shift operator, i.e. $(\mathcal{S}\mathcal{U})(i) = \mathcal{U}(i+1)$, and $\mathcal{U}(0)$ is the first element in the control sequence $\mathcal{U}$, [61]. Koopman operator is thus defined for the following skew product system,

$$\big(f\big(x, \mathcal{U}(0)\big), \mathcal{S}\mathcal{U}\big): \mathfrak{M} \times \ell(\mathrm{N}) \to \mathfrak{M} \times \ell(\mathrm{N}) \tag{2-20}$$

as follows

$$\mathcal{K}_{\Delta t} g(x_k^{Aug}) = g \circ \mathcal{F}(x_k^{Aug}) = g(x_{k+1}^{Aug}) \tag{2-21}$$

for any observable function $g: \mathfrak{M} \times \ell(\mathrm{N}) \to \mathbb{C}$ defined on the augmented space.

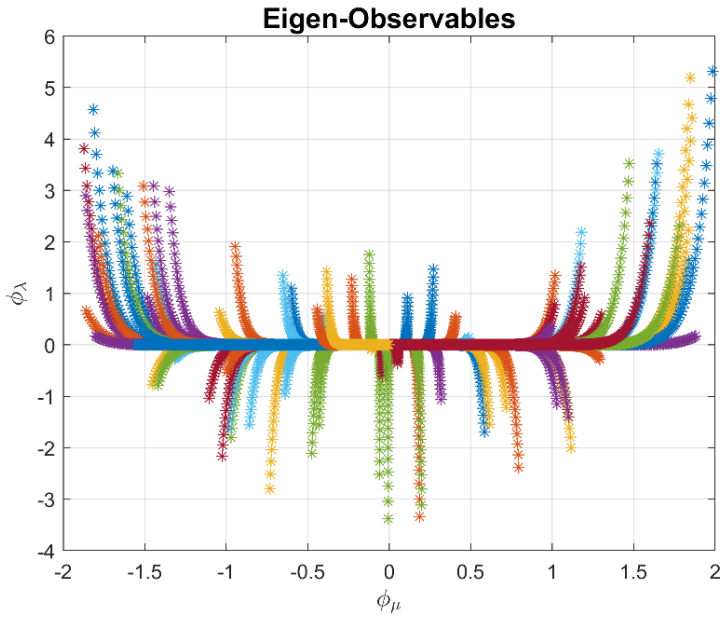

Figure 2- 3 Eigen-observables Trajectories of the Nonlinear System in Example 2.2

In the context of KIC, the definition of eigenvalues, eigenfunctions and Koopman modes are similar to the case without external control.

2.2 Finite-Dimensional Approximation of the Koopman Operator

The Koopman operator offers a global linearization viewpoint that has the potential to revolutionize how we analyze, predict, and control nonlinear dynamical systems. The traditional local linearization of nonlinear dynamics near fixed points or periodic orbits has long been employed, but its validness is questionable far away from the fixed points and periodic orbits.

The main obstacle of the application of the Koopman operator is the infinite dimensionality. Several data-driven methods to approximate the spectral properties of the underlying dynamics have emerged to resolve this issue, and this research area keeps receiving great attention and working efforts. The numerical approximation methods can be generally classified into two types [24]:

(1) Methods aiming to obtain a finite-dimensional matrix approximation of the Koopman operator such as (extended) dynamic mode decomposition (E)DMD, [28, 29]. Recently, ref. [27, 30] leverages the power of deep learning to discover eigenfunctions or the invariant subspaces, releasing the typical EDMD from the cumbersome search of appropriate lifting functions.

(2) Methods based on generalized Laplace averages (GLA) [31, 32]. Such methods first seek an approximation of the Koopman eigenvalues and then use the projection theorem to obtain eigenfunctions and Koopman modes.

A summary of the development of numerical methods to approximate the Koopman operator can be found in [33]. This section introduces two commonly used numerical methods: Arnoldi-type algorithm and SVD-enhanced DMD (with control) algorithm.

2.2.1 Arnoldi-Type Method

The Arnoldi-type algorithm presented in [34] constructs a companion matrix based on the observable data sampled along a trajectory of the system and attempts to approximate the Koopman operator, utilizing Krylov subspaces of the state-space. Suppose we have finite sampled snapshots of the dynamical system in (2-1)

$$Z = \begin{bmatrix} | & | & & | \\ z_0, & z_1, & .., & z_{N-1} \\ | & | & & | \end{bmatrix} \in \mathbb{R}^{p \times N} \tag{2-22}$$

where $z_k = \vec{g}(x_k) \in \mathbb{R}^p$ is the k[th] snapshot of the states $x_k = T^k(x_0)$, and N is the total number of the collected snapshots. The Koopman modes (empirical Ritz vectors) and eigenvalues (empirical Ritz values) can be approximated following the procedures below.

Arnoldi Algorithm:

Step 1: Compute a constant vector $c = [c_0, c_1, ..., c_{N-2}]^T$ such that for some $r \in \mathbb{R}^p$ satisfying $r \perp span\{K_{N-1}\}$,

$$r = z_{N-1} - K_{N-1}c \tag{2-23}$$

with the Krylov subspace defined as

$$K_{N-1} := [z_0, z_1, .., z_{N-2}] \tag{2-24}$$

The constant vector c is computed by

$$c = K_{N-1}^{\dagger} z_{N-1} \tag{2-25}$$

where $K_{N-1}^{\dagger}$ stands for the Moore-Penrose pseudoinverse of K_{N-1}.

Step 2: Define the companion matrix C_{N-1} as

$$C_{N-1} \coloneqq \begin{pmatrix} 0 & 0 & \cdots & 0 & c_0 \\ 1 & 0 & \dots & 0 & c_1 \\ 0 & 1 & \dots & 0 & c_2 \\ \vdots & \vdots & \ddots & \vdots & \vdots \\ 0 & 0 & \dots & 1 & c_{N-2} \end{pmatrix} \tag{2-26}$$

The N-1 eigenvalues of C_{N-1} are empirical Ritz values $\tilde{\mu}_1, \tilde{\mu}_2, ..., \tilde{\mu}_{N-1}$.

Step 3: Define the Vandermonde matrix $\mathfrak{T}$ using $\tilde{\mu}_1, \tilde{\mu}_2, ..., \tilde{\mu}_{N-1}$

$$\mathfrak{T} \coloneqq \begin{bmatrix} 1 & \tilde{\mu}_1 & \tilde{\mu}_1^2 & \cdots & \tilde{\mu}_1^{N-2} \\ 1 & \tilde{\mu}_2 & \tilde{\mu}_2^2 & \dots & \tilde{\mu}_2^{N-2} \\ \vdots & \vdots & \vdots & \ddots & \vdots \\ 1 & \tilde{\mu}_{N-1} & \tilde{\mu}_{N-1}^2 & \dots & \tilde{\mu}_{N-1}^{N-2} \end{bmatrix} \in \mathbb{R}^{(N-1)\times(N-1)} \tag{2-27}$$

Step 4: Define the empirical Ritz vectors $\tilde{\boldsymbol{v}}_j$ to be the columns of $V \coloneqq K_{N-1}\mathfrak{T}^{-1}$. Each column of V is the projection of the measured snapshot onto the eigenspace spanned by the eigenfunction. Therefore, if $\tilde{\mu}_j$ approximates the true eigenvalue of the Koopman operator, then $\tilde{\boldsymbol{v}}_j$ is closely related to the Koopman mode and the eigenfunction.

It is shown in [34] that if all empirical Ritz values $\tilde{\mu}_1, \tilde{\mu}_2, ..., \tilde{\mu}_{N-1}$ are nonzero and distinct, then the following decompositions of the data are obtained

$$z_k = \sum_{j=1}^{N-1} \tilde{\mu}_j^k \, \tilde{\boldsymbol{v}}_j, k = 0,1, \dots N-2, \quad z_{N-1} = \sum_{j=1}^{N-1} \tilde{\mu}_j^{N-1} \, \tilde{\boldsymbol{v}}_j + \boldsymbol{r} \tag{2-28}$$

Comparing (2-28) with (2-12), the empirical Ritz values $\tilde{\mu}_j$ and vectors $\tilde{\boldsymbol{v}}_j$ behave equivalently to the Koopman eigenvalues λ_j and the terms $\varphi_j \vec{v}_j$. However, the sum is finite in (2-28) instead of the infinite sum in (2-12). If the data in (2-22) are generated by a continuous-time system with a sampling time Δt (i.e., $x_k = F^{k\Delta t}(x_0)$), then the continuous-time eigenvalues are given by $\log(\tilde{\mu}_j)/\Delta t$.

Arnoldi-type methods require the vector-valued measurements in a high dimension, at least satisfying $p > N - 1$. To address the rank deficiency, a variant of the typical Arnoldi algorithm called the Prony-type method [35] (or Hankel DMD) is proposed using the time-delay embedding techniques. The embedding of delay coordinates helps construct a “rich" feature space for the geometrical reconstruction of non-linear dynamical systems, which is justified by the Takens embedding theorem [36]. The delay-coordinate embedding can be applied to other data-driven approximation methods as well, for example, EDMD for input-output dynamical systems [61].

2.2.2 Dynamic Mode Decomposition with Control (DMDc)

Dynamic mode decomposition (DMD) is a data-driven and equation-free approach that reconstructs the underlying dynamics of the nonlinear system from snapshot measurements alone in (2-22). The relationship between DMD and the Koopman operator theory is analyzed rigorously in [24].

Defining the lifted state $\tilde{z} = \vec{\psi}(\vec{g}(x)) = \tilde{\psi}(x) \in \mathbb{R}^q$ and neglecting the projection from the infinite dimensional function space $\wp$ to an q-dimensional linear space $\wp_q \subseteq \wp$, the approximated linear lifted dynamics becomes

$$\tilde{z}_{k+1} = A\tilde{z}_k \tag{2-29}$$

with $A = K_{\Delta t}^T$. Note that the lifting space typically has a much higher dimension than the dimension of the raw measurements ($q \gg p$). The choice of the (nonlinear) lifting (dictionary) function $\vec{\psi}$ depends on the underlying dynamics.

Example 2.2 demonstrates that with appropriate lifting functions (e.g. $\tilde{\psi}(x)=[x_1, x_2, x_1^2]$), a finite-dimensional ($q=3$), closed, and invariant subspace can be found for the Koopman operator. However, for most general cases, the finite-dimensional linear space is actually an approximation, on which the Koopman operator is not strictly invariant. An illustrative example is the logistic map, given by $x_{k+1}=\beta x_k(1-x_k)$, [26]. The idea of lifting dynamics is consistent with the EDMD algorithm, and DMD corresponds to the particular selection of the lifting function $\tilde{z}=\vec{\psi}(\vec{g}(x))=\vec{g}(x)=z$.

The extension of DMD to take the external forces (controls) into account is referred to as DMD with control (DMDc), deriving from KIC in subsection 2.1.3. Accordingly, the Koopman operator can be approximated in a finite-dimensional subspace spanned by the lifted functions $\tilde{z}=\vec{\psi}(\vec{g}(x),u)=\tilde{\psi}(x,u)\in\mathbb{R}^q$. To obtain a linear dynamical system, lifting functions $\tilde{\psi}(x,u)$ have the following form,

$$\{\tilde{\psi}_j(\vec{g}(x))\}_{j=1}^{q}\cup\{u_j\}_{j=1}^{m} \tag{2-30}$$

and the linear lifted dynamics thus become

$$\tilde{z}_{k+1}=A\tilde{z}_k+Bu_k \tag{2-31}$$

with $A\in\mathbb{R}^{q\times q}, B\in\mathbb{R}^{q\times m}$. Same as the case of DMD, DMDc corresponds to $\tilde{z}=\tilde{\psi}_j(\vec{g}(x))=\vec{g}(x)=z$.

- **Algorithms of DMDc**

The dynamical data preparation is shown conceptually in Figure 2-4, where the datasets of system observables and control inputs $\{Z, Z^+, U\}$ come from historical records, laboratory experiments, or numerical simulations. Unlike the Arnoldi-type methods, the data of

DMDc usually come from multiple trajectories, and there is no requirement of any temporal ordering in each single data matrix. The vector in the matrix Z^+ satisfies $z_k^+ = \vec{g}(f(x_k, u_k))$ with $z_k = \vec{g}(x_k), z_k, z_k^+ \in \mathbb{R}^p$. The DMDc algorithm aims to compute the matrices A, B in (2-31). If $p \gg N$ (e.g., the global climate system and fluid flows), a reduced-order dynamical system is preferred. We present the DMDc algorithm considering two cases.

- **Case A: Low-dimensional observables (p is relatively small)**

In this context, the matrices $A \in \mathbb{R}^{p\times p}, B \in \mathbb{R}^{p\times m}$ are calculated directly in a least-square sense

$$\min_{A,B} \| Z^+ - AZ - BU \|_F \tag{2-32}$$

The symbol $\| \cdot \|_F$ denotes the Frobenius norm of a matrix. The analytical solution to (2-32) is

$$[A, B] = Z^+ [Z; U]^\dagger \tag{2-33}$$

An efficient and accurate way to find the pseudoinverse is the singular value decomposition (SVD). When $p \ll N$, it is computationally beneficial to solve the normal equations,

$$\begin{aligned} &V = MG, \\ &V = Z^+ \begin{bmatrix} Z \\ U \end{bmatrix}^T, G = \begin{bmatrix} Z \\ U \end{bmatrix} \begin{bmatrix} Z \\ U \end{bmatrix}^T \end{aligned} \tag{2-34}$$

where $M = [A, B], V \in \mathbb{R}^{p\times(p+m)}, G \in \mathbb{R}^{(p+m)\times(p+m)}$. The calculation burden of (2-34) has nothing related to N (the total number of snapshots in data matrices).

➢ **Case B: High-dimensional observables (p is relatively large)**

When the system measurement vector is of high dimension, a reduced-order dynamical system is sought to reduce the computational complexity when the identified system is exploited for predictions and spectral properties analysis. The algorithm of DMDc is outlined as follows, [37].

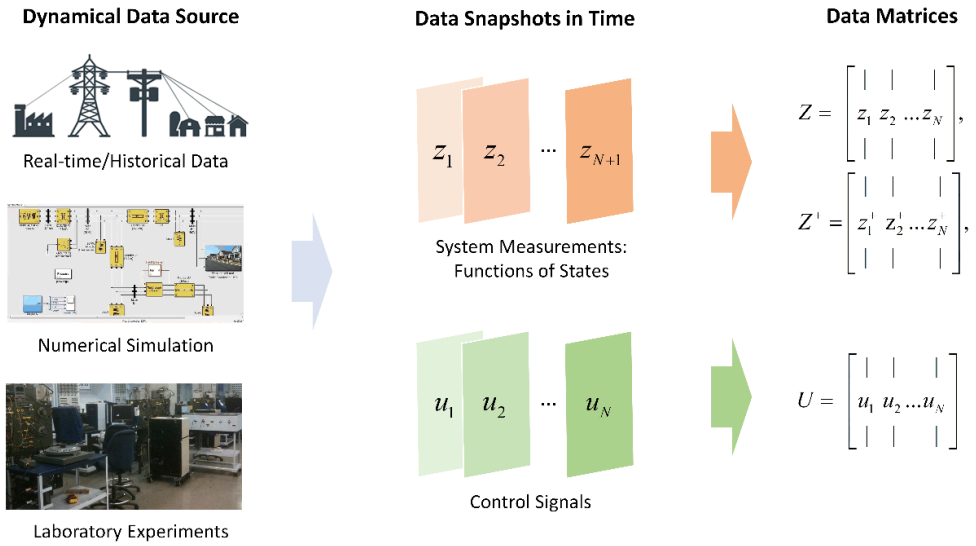

Figure 2- 4 Dynamical Data Collection and Organization in DMDc

Reduced-Order DMDc

Step 1: Collect and construct the data matrices

Given the data matrices in Figure 2-4, stack matrices Z and U to get matrix $\Omega = [Z;U]$.

Step 2: Compute SVD of the input space matrix Ω

Compute SVD on Ω and approximate the input space as $\Omega \approx \tilde{U}\tilde{\Sigma}\tilde{V}^*$ with truncation value t. The selection of t has a rich literature; notably, the Eckart-Young theorem is a rigorous and popular method [38].

Step 3: Compute SVD of the output space matrix Z^+

Compute SVD on Z^+ and approximate the output space as $Z^+ \approx \hat{U}\hat{\Sigma}\hat{V}^*$ with truncation value r.

Step 4: Compute the reduced-order dynamical system matrices.

The reduced-order dynamical system is $z_{k+1}^{red} = \tilde{A}z_k^{red} + \tilde{B}u_k$ with matrices defined as

$$\begin{aligned} \tilde{A} &= \hat{U}^* Z^+ \tilde{V}\tilde{\Sigma}^{-1}\tilde{U}_1^*\hat{U} \in \mathbb{R}^{r\times r}, \\ \tilde{B} &= \hat{U}^* Z^+ \tilde{V}\tilde{\Sigma}^{-1}\tilde{U}_2^* \in \mathbb{R}^{r\times m}, \\ z_k^{red} &= \hat{U}^* z_k \end{aligned} \tag{2-35}$$

where $\tilde{U}^* = [\tilde{U}_1^*, \tilde{U}_2^*], \tilde{U}_1^* \in \mathbb{R}^{N\times p}, \tilde{U}_2^* \in \mathbb{R}^{N\times m}$.

Step 5: Perform eigenvalue decomposition on $\tilde{A}$

The eigenvalue decomposition of the reduced-order system matrix is $\tilde{A}W = W\Lambda$. The eigenvalues of $\tilde{A}$ are also eigenvalues of the full order system matrix $A \in \mathbb{R}^{p\times p}$.

Step 6: Compute the dynamic modes (eigenvectors) of the system matrix A

The Exact DMD method [39] is utilized to calculate the eigenvectors ϕ of $A \in \mathbb{R}^{p\times p}$,

$$\phi = Z^+ \tilde{V}\tilde{\Sigma}^{-1}\tilde{U}_1^*\hat{U}W \tag{2-36}$$

If the eigenvalue $\lambda \neq 0$, then Eqn. (2-36) is utilized; else, $\phi = \hat{U}W$. Based on the reduced-order dynamical system, the system trajectory prediction is depicted in Figure 2-5.

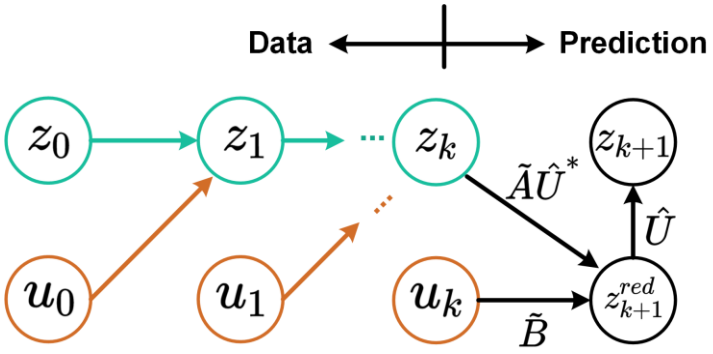

Figure 2- 5 System Trajectory Prediction via the Reduced-Order System

Chapter 3

Extended State Observer

A dynamical system evolves by actively interacting with the external environment: being regulated by manipulated control input and exporting system outputs. The accessible inputs and outputs signals may represent direct measurements or partially contain indirect information about the system's intrinsic states. A ***state observer*** or ***state estimator*** is a system that provides an estimation of the internal states asymptotically based on the real-time measurements of the system inputs and outputs. If the dynamical system is observable, it is entirely possible to reconstruct system states, and thus advanced control techniques using state feedback are allowed.

Extended state observer (ESO) was explicitly proposed by J. Han in his seminal work [40] to estimate the "total disturbance" in the context of ***active disturbance rejection control (ADRC)***. ESO treats all external disturbances, internal uncertainties, and even numerical calculation errors as a lumped disturbance and tries to estimate it as an extended state. ADRC utilizes the disturbance estimation by ESO to actively compensate the "total disturbance" and reduces the original dynamical system into a new format that is easy to control, e.g., the canonical form in ADRC cascaded-integrators system.

3.1 Review of the State Observer

The information flow of the state observer is presented in Figure 3-1, where the system states are estimated relying on the measured control inputs and the system outputs. The system dynamics (if known) or any existing pre-knowledge should be incorporated into the state observer to release the estimation burden. This section briefly introduces the general state observer with known or unknown system dynamics, analyzes and compares the estimation error of linear and nonlinear state observer designs.

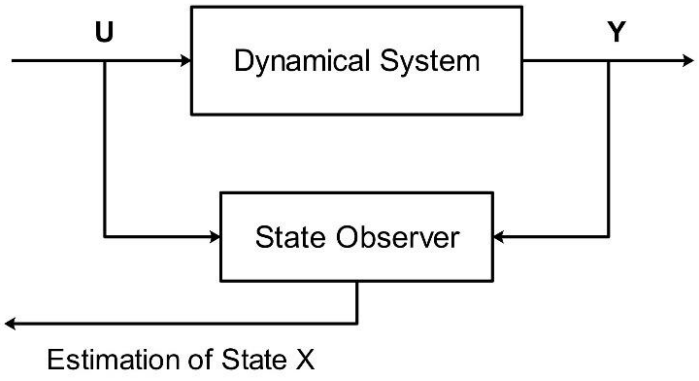

Figure 3 - 1 Information Flow of the State Observer

3.1.1 State Observer with Known System Dynamics

For a linear dynamical system with control,

$$\begin{cases} \dot{x} = Ax + Bu \\ y = Cx \end{cases} \tag{3-1}$$

where $x \in R^n$ stands for system states; $u \in R^p$ represents the control input and $y \in R^q$ is the system output; in general, $q < n, p < n$. The system matrix $A \in R^{n \times n}$, control matrix $B \in R^{n \times p}$ and output matrix $C \in R^{q \times n}$ are assumed to be known in advance.

A dynamical system is constructed with u and y from (3-1) as the system input,

$$\begin{cases} \dot{z} = Az + Bu + L(y - \hat{y}) = (A - LC)z + \begin{bmatrix} L & B \end{bmatrix} \begin{bmatrix} y \\ u \end{bmatrix} \\ \hat{y} = Cz \end{cases} \tag{3-2}$$

where vector $z \in R^n$ is the estimation of $x \in R^n$. System in (3-2) was originated by D. G.Luenberger [42] and is well-known as Luenberger observer. The observer corrects the estimation with feedback from the estimation error $\left(y - \hat{y}\right)$, and $L \in R^{n \times q}$ is the observer gain.

Define the estimation error as $e = x - z$, then we have

$$\dot{e} = (A - LC)e \tag{3-3}$$

The exponential convergence to the true state is guaranteed when $(A - LC)$ is a Hurwitz (stable) matrix, with the convergence rate dependent on the observer gain L. The eigenvalues of $(A - LC)$ can be placed arbitrarily when system (3-1) is observable. Next, we consider a nonlinear dynamical system with known dynamics $f(x_1, x_2)$ and a control gain b,

$$\begin{cases} \dot{x}_1 = x_2 \\ \dot{x}_2 = f(x_1, x_2) + bu \\ y = x_1 \end{cases} \tag{3-4}$$

The corresponding state observer is designed in (3-5),

$$\begin{cases} \dot{z}_1 = z_2 + l_1(y - \hat{y}) \\ \dot{z}_2 = f(z_1, z_2) + bu + l_2(y - \hat{y}) \\ \hat{y} = z_1 \end{cases} \tag{3-5}$$

Then the estimation error between (3-4) and (3-5) is shown in (3-6),

$$\begin{cases} e_1 = x_1 - z_1, e_2 = x_2 - z_2 \\ \dot{e}_1 = e_2 - l_1 e_1 \\ \dot{e}_2 = f(x_1, x_2) - f(x_1 - e_1, x_2 - e_2) - l_2 e_1 \end{cases} \tag{3-6}$$

If the known internal dynamics $f(x_1, x_2)$ is continuous and differentiable, using Taylor expansion, Eqn. (3-6) can be approximated to (3-7).

$$\begin{cases} e_1 = x_1 - z_1, e_2 = x_2 - z_2 \\ \dot{e}_1 = e_2 - l_1 e_1 \\ \dot{e}_2 \approx \dfrac{\partial f}{\partial x_1} e_1 + \dfrac{\partial f}{\partial x_2} e_2 - l_2 e_1 \end{cases} \tag{3-7}$$

When the partial derivatives $\partial f / \partial x_1$ and $\partial f / \partial x_2$ are bounded, there always exists a feedback gain $L = [l_1, l_2]$ to make the system (3-7) stable.

3.1.2 State Observer with Unknown System Dynamics

The linear/nonlinear dynamical systems mentioned in the last section assume complete modeling. However, the internal dynamics $f(x_1, x_2)$ in (3-4) generally involve the effects of uncertain noises and unpredicted intermittent disturbances, e.g., the intense penetration of renewable energy sources (RESs) in power systems. Therefore, the exact expression of $f(x_1, x_2)$ is typically inaccessible in most practical applications. To this end, nonlinear feedback is applied to improve the estimation accuracy and computation efficiency confronting unknown dynamics f. A nonlinear state observer is designed as,

$$\begin{cases} \dot{z}_1 = z_2 - \beta_{01} g_1(e) \\ \dot{z}_2 = bu - \beta_{02} g_2(e) \\ e = z_1 - y \end{cases} \tag{3-8}$$

where $\beta_{01} g_1(e)$ and $\beta_{02} g_2(e)$ are nonlinear feedback functions satisfying

$eg_i(e) \geq 0, i = 1,2$ and $\beta_{01}, \beta_{02} \geq 0$. When the nonlinear feedback functions are well-selected, the state observer in (3-8) can estimate the states in (3-4) accurately regardless of various dynamics in f .

Example 3.1: To illustrate the validness of (3-8), an autonomous dynamical system ($b = 0$) is considered with unknown nonlinear dynamics,

$$\begin{aligned} f(x_1, x_2, t) &= -(1 + \frac{\cos(t)}{2})x_1 - (1 + \sin(\frac{t}{3}))x_2 + w(t), \\ w(t) &= sign(\sin(\frac{3t}{2})) \end{aligned} \tag{3-9}$$

The initial states are set as $x_1(0) = x_2(0) = 0$, and the state observer is designed as

$$\begin{cases} e = z_1 - y \\ \dot{z}_1 = z_2 - 100e \\ \dot{z}_2 = -200\, fal(e, r, \delta) + bu \end{cases}$$
$$fal(e, r, \delta) = \begin{cases} |e|^r \ sign(e), & |e| > \delta \\ \dfrac{e}{\delta^{1-r}}, & |e| \leq \delta \end{cases} \tag{3-10}$$

where $fal(e, r, \delta)$ is a commonly used nonlinear feedback function for anti-chattering in the discrete-time design. We set the Euler integration time step $\Delta t = 0.01s$ and $\delta = \Delta t, r = 0.5$ in (3-10). The estimation performance of the state observer is presented in Figure 3-2. The state observer is randomly initialized and can accurately track the true system states with almost negligible estimation error. Therefore, the state observer is largely independent of the system dynamics and, in this sense, Eqn. (3-10) fits in a wide range of different f .

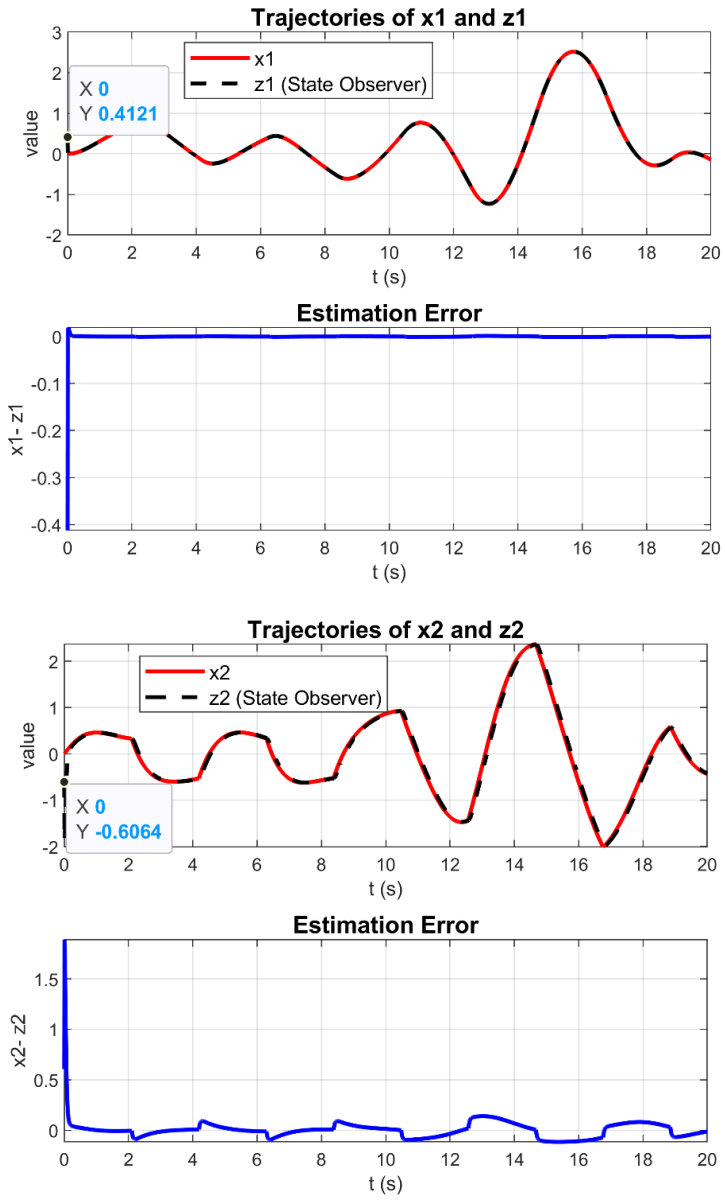

Figure 3 - 2 ***Example 3.1*:** State Observer States Estimation

3.1.3 Analysis of the State Observer Estimation Error

To simplify the analysis of the estimation error in the nonlinear state observer, the unknown dynamics is assumed as a constant $f \equiv w_0 = const$, then the estimation error considering (3-8) and (3-4) is

$$\begin{cases} e_1 = z_1 - x_1, e_2 = z_2 - x_2 \\ \dot{e}_1 = e_2 - \beta_{01} e_1 \\ \dot{e}_2 = -w_0 - \beta_{02}\, fal(e_1, r, \delta) \end{cases} \tag{3-11}$$

When system (3-11) is in a steady state with $\delta = 0, r = 0.5$, the estimation error boundaries are given as follows

$$| e_1 | = (\frac{w_0}{\beta_{02}})^2, | e_2 | = \beta_{01}(\frac{w_0}{\beta_{02}})^2 \tag{3-12}$$

If the feedback gain β_{02} satisfies $\beta_{02} \gg w_0$, then the estimation error is limited at a relatively low level. Compared with linear error feedback ($g_i(e) = e$) where the estimation error is proportional to $|\frac{w_0}{\beta_{02}}|$, the state observer with nonlinear feedback has a greatly improved accuracy since $(\frac{w_0}{\beta_{02}})^2 \ll |\frac{w_0}{\beta_{02}}|$ with $\beta_{02} \gg w_0$. As to more general cases of bounded $f(x_1, x_2)$, ref. [41] elaborates a similar conclusion based on the Lyapunov theory; proof details are omitted here.

3.2 Basics of Extended State Observer

Last section demonstrates that the nonlinear state observer (3-8) can estimates the dynamical system (3-4) accurately with unknown dynamics $f(x_1, x_2)$. Extended state observer (ESO) treats $f(x_1, x_2)$ as an extended state $x_3 = f(x_1, x_2)$ and $\dot{x}_3 = \xi(t)$, and tries to estimate it. This idea can be traced back to a high-gain observer with an augmented state variable used in [43]. With the introduction of the extended state, dynamical system (3-4) can be rewritten as

$$\begin{cases} \dot{x}_1 = x_2 \\ \dot{x}_2 = x_3 + bu \\ \dot{x}_3 = \xi(t) \\ y = x_1 \end{cases} \tag{3-13}$$

Accordingly, ESO is designed as below (input gain b is assumed to be known)

$$\begin{cases} \dot{z}_1 = z_2 - \beta_{01} g_1(e) \\ \dot{z}_2 = bu + z_3 - \beta_{02} g_2(e) \\ \dot{z}_3 = -\beta_{03} g_3(e) \\ e = z_1 - y \end{cases} \tag{3-14}$$

Numerical studies and industry applications since ESO was proposed have verified that with well-tuned functions $g_i(e), i = 1,2,3$ and parameter $\beta_{01}, \beta_{02}, \beta_{03}$, ESO in (3-14) has satisfying adaptability, robustness, and estimation accuracies. Estimations of the system intrinsic states $[x_1(t), x_2(t)]$ and the extended state $x_3(t) = f(x_1(t), x_2(t))$ are thus provided in a unified framework. The unknown dynamics $f(x_1(t), x_2(t))$ may have other different formats, e.g., $f(t)$ or $f(x_1, x_2, \omega(t))$. However, no matter f is continuous or discontinuous, time-invariant or time-varying, linear or nonlinear, ESO given by (3-14) can always work, and its design is thus independent of the detailed expression of f .

On the other side, it should be noted that ESO is never "model-free". Any pre-knowledge or existing modeled dynamics should be made full use in (3-14), which will help release the estimation burden of ESO and increase the accuracy level. Besides, the control gain b does not need to be precisely known; experiments show that an approximation of b with even 50% relative error will not degrade the performance of ESO significantly. The estimated value of b is supposed as b_0 and the dynamics f is split into two parts

$$f = f_0(x_1, x_2) + f_1(x_1, x_2, t, \omega(t)) \tag{3-15}$$

with $f_0(x_1, x_2)$ is known mathematical equation, representing the basic dynamics related to principal physical laws or other pre-existing knowledge about the system; $f_1(x_1, x_2, t, \omega(t))$ stands for all unmodeled dynamics, and $\omega(t)$ is the external noise or disturbance. Then ESO in (3-14) can be modified to incorporate $f_0(x_1, x_2)$,

$$\begin{cases} \dot{z}_1 = z_2 - \beta_{01} g_1(e) \\ \dot{z}_2 = b_0 u + f_0(z_1, z_2) + z_3 - \beta_{02} g_2(e) \\ \dot{z}_3 = -\beta_{03} g_3(e) \\ e = z_1 - y \end{cases} \tag{3-16}$$

where $z_3 \to x_3(t) = f_1(x_1, x_2, t, \omega(t)) + (b - b_0)u(t)$ involves both the unmodeled dynamics and the effect of control gain estimation error. Nonlinear functions $fal(e, r, \delta), r = \frac{1}{2^{i-1}}$ are often used when choosing $g_i(e), i > 1$ and $g_1(e) = e$. Although nonlinear function has higher efficiency, linear ESO ($g_i(e) = e$) avoids the time-consuming parameter tuning and makes an explicit connection with the concept of bandwidth, which will be covered in the next section.

- ***Example 3.2:*** Take a second-order strongly nonlinear dynamical system in (3-17) as an example to illustrate the estimation performance of nonlinear ESO (NESO).

$$\begin{cases} \dot{x}_1 = x_2 \\ \dot{x}_2 = sign(\sin(0.05t)) + b(t)u(t) \\ b(t) = 1.5 + 0.5 sign(\sin(0.03t)), u(t) = \cos(0.02t) \\ y = x_1 \end{cases} \tag{3-17}$$

In this case, the control gain b is time-varying and approximated as a constant $b_0 = 1.5$ in the designed ESO,

$$\begin{cases} e = z_1 - y,\ fe = fal(e, 0.5, \delta),\ fe_1 = fal(e, 0.25, \delta) \\ \dot{z}_1 = z_2 - \beta_{01} e \\ \dot{z}_2 = b_0 u(t) + z_3 - \beta_{02} fe \\ \dot{z}_3 = -\beta_{03} fe_1 \end{cases} \tag{3-18}$$

where the extended state is $x_3(t) = 0.5sign(\sin(0.03t))\cos(0.02t) + sign(\sin(0.05t))$. The numerical simulation results of (3-18) are displayed in Figure 3-3, where the system states, as well as the extended state are estimated accurately. Therefore, ESO inherits the power of the conventional state observer and embodies the benefit of identifying system unknown dynamics in real-time based on the system input and output measurements. The convergence of various high gain NESOs can be found in [44], where a group of nonlinear systems with uncertainties are considered.

To be sure, disturbance estimation and cancellation have been studied over the past years, and many solutions are proposed, such as the unknown input observer (UIO) [45, 46] and the disturbance observer (DOB) [47, 48]. These observers both rely on an exact mathematical system model and behave sensitively to the observer gains. In this regard, ESO is quite different, escaping from the sufferings of burdensome modeling procedures and combining the estimation power of a UIO with the tuning simplicity of a DOB [49].

The ability of ESO to extract “total disturbance” from the system input and output measurements lies in the fact that the “total disturbance” has influences on the system output. The system measurements are believed to contain information about the “total disturbance” (acceleration) in turn. For disturbances not affecting the system output, there is no need to take them into consideration when designing controllers. In the framework of ADRC, the lumped disturbance, estimated by ESO, is then compensated in the input channel, which reduces the system dynamics to a disturbance-free form.

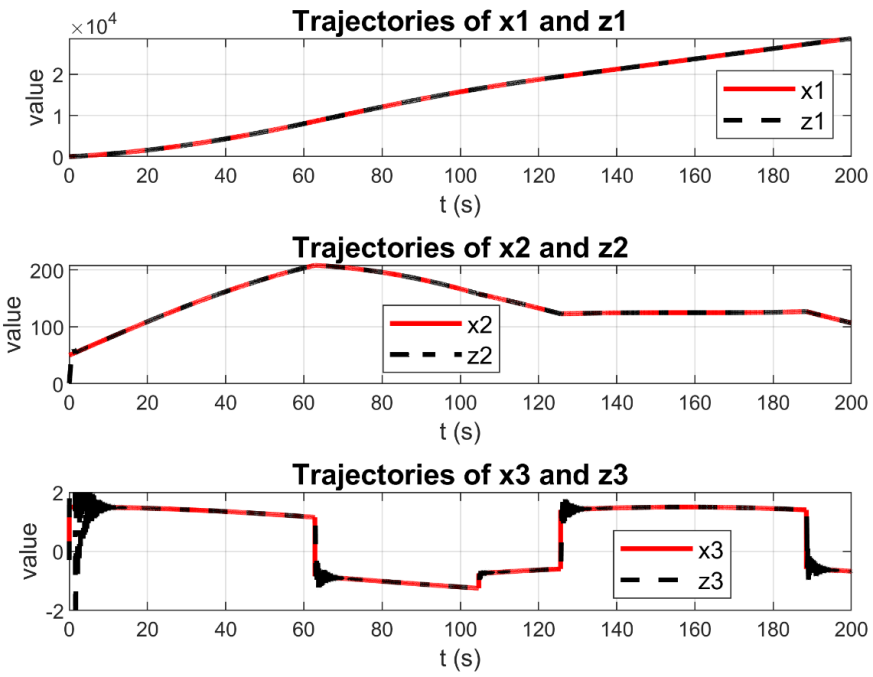

Figure 3 - 3 ***Example 3.2:*** Estimation performance of NESO

$(\Delta t = 0.01s, \beta_{01} = 10, \beta_{02} = 41, \beta_{03} = 66)$

3.3 Linear Extended State Observer (LESO)

Unfortunately, although huge applications of NESO have been carried out in engineering applications [50~52], the choice of the nonlinear feedback functions $g_i(e)$ is essentially experiential. To apply ESO conveniently in practice, Gao proposed the linear extended state observer (LESO) in [53] to avoid the cumbersome parameter tuning and built an explicit connection with the concept of bandwidth. This section gives an overview of LESO and its primary design guidelines.

Revisiting the second-order dynamical system with the "total disturbance" $f(x_1, x_2)$ in (3-4) and its equivalent format in (3-13), we reorganize the system representation to a state-space model

$$\begin{aligned} \dot{x} &= Ax + Bu + E\xi \\ y &= Cx \end{aligned} \tag{3-19}$$

where

$$A = \begin{bmatrix} 0 & 1 & 0 \\ 0 & 0 & 1 \\ 0 & 0 & 0 \end{bmatrix}, B = \begin{bmatrix} 0 \\ b \\ 0 \end{bmatrix}, E = \begin{bmatrix} 0 \\ 0 \\ 1 \end{bmatrix}, C = [1 \;\; 0 \;\; 0] \tag{3-20}$$

The extended state vector $x = [x_1, x_2, x_3]^T$ has the extended state x_3 involved, which stands for the lumped disturbance. The linear ESO in (3-20) is constructed with the feedback functions $g_i(e) = e, i = 1, 2, 3$ so that a LESO is formulated as

$$\begin{aligned} \dot{z} &= Az + Bu + L(y - \hat{y}) \\ \hat{y} &= Cz \end{aligned} \tag{3-21}$$

The correction terms, $l_i(y - \hat{y})$, are used to accommodate the unknown initial states, the uncertainties in parameters, and the disturbances. Vector L can be obtained using the pole placement technique,

$$L = \left[\beta_{01}, \beta_{02}, \beta_{03}\right]^T \tag{3-22}$$

Several key points of the LESO in (3-21) are listed below,

- **Stability:**

Define $e = x - z$, then subtracting (3-21) from (3-19) yields,

$$\dot{e} = A_e e + E\xi \tag{3-23}$$

with $A_e = A - LC = \begin{bmatrix} -\beta_{01} & 1 & 0 \\ -\beta_{02} & 0 & 1 \\ -\beta_{03} & 0 & 0 \end{bmatrix}$. LESO is bounded-input bounded-output (BIBO) stable if the roots of the characteristic polynomial of A_e

$$\left|sI - A_e\right| = s^3 + \beta_{01}s^2 + \beta_{02}s + \beta_{03} \tag{3-24}$$

are all on the left half plane (LPH) and ξ is bounded, as claimed in Lemma 3.1 and

followed by proof [54].

Lemma 3.1 *If A_e is a Hurwitz (stable) matrix with a suitable observer gain L and the lumped disturbance $f(x_1, x_2)$* or *$f(x_1, x_2, t, \omega(t))$ is differentiable on t with $\xi = \partial f / \partial t$, then the estimation error e is bounded for any bounded $d = E\xi$. Moreover, the boundary of e satisfies $\| e \|_2 = 2 \| P^T d \|_2$, where P is the unique solution of the Lyapunov equation $A_e^T P + P A_e = -I$ with I being an identity matrix.*

Proof: When A_e is a Hurwitz (stable) matrix, suppose $V = e^T P e$ as a Lyapunov function, where P is the unique solution to the Lyapunov equation $A_e^T P + P^T A_e = -Q$ and Q is a positive definite matrix. Then,

$$\dot{V} = 2d^T Pe - e^T Qe = -(e^T Q^{\frac{1}{2}} - d^T PQ^{-\frac{1}{2}})(e^T Q^{\frac{1}{2}} - d^T PQ^{-\frac{1}{2}})^T + (d^T PQ^{-\frac{1}{2}})(d^T PQ^{-\frac{1}{2}})^T \quad (3\text{-}25)$$

Therefore, when

$$\| e^T Q^{\frac{1}{2}} - d^T PQ^{-\frac{1}{2}} \|_2 > \| d^T PQ^{-\frac{1}{2}} \|_2 \text{ or } \| e^T Q^{\frac{1}{2}} \|_2 > 2 \| d^T PQ^{-\frac{1}{2}} \|_2 \quad (3\text{-}26)$$

we have $\dot{V} < 0$. For $Q = I$,

$$\| e \|_2 > 2 \| P^T d \|_2 \rightarrow \dot{V} < 0 \quad (3\text{-}27)$$

so V decreases as long as (3-27) is satisfied. After entering steady state, $\| e \|_2$ is bounded by $2 \| P^T d \|_2$. Q.E.D.

Assign the poles of (3-24) at $-\omega_0$, then $|sI - A_e| = (s + \omega_0)^3$, and accordingly,

$$\beta_{01} = 3\omega_0, \beta_{02} = 3\omega_0^2, \beta_{03} = \omega_0^3 \quad (3\text{-}28)$$

where ω_0 denotes the bandwidth of the linear extended state observer (LESO).

- **Tuning (Optimization) of the bandwidth ω_0**

With the LESO parameterization linked with the concept of bandwidth, the tuning of LESO becomes straightforward with clear physical meaning. In general, the faster the LESO tracking speed is, the sooner the disturbance is observed and compensated by the controller. That is, the observer bandwidth ω_0 should be increased as much as allowed by the hardware and software limitations.

- **Limitations of LESO**

  (1) Sensor noises: The observer bandwidth is limited by the ubiquitous sensor noises in practical applications. The observer bandwidth ω_0 is selected to make sure there is no significant oscillation in the estimations.

  (2) Sampling rate: The observer bandwidth ω_0 is also limited by the sampling rate since the operation of LESO is subject to the sampling delay.

LESO functions in the inner loop of the overall control architecture to cancel out the uncertainties and reduces the dynamical system under control to be disturbance-free. To this end, LESO generally works faster than the outer-loop controller. Therefore, the bandwidth of LESO is often higher than the controller, and a suggested thumb ratio is

$$\omega_0 = 3 \sim 5\omega_c \tag{3-29}$$

where ω_c is the control loop bandwidth, determined by the transient response requirements, especially the specifications on the settling time.

- ***Example 3.3:*** Consider a motion control testbed in [53] with a mathematical model verified in the hardware test as

$$\ddot{y} = -1.41\dot{y} + 23.2T_d + 23.2u \tag{3-30}$$

where y denotes the output position, u is the control voltage sent to the power amplifier to drive the motor, and T_d is the torque disturbance. The control gain used in LESO is $b = 40$ instead of the exact value $b_0 = 23.2$. So the lumped disturbance is $f = -1.41\dot{y} + 23.2T_d - 16.8u \rightarrow \ddot{y} = f + bu$.

The torque disturbance T_d considered in this case is random in [-0.02, 0.02] and the system input is

$$u(t) = \gamma sign(\sin(2 * t / \pi)) \tag{3-31}$$

with $\gamma = 0.15$. Supposing the sample rate $\Delta t = 1ms$ and integrating by Euler method, the estimation performance of LESO with bandwidth $\omega_0 = 40\text{rad/sec}$ is exhibited in Figure 3-4. The position x_1, motion speed x_2 and the lumped disturbance f are tracked accurately.

3.4 Discrete Implementation of the Extended State Observer

A continuous-time dynamical model (3-19) is usually discretized by Euler approximation or zero order hold (ZOH). The discrete-time model corresponding to (3-19) is

$$\begin{aligned} x(k+1) &= A_d x(k) + B_d u(k) + E_d \xi(k) \\ y(k) &= C_d x(k) \end{aligned} \tag{3-32}$$

where k denotes a discrete time instant kT_s, and T_s is the sampling rate. A_d, B_d, C_d, E_d are discrete-time system matrices. Then the discrete-ESO (DESO) for (3-32) is

$$\begin{aligned} \hat{x}(k+1) &= A_d \hat{x}(k) + B_d u(k) + L_d (y(k) - \hat{y}(k)) \\ \hat{y}(k) &= C_d \hat{x}(k) \end{aligned} \tag{3-33}$$

Estimator (3-33) is a ***predictive estimator*** since the current estimation error $y(k) - \hat{y}(k)$ is used to update the subsequent state estimation $\hat{x}(k+1)$. The feedback vector L_d is

adjusted by placing the eigenvalues of the error dynamical matrix $(A_d - L_d C_d)$ at a single location $\beta = e^{-\omega_0 T_s}$, where ω_0 is the bandwidth of the continuous-ESO (CESO),

$$\det(zI - (A_d - L_d C_d)) = (z - \beta)^3 \tag{3-34}$$

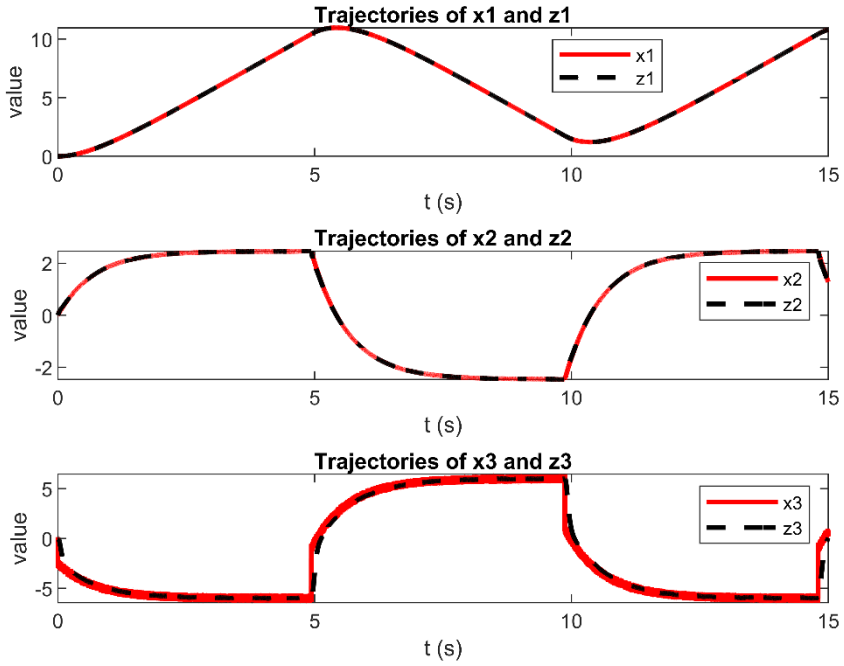

Figure 3 - 4 ***Example 3.3*** Estimation Performance of LESO

Applying the Euler approximation, system matrices in (3-32) are presented below,

$$A_d = \begin{bmatrix} 1 & T_s & 0 \\ 0 & 1 & T_s \\ 0 & 0 & 1 \end{bmatrix}, B_d = \begin{bmatrix} 0 \\ bT_s \\ 0 \end{bmatrix}, E_d = \begin{bmatrix} 0 \\ 0 \\ T_s \end{bmatrix}, C_d = [1,0,0] \tag{3-35}$$

then the feedback gain vector $L_d = [l_1, l_2, l_3]^T$ has the following values

$$l_1 = 3 - 3\beta, l_2 = \frac{3(\beta - 1)^2}{T_s}, l_3 = \frac{(1-\beta)^3}{T_s^2} \tag{3-36}$$

In addition, ZOH provides a more accurate approximation of the continuous-time system discretization with matrices given as,

$$
\begin{aligned}
A_d &= e^{AT_s} = \sum_{k=0}^{\infty} \frac{A^k T_s^k}{k!} = \begin{bmatrix} 1 & \mathrm{T}_s & \mathrm{T}_s^2/2 \\ 0 & 1 & \mathrm{T}_s \\ 0 & 0 & 1 \end{bmatrix}, \\
B_d &= \int_0^T e^{A\tau} d\tau B = \sum_{k=0}^{\infty} \frac{A^k T_s^{k+1}}{(k+1)!} B = \begin{bmatrix} T_s^2 b/2 \\ T_s b \\ 0 \end{bmatrix}, \\
C_d &= [1,0,0]
\end{aligned}
\tag{3-37}
$$

and the feedback gain vector $L_d = [l_1, l_2, l_3]^T$ becomes

$$
l_1 = 3-3\beta, l_2 = \frac{(\beta-1)^2(\beta+5)}{2T_s}, l_3 = \frac{-(\beta-1)^3}{T_s^2} \tag{3-38}
$$

3.4.1 Current Discrete ESO

The realization of DESO in a new form: ***current discrete estimator***, is proposed in [49], and it helps to maintain stable operation at a low sampling rate. The discrete predictive estimator in (3-33) has at least one sample delay since the current estimation error comes to effect until the next time instant. Instead, the current discrete estimator avoids this delay by using the present estimation error to update the current estimated states. In this way, the strict requirement of sampling rate is relaxed.

By defining the feedback vector L_d in (3-33) as $L_d = A_d L_c$ with the subscript "c" representing "current", the update equation in (3-33) is reduced to

$$
\begin{aligned}
\hat{x}(k+1) &= A_d \bar{x}(k) + B_d u(k) \\
\bar{x}(k) &= \hat{x}(k) + L_c (y(k) - \hat{y}(k))
\end{aligned}
\tag{3-39}
$$

where $\bar{x}(k)$ includes a correction of the current time update. When the sampling rate is low, the correction item significantly reduces the time delay and enhances the stability of a closed-loop system [49]. The current discrete estimator can be rewritten as

$$
\begin{aligned}
&\hat{x}(k+1) = (A_d - L_d C_d)\hat{x}(k) + [B_d, L_d][u(k), y(k)]^T, \\
&output: \bar{x}(k) = (I - L_c C_d)\hat{x}(k) + L_c y(k)
\end{aligned}
\tag{3-40}
$$

The only difference from the predictive estimator is the output, as shown in Figure 3-5.

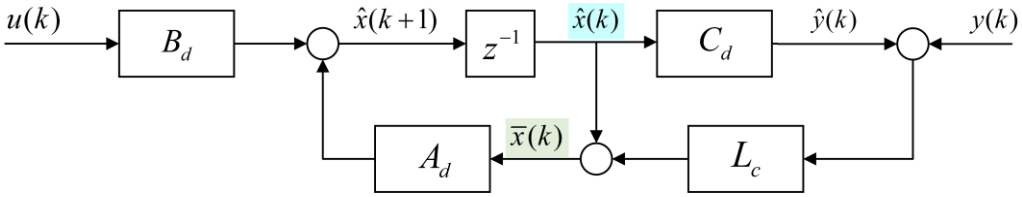

Figure 3 - 5 Block Diagram of Discrete ESO (DESO)

3.4.2 Multi-Channel ESO

Owing to the standard system format of pure chaining integrators in ADRC, the system matrix A (continuous-time) or A_d (discrete-time) is upper-triangular. The determination of the feedback gain vector L or L_d is thus made easy when placing all eigenvalues of $(A-LC)$ or $(A_d-L_dC_d)$ at a single location $-\omega_0$ or $e^{-\omega_0 T_s}$. However, for a general case of the discrete-time system matrix A_d, the calculation of L_d is not that straightforward.

The "states" of a discrete dynamical model identified by DMDc refers to accessible measurements. In this regard, the model is fully observable. To leverage this property, we come up with a design referred to as ***multi-channel ESO*** to estimate the model-plant mismatch. A linear dynamical system identified by DMDc with compensation has the format of (3-41),

$$x(k+1) = Ax(k) + Bu(k) + d(k) \tag{3-41}$$

where $x(k) \in R^n$ denotes the system measurements (functions of states) at the sampling instance of kT_s; $d(k) \in R^n$ is a vector representing the modeling error, which can be time-invariant or time-varying and needs to be estimated on line; and $u(k) \in R^m$ is the system input. The matrices $A \in R^{n\times n}$ and $B \in R^{n\times m}$ are computed by DMDc.

The system in (3-41) is naturally decomposed into n parallel channels (subsystems), and the $q^{th}, q = 1, 2, ..., n$ channel (state) has dynamics as follows.

$$x_q(k+1) = A_{qq}x_q(k) + \sum_{j=1, j\neq q}^{n} A_{qj}x_j(k) + \sum_{j\in S_c} B_{qj}u_j(k) + \sum_{j\notin S_c} B_{qj}u_j(k) + d_q(k) \tag{3-42}$$

where $x_q(k)$ is the q^{th} element of x at time kT_s, and S_c represents the set of the indexes of adjustable control inputs. Other control vector elements $u_j, j \notin S_c$ are usually given references supervised by upper layers in a hierarchical control architecture. Without loss of generality, we assume only the last element u_m is tunable, and the lumped disturbance is defined as

$$f_{kq} = \sum_{j=1, j\neq q}^{n} A_{qj}x_j(k) + \sum_{j=1}^{m-1} B_{qj}u_j(k) \tag{3-43}$$

The variable f_{kq} has known dynamics, involving couplings with other channels $x_j, j \neq q$, and the influences of un-adjustable control inputs. Since $x(k)$ and $u(k)$ are accessible, f_{kq} in (3-43) can be calculated accordingly based on the real-time measurements. Substituting (3-43) into (3-42), the q^{th} channel dynamics becomes

$$x_q(k+1) = A_{qq}x_q(k) + B_{qm}u_m(k) + f_{kq} + d_q(k) \tag{3-44}$$

We set the extended state vector as $\tilde{x}_q = [x_q, d_q]$ containing the model-plant discrepancy d_q, and (3-44) can be rewritten in a state-space form.

$$\begin{aligned} \tilde{x}_q(k+1) &= \tilde{A}\tilde{x}_q(k) + \tilde{B}u_m(k) + \tilde{F}f_{kq} + \tilde{D}\Delta d_q(k), \\ y_q(k) &= \tilde{C}x_q(k) \end{aligned} \tag{3-45}$$

where

$$\tilde{A}=\begin{bmatrix} A_{qq} & 1 \\ 0 & 1 \end{bmatrix}, \tilde{B}=\begin{bmatrix} B_{qm} \\ 0 \end{bmatrix}, \tilde{F}=\begin{bmatrix} 1 \\ 0 \end{bmatrix}, \tilde{D}=\begin{bmatrix} 0 \\ 1 \end{bmatrix}, \tilde{C}=[1\ 0]$$
$$d_q(k+1)=d_q(k)+\Delta d_q(k) \tag{3-46}$$

The corresponding LESO is designed as

$$\begin{aligned} z_q(k+1) &= \tilde{A}z_q(k)+\tilde{B}u_m(k)+\tilde{F}f_{kq}+L(y_q(k)-\hat{y}_q(k)) \\ \hat{y}_q(k) &= \tilde{C}z_q(k) \end{aligned} \tag{3-47}$$

Eqn. (3-47) is a second-order LESO with z_q as the estimation of $\tilde{x}_q$. When the dynamical error matrix $\tilde{A}_e=\tilde{A}-L\tilde{C}$ is stable, the estimation error of LESO (3-47) is bounded when the total disturbance variation Δd_q is bounded, which is often the case in real applications. Suppose all eigenvalues of $\tilde{A}_e$ are located at $\Omega_0 (0 \le \Omega_0 < 1)$ with

$$\det(\lambda I-(\tilde{A}-L\tilde{C}))=(\lambda-\Omega_0)^2 \tag{3-48}$$

then $L=[l_1,l_2]^T$ with $l_1=A_{qq}+1-2\Omega_0, l_2=(\Omega_0-1)^2$.

In this way, the disturbance (model-plant mismatch) vector $d \in R^n$ is estimated by n second-order LESOs for each channel (subsystem) in parallel, referred to as ***multi-channel LESO***. The effects of couplings from other channels and the control signals are aggregated together and calculated using the system measurements approximately. Such a design fully leverages the real-time information and the system's dynamics identified via DMDc, which helps to reduce the computation burden and relax the requirement of high bandwidth in LESOs. The tuning of each second-order LESO is only relevant to the parameter Ω_0, and clear physical meanings behind are used as basic guidelines.

Chapter 4

Extended State Observer-Koopman-Model Predictive Control

This chapter presents a data-driven control framework named Extended State Observer-Koopman-Model Predictive Control (***ESO-Koopman-MPC, EKM***) for the controller design in (nonlinear) complicated dynamical systems. Indicated by the name, the proposed control framework consists of three critical steps as follows:

- **Step 1:** Identify a dynamical model from experimental, historical, or simulation data based on the Koopman operator theory, e.g., DMDc; see Chapter 2.
- **Step 2:** The utilization of an appropriate observer to estimate the mismatch between the identified model and the real plant. The multi-channel ESO proposed in Section 3.4.2 is applied to estimate the modeling error and increase the accuracy of the data-driven modeling. The observer is highly independent of the mathematical model but only relies on the system input and output measurements.
- **Step 3:** Controller design based on model predictive control (MPC). The compensated model after Step 1&2 has an enhanced prediction ability and is embedded into the MPC structure. The overall control framework is purely data-driven and does not require any procedures of modeling.

4.1 Model Predictive Control

While the idea of MPC can be traced back to the 1960s [55], interest in this field started to surge until the 1980s. Since then, MPC has been applied in process industries spanning from chemical plants, oil refineries, power systems to aerospace engineering. Ref [56] summaries more than 4500 applications of MPC so far.

4.1.1 Basic Theory of MPC

MPC generally refers to a class of algorithms that compute a sequence of manipulated variables to optimize the future behavior of a plant while satisfying a set of constraints. The prediction of the underlying dynamical system relies on the predictive model, often obtained by system identification or direct mathematical modeling. The principle of MPC is graphically described in Figure 4-1.

At the current time t_k, the MPC solves an optimization problem over a finite prediction horizon $[t_k, t_k + N_p T_s]$ with respect to an objective function such that the predicted system output can optimally track the given reference, and the states and control input constraints are complied. The solution to the optimization problem at each step is a sequence of control inputs over a finite horizon $[t_k, t_k + N_c T_s]$ ($N_c \le N_p$). For an ideal case where there is no uncertain disturbance and the dynamical model used for prediction is absolutely accurate, the control sequence obtained at t_k can be applied for all times $t \ge t_k$ when the control horizon is infinite $N_c = \infty$.

However, due to the external disturbances, the model-plant discrepancy, and the finite prediction horizon N_p, the true system trajectory may deviate from the prediction. To

incorporate the system feedback, only the first element in the optimal sequence is applied, and until the next time step $t_k + T_s$, the entire calculation is repeated. The prediction horizon is kept being shifted forward, and for this reason, MPC is a receding or moving horizon control mechanism.

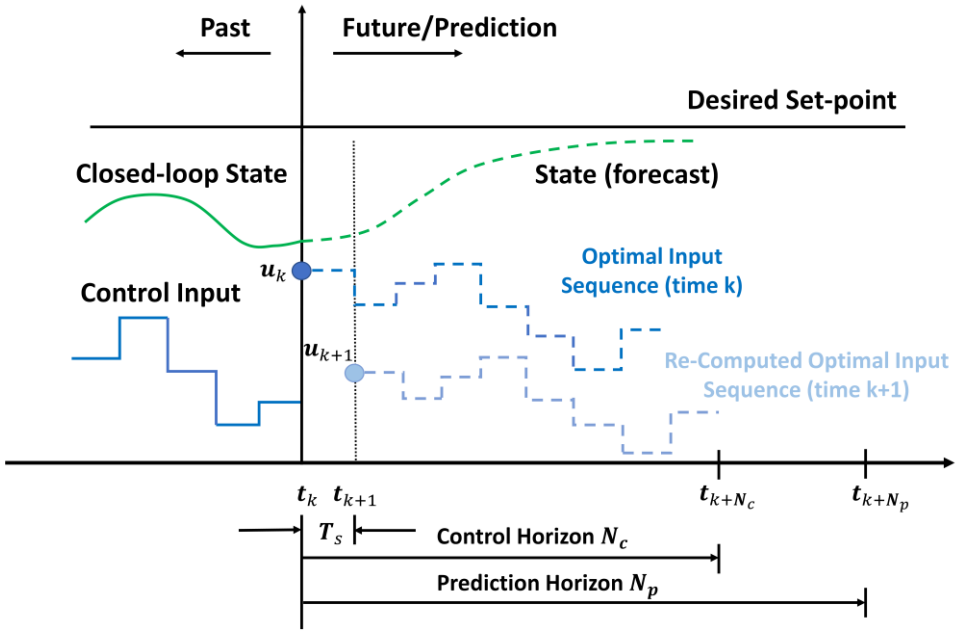

Figure 4 - 1 Discrete MPC Scheme

In general, MPC is classified by the predictive model into linear MPC (LMPC) and nonlinear MPC (NMPC). LMPC refers to a family of MPC where linear models are used to predict the system dynamics, and linear constraints on the states and inputs [57] are considered. Conversely, NMPC uses nonlinear models for predictions and/or considers a non-quadratic cost function with nonlinear constraints. The nonlinear model may have the form of an empirical data fit (e.g., artificial neural networks) or a high-fidelity dynamic model based on fundamental mass and energy balances.

4.1.2 Mathematical Formulation of MPC

- **Nonlinear MPC**

The optimization problem to be solved at time t_k is usually formulated as,

$$\min_{u} \int_{t_k}^{t_k+N_pT_s} F(\hat{x}(\tau), u(\tau))d\tau \tag{4-1}$$

subject to

$$\dot{\hat{x}}(\tau) = f(\hat{x}(\tau), u(\tau)), \quad \hat{x}(t_k) = x(t_k) \tag{4-2a}$$

$$u_{\min} \le u(\tau) \le u_{\max}, \quad \forall \tau \in [t_k, t_k + N_cT_s] \tag{4-2b}$$

$$u(\tau) = u(t_k + N_cT_s), \quad \forall \tau \in [t_k + N_cT_s, t_k + N_pT_s] \tag{4-2c}$$

$$x_{\min}(\tau) \le \hat{x}(\tau) \le x_{\max}(\tau), \quad \forall \tau \in [t_k, t_k + N_pT_s] \tag{4-2d}$$

where $\hat{x}$ denotes the predicted states and $x(t_k)$ is the true measurements at t_k; u stands for a sequence of control inputs, which are optimization variables of (4-1).

Eqn. (4-1) represents the objective function; Eqn. (4-2a) is a dynamical system model whose states are initialized by the measurements of the current states; Eqn. (4-2b~4-2c) are the magnitude limitations on the control variable u. When $N_c \le N_p$, the control inputs outside the control horizon are assumed to be unchanged after $t_k + N_cT$; Eqn. (4-2d) indicates the states constraints within the prediction horizon. The optimization problem is parameterized by the current states $x(t_k)$.

When the dynamical model (4-2a) is nonlinear, the corresponding NMPC optimization problem is not necessarily convex, which poses challenges on both the solution stability and convergence time. The numerical solvers are typically based on direct optimal control methods using Newton-type optimization schemes [58], which exploits the fact that

consecutive optimal control problems are similar. This property allows initializing the Newton-type methods efficiently by a shifted guess from the last optimal solution. Thus, considerable amounts of computation time are saved. Another case to utilize the similarity of subsequent problems is never attempting to iterate until the convergence of the optimization problem. Instead, only a few iterations are conducted towards the solution of the current NMPC problem before proceeding to the next one [59].

However, the stability and optimality of NMPC are still open questions. The applications of NMPC are limited to the processes of low sampling rates.

- **Linear MPC**

Considering the proposed control framework *ESO-Koopman-MPC*, a LMPC is formulated since the dynamical model identified based on the Koopman operator theory is guaranteed to be linear. The discrete format of LMPC is presented as below,

$$\min_{u_i} J((u_i)_{i=0}^{N_p-1}, (\hat{x}_i)_{i=0}^{N_p}) \tag{4-3}$$

subject to

$$\hat{x}_{i+1} = A\hat{x}_i + Bu_i, \quad i = 0,1,...,N_p - 1 \tag{4-4a}$$

$$E_i\hat{x}_i + F_iu_i \le b_i, \quad i = 0,1,...,N_p - 1 \tag{4-4b}$$

$$E_{N_p}\hat{x}_{N_p} \le b_{N_p} \tag{4-4c}$$

parameter $$\hat{x}_0 = x(t_k) \tag{4-4d}$$

where $N_p = N_c$ and the objective function in (4-3) is often a convex quadratic programming problem involving the tracking performances and the control efforts,

$$J((u_i)_{i=0}^{N_p-1},(\hat{x}_i)_{i=0}^{N_p}) = \hat{x}_{N_p}^T Q_{N_p} \hat{x}_{N_p} + q_{N_p}^T \hat{x}_{N_p} + \sum_{i=0}^{N_p-1} (\hat{x}_i^T Q_i \hat{x}_i + u_i^T R_i u_i + q_i^T \hat{x}_i + r_i^T u_i) \tag{4-5}$$

with $Q_i \in R^{n\times n}$ and $R_i \in R^{m\times m}$ being positive semidefinite matrices. The matrices $E_i \in R^{n_c\times n}$ and $F_i \in R^{n_c\times m}$ as well as the vector $b_i \in R^{n_c}$ define the state and control input constraints, and n_c is the number of linear constraints. The optimization problem at time t_k is parameterized by the current measurement $x(t_k)$. If $(u_i^*)_{i=0}^{N_p-1}$ is the optimal solution to (4-3~4-5), the feedback controller is

$$\kappa(x(t_k)) = u_0^* \tag{4-6}$$

4.1.3 Dense Form of Linear MPC

We assume the matrices $A \in R^{n\times n}$ and $B \in R^{n\times m}$ are identified by DMDc, and n is the number of available measurements. For some cases like epidemiology, neuroscience, and video processing [60], the dimension of the optimization problem of LMPC is quite high. In this subsection, it is clarified that the computational complexity of solving the LMPC problem (4-3~4-5) can be rendered independent of the dimension of the measurements n, [61]. This is achieved by reorganizing the problem into the so-called ***dense form***,

$$\min_{U\in R^{mN_p}} U^T H U + h^T U + \hat{x}_0^T G U \tag{4-7}$$

subject to

$$LU + M\hat{x}_0 \le c \tag{4-8a}$$

parameter $$\hat{x}_0 = x(t_k) \tag{4-8b}$$

where $U \in R^{mN_p}$ is the column concatenation of the control sequence

$u_i \in R^m$, $i = 0,1,...,N_p - 1$; $H \in R^{mN_p \times mN_p}$ is a positive-semidefinite matrix and the other vectors and matrices involve $h \in R^{mN_p}$, $G \in R^{n \times mN_p}$, $L \in R^{(N_p+1)n_c \times mN_p}$, $M \in R^{(N_p+1)n_c \times n}$ and $c \in R^{(N_p+1)n_c}$.

The matrices and vectors in (4-7~4-8) are defined below,

$$\begin{aligned} &\tilde{Q} = diag(Q_0, Q_1, ..., Q_{N_p}) \in R^{(N_p+1)n \times (N_p+1)n}, \\ &\tilde{R} = diag(R_0, R_1 ..., R_{N_p-1}) \in R^{N_p m \times N_p m} \\ &\tilde{E} = diag(E_0, E_1, ..., E_{N_p}) \in R^{(N_p+1)n_c \times (N_p+1)n} \end{aligned} \tag{4-9a}$$

$$\begin{aligned} &\tilde{A} = \begin{bmatrix} I_{n\times n} \\ A \\ A^2 \\ \vdots \\ A^{N_p} \end{bmatrix} \in R^{nN_p \times nN_p}, \tilde{B} = \begin{bmatrix} 0_{n\times m} & 0_{n\times m} & \cdots & 0_{n\times m} \\ B & 0_{n\times m} & \cdots & 0_{n\times m} \\ AB & B & \cdots & 0_{n\times m} \\ \vdots & \ddots & \ddots & \\ A^{N_p-1}B & \ldots & AB & B \end{bmatrix} \in R^{(N_p+1)n \times N_p m} \\ &\tilde{F} = \begin{bmatrix} F_0 & 0 & \ldots & 0 \\ 0 & F_1 & \ldots & 0 \\ \vdots & & \ddots & \vdots \\ 0 & 0 & \ldots & F_{N_p-1} \\ 0 & 0 & \cdots & 0 \end{bmatrix} \in R^{(N_p+1)n_c \times N_p m} \end{aligned} \tag{4-9b}$$

$$H = \tilde{B}^T \tilde{Q} \tilde{B} + \tilde{R} \in R^{N_p m \times N_p m}, \quad G = 2\tilde{A}^T \tilde{Q} \tilde{B} \tag{4-9c}$$

$$\tilde{r} = [r_0^T, r_1^T, \cdots r_{N_p-1}^T]^T \in R^{N_p m}, \quad \tilde{q} = [q_0^T, q_1^T, \cdots q_{N_p}^T]^T \in R^{(N_p+1)n} \tag{4-9d}$$

$$h = \tilde{r} + \tilde{B}^T \tilde{q}, \quad c = [b_0^T, b_1^T, \cdots b_{N_p}^T]^T \in R^{(N_p+1)n_c} \tag{4-9e}$$

$$L = \tilde{F} + \tilde{E}\tilde{B}, \quad M = \tilde{E}\tilde{A} \tag{4-9f}$$

The optimization is over $U \in R^{N_p m}$ and the dense form is derived from the "sparse form" in (4-3~4-5) by solving the predictions $\hat{x}_i$ explicitly and concatenating the point-wise-in-time stage costs and the constraints. Notice that the sizes of matrices H, L and vectors h, c

are independent of the dimension of $x(t_k)$. Hence, the computational burden of the online optimization problem is comparable to solving a standard LMPC on the same prediction horizon N_p and the same dimension of the control inputs m, but has nothing to do with the states order n. Importantly, all these matrices and vectors in (4-9) are fixed and can be precomputed offline before deploying the controller (with exception of the inexpensive matrix-vector multiplications $\hat{x}_0^T G$ and $M\hat{x}_0$), [61].

4.2 ESO-Koopman-MPC

Recently, several works have been conducted to integrate ESO into the design of MPC.

- Ref. [62] proposed an MPC solution, assisted by ESO for the common rail pressure control in gasoline engines, where the discrepancy of the model from the real plant is estimated by ESO and then mitigated in the MPC structure. The "total disturbance" is assumed to be constant in the prediction horizon.
- The internal and external disturbances in a direct-drive permanent magnet synchronous generator (PMSG)-based wind energy conversion system (WECS) are attenuated with ESO in [63]. The ESO-based MPC approach realized a maximum power point tracking strategy with the system parameter variations and uncertain wind speeds considered.
- Ref. [64] deals with the tracking problem of a quadrotor helicopter with wind disturbances by an ESO-based MPC, and ref. [65] applied the same design in the case of a tractor-trailer vehicle suffering from inaccessible system states and uncertain disturbances.
- The convergence of the ESO estimation errors and stability of the ESO-based MPC are

proved when the disturbance is time-varying in [66].

4.2.1 Schematics of ESO-Koopman-MPC

As mentioned in Section 3.4.2, the discrepancy between the model identified by DMDc and the real plant is estimated by multi-channel ESO, which is assumed as a constant in the LMPC prediction horizon. The embedding of the ESO-compensated Koopman theory-based system identification into the MPC structure formulates ***ESO-Koopman-MPC (EKM)***. ESO-Koopman-MPC (EKM) is completely data-driven with no mathematical modeling procedures or any requirement of pre-knowledge about the studied system (pre-knowledge (if exists) should be exploited in the system identification and ESO design). The schematics of the overall EKM is presented in Figure 4-2.

The model-plant discrepancy d_k in the predictive model keeps being updated adaptively at each control step by the multi-channel ESO. The estimated model-plant mismatch is assumed to be constant in the MPC prediction horizon, and the MPC problem is parameterized by the real-time measurement $x(t_k)$. Notice that, crucially, the MPC problem formulated is a quadratic programming problem owing to an appropriate objective function, linear constraints on the inputs and states, and most importantly, the linear dynamical model identified based on the Koopman theory even if the underlying process is highly nonlinear. Since the quadratic programming problem is convex, rapid numerical solvers are thus allowed to realize real-time implementations.

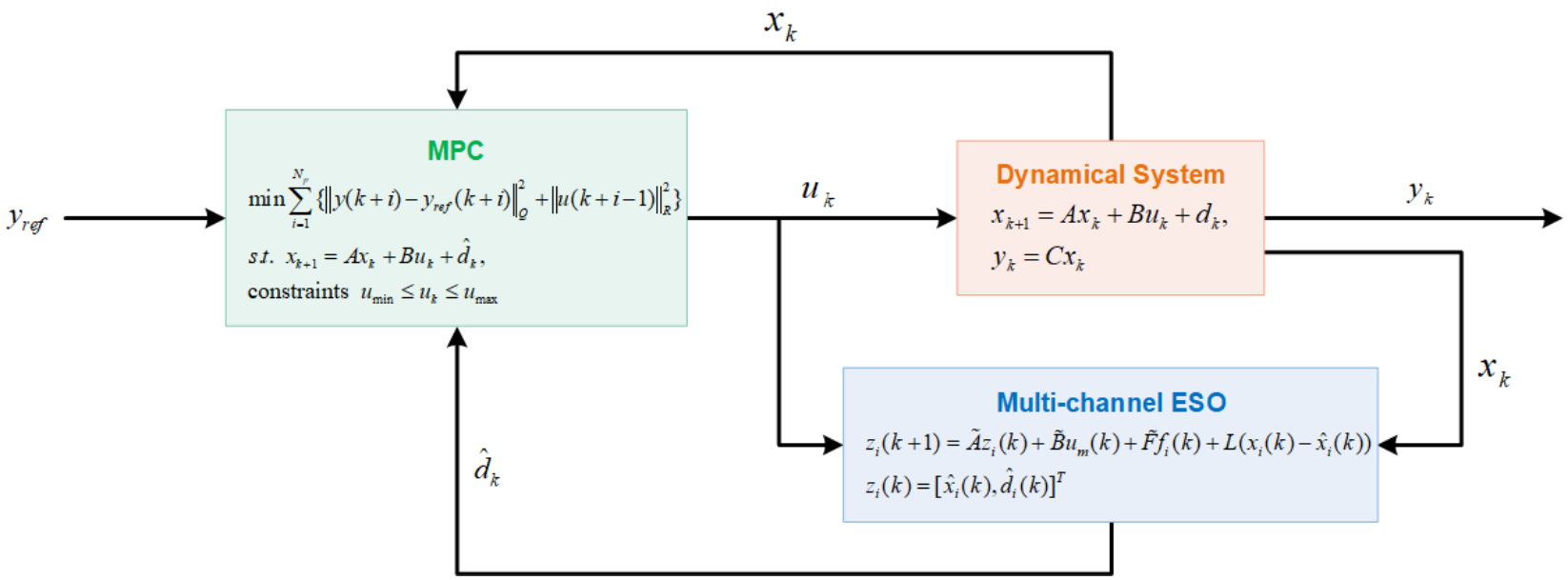

Figure 4 - 2 Schematics of ESO-Koopman-MPC

4.2.2 ESO-Koopman-MPC Online Algorithm

The algorithm of ESO-Koopman-MPC is summarized as follows.

Algorithm: **ESO-Koopman-MPC**

Require: A, B identified via DMDc from the collected data, bandwidth Ω_0 of the multi-channel ESOs

Initialize: Set the time index $k = 0$;

Initialize the state vectors of the multi-channel ESOs $z_q(0), q = 1, 2, ..., n$

While the control process is not terminated ***Do***

- Obtain the system measurements $x(t_k)$ and the related references;
- Solve the LMPC optimization problem (4-3~4-5) online with measured $x(t_k)$ and the disturbance vector $d(k)$ estimated by multi-channel ESOs to achieve an optimal control sequence $(u_i^*)_{i=0}^{N_p-1}$;
- Apply the first element in the optimal sequence u_0^* to the underlying dynamical system;
- Estimate $d(k+1)$ based on u_0^* and $x(t_k)$ by Eqn. (3-47);
- Update $k \leftarrow k+1$;

End

---

* For cases where the sampling rate is low, DESO of *current discrete estimator* form in 3.4.1 can be utilized to improve the estimation accuracy and enhance the control stability.

Chapter 5

Data-Driven Controller Design for Power System Oscillation Damping

The expected tremendous growth of power systems needed to integrate renewable sources and storage significantly increases the system complexity and poses challenges on the security and reliability of the power supply. A major root cause of large-scale power system blackouts is poorly damped or unstable electromechanical oscillations, which are inherent to the interconnected power systems [67]. Generator excitation control is one of the most effective measures widely applied to enhance system stability. Indeed, due to multiple factors including but not limited to the rapid expansion of the power grid, the adoption of new transmission technology, the high share of intermittent and uncertain renewable energy sources (RESs) [68], the provision of adequate damping remains a vital research challenge [69, 70].

Particularly, ***automatic voltage regulator (AVR)*** and ***power system stabilizer (PSS)*** have been extensively used as generator excitation controllers to enhance the power system oscillations damping in the power system industry. These conventional controllers are usually based on local linearization of a detailed dynamic model of the power grid. This method is perhaps suitable for small and moderate scale power systems but is impractical

for modern bulk power systems, especially when the operating conditions vary with the system configuration and the load levels in a complex manner [71, 72].

To this end, this chapter proposed a completely data-driven power system oscillation damping controller design based on the ESO-Koopman-MPC framework in the last chapter. The system dynamics are extracted from measurements of the observables and applied to the synthesis of control actions in an equation-free manner without requiring explicit knowledge about the underlying power network.

Two damping control strategies are explored, viewing different components of the system as the entity to be controlled:

- Integration of AVR and PSS
- Only PSS

The performances of the novel data-driven damping controllers are compared with the conventional model-based AVR and PSS on multiple test platforms, e.g., single machine infinite bus system (SMIB), Kundur two-area system, and IEEE-39 bus system. The simulation results verify the enhanced oscillation damping performances and voltage regulation abilities of the data-driven controllers.

5.1 Power System Oscillations

The modern power grids across the world are growing tremendously fast to cater to the increasing power needs of massive consumers, which results in the interconnections of multiple existing and newly developed power networks. The concerns regarding the power oscillation instabilities are more pronounced in the interconnected power networks [73]. If the power system oscillations are not tackled appropriately, the oscillations may turn

toward large-area voltage collapse and even cause blackouts like the western system coordinating council blackout [74] and the US-Canada blackout [75], etc.

Commonly observed and analyzed power system oscillations are defined in [79], and Figure 5-1 displays a typical example of ambient, transient, and forced responses.

- **Ambient Response:** The response of the system to small random changes such as load variations.
- **Transient Response:** The response of the system when a sudden disturbance occurs.
- **Forced Response:** The response associated with an external input or a malfunctioning apparatus.

To make it clear, the type of oscillatory response studied in this chapter is the transient response. In the rest of this section, we first summarize the major causes of the power oscillations and present a classification of transient oscillations commonly observed. Secondly, the conventional power oscillations damping (POD) approach, deployment of local power system stabilizers (PSSs), is illustrated with different types of PSSs. Finally, the shortcomings of the conventional PSSs (CPSSs) are analyzed, and a brief literature review is given to summarize the techniques to improve the performances of CPSSs.

5.1.1 Major Causes of Power System Transient Oscillations

Due to the requirements of stable and reliable operation, power system oscillations and transient stabilities are extensively studied recently. Here, we summarized a list of major causes of the power system transient oscillations from related literature,

- *The wide deployment of rapid-responding, high-gain voltage regulator (AVR) and excitation systems in the automatic control of the generator terminal voltage.*

The fast-acting exciters pose a negative damping effect on the rotor oscillations induced by small disturbances such as random load variations [76].

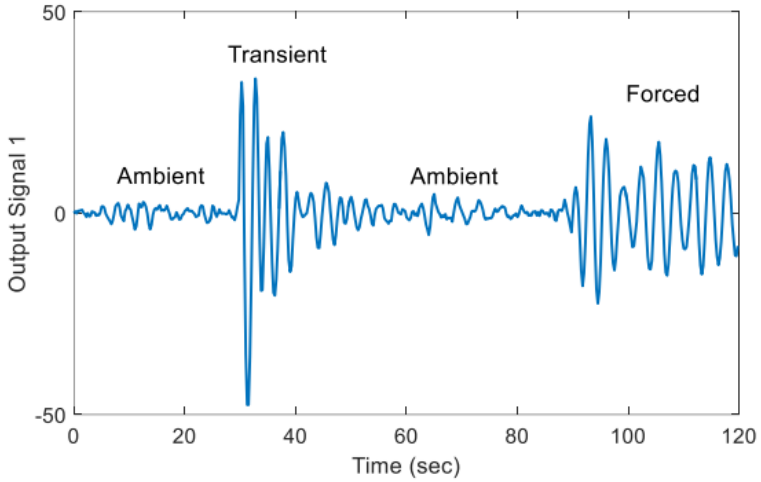

Figure 5 - 1 Example of Ambient, Transient, and Forced Responses

- *Interconnections of subsystems with the transmission of bulk power by weak tie-lines.*

The modern power network has large regional grids with different types of flexible and variable loads, generally distant from the generation resources. These regional grids are interconnected by long transmission lines with limited transmission capacity. A tie-line is termed "weak" if $P_{tie\ \max} \ll P_{ri}$ [77], where $P_{tie\ \max}$ represents the maximum real power to be transmitted via the line and P_{ri} is the per unit base value for all powers.

- *The increasing integration of RESs in power systems.*

The increasing growth of RESs like solar photovoltaic (PV), onshore wind, hydropower, etc., in power networks, leads to a reduction of the system's inertia, which degrades the transient stability and worsens the undamped small signal stability [78].

- *Sudden disturbances such as a short-circuit fault, transmission line tripping, generator tripping, or significant load variations.*

Transient oscillations are excited by emergency events and die out over short-time

intervals. Events like faults and trips on transmission lines, sudden losses of generation, and significant load variations, can cause transients visible at the transmission level.

5.1.2 Classification of the Power Transient Oscillations

Small signal stability can be used to describe the oscillatory modes related to the excitation system. These oscillations are damped as much as possible to achieve a stable and reliable operation. Depending on the oscillation frequency [80], transient power oscillations are classified into four types.

I. Local machine/Unit system oscillation [0.7-3.0Hz]

This type of oscillation refers to the case when one or more synchronous generators in a specific power station swing together against the rest of the power system or the load center. This oscillatory mode may induce severe results in power plants with high loads and reactance tie-lines. CPSS is recommended to deal with local mode oscillations.

II. Inter/Wide-area oscillation [0.1-0.7Hz]

Inter/wide-area oscillations occur when a group of generators in a single area swing against a second group of generators located in another area. To damp wide-area oscillations, it is necessary to apply a reliable control and monitoring system, such as PSSs, to guarantee the stability of large-scale power networks [81].

III. Inter-unit/Plant oscillation [1.5-3Hz]

When two or more synchronous machines in the same generation plant or the nearby plants swing against each other, the oscillation mode is called the inter-unit/plant oscillation, whose damping relies on the PSS re-tuning.

IV. Torsional oscillation [> 5Hz or > 10Hz]

Torsional oscillation usually occurs in steam-driven systems. The oscillatory mode takes place within rotating elements of the generation unit, such as synchronous machines, turbine stages, or rotating exciters mounted on the same shaft. The frequency is usually higher than 10 Hz for turbines with 3600 rpm and about 5 Hz for those with 1800 rpm [78]. Multi-band PSSs (MB-PSSs) are generally applied to damp the torsional oscillations.

5.1.3 Structure of Conventional PSSs

CPSSs are mostly single-loop local controllers, which use the rotor speed deviation ($\Delta\omega$), frequency, electrical power (P_e) or a combination of these locally available variables as the input signal. The objective of PSS is to provide additional damping torque by generating a supplementary control signal for the excitation system. The control diagram of a single generator with PSS is depicted in Figure 5-2. The input signal of CPSS depends on the type of PSS, and the output of the PSS is used to regulate the reference fed into AVR. The parameters of the lead-lag compensators in PSS are determined based on a small set of linearized models around critical operating conditions.

CPSSs, proposed in the 1960s, are generally designed with the phase compensation techniques in the frequency domain and implemented by washout (high-pass) filter and a series of lead-lad compensators. In this subsection, several widely used CPSSs structures are presented and explained.

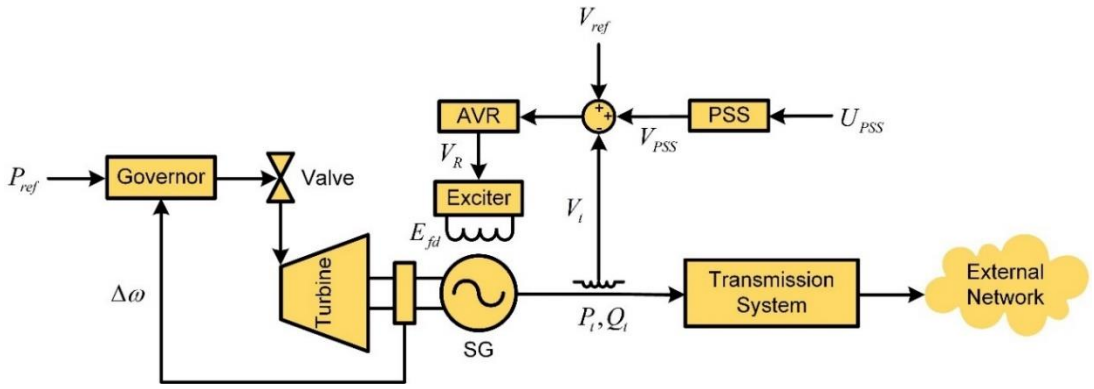

Figure 5 - 2 Control Diagram of a Single Generator

- **Classical Single Input PSS**

The input of single-input PSS can be the rotor speed, frequency signal, or the acceleration power, with the block diagram displayed in Figure 5-3. The rotor speed signal is inherently sensitive to torsional oscillations, so a torsional filter is utilized, or an average speed is used when more than one operating unit exits. The frequency signal is less sensitive to torsional oscillations but is prone to noises. Besides, acceleration power $\Delta P_a = P_m - P_e$ (difference of the mechanical power and the electrical power) is another option of the input signal and has the advantage of minimum lead compensation requirements.

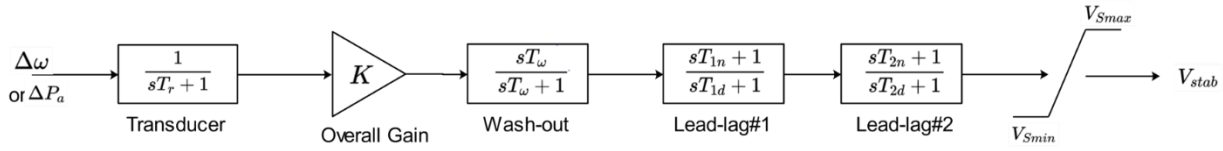

Figure 5 - 3 Block Diagram of Single Input-PSS

The wash-out block acts as a high-pass filter and works to eliminate steady-state bias in the input signal since PSS is expected to only respond to transient variations. The two lead-lag compensators are used to provide a phase lead for the input signal in the frequency range of interest so that the output of PSS is in phase with the rotor speed change.

- **Integral of Accelerating Power-based Stabilizer**

Single-input PSS has many limitations. Instead, a structure called IEEE PSS2B [82] is proposed with two inputs: rotor speed $\Delta\omega$ and the electrical power P_e, shown in Figure 5-4. Three lead-lag compensators are used in this design, and thus the parameters contain six independent time constants.

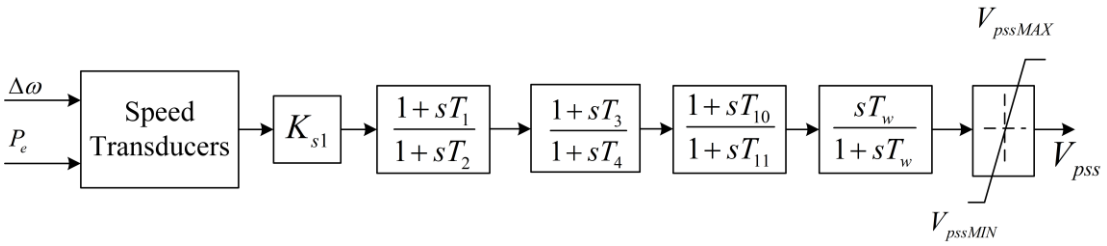

Figure 5 - 4 IEEE PSS2B Structure

- **Multi-Band PSS (MB-PSS)**

The main limitation of the single-input and dual-input PSSs mentioned above is the incapability to deal with a wide range of critical frequencies. Multi-Band PSS (MB-PSS) is proposed to solve this problem, and as its name indicates, MB-PSS structure is based on multiple working bands (see Figure 5-5) of (i) low-frequency band; (ii) intermediate-frequency band; (iii) high-frequency band.

A representative example of MB-PSS is IEEE PSS4B [82], where the input signal of the high-frequency band is the electrical power P_e. PSS4B provides an additional degree of freedom to achieve robustness and optimal tuning over frequencies of interest but at the expense of a cumbersome tuning process.

5.1.4 Shortcomings of CPSSs and Recent Developments

The parameters of CPSSs are chosen to provide adequate damping of all critical modes

under various operating conditions (e.g., full load conditions, weak AC system). The parameters are determined based on a small set of linearized models around these operating conditions. However, emerging power systems tend to operate over a wide range of conditions, with the system configuration, parameters, and load levels varying in a complex and uncertain manner. This leads to the concern that the damping effects of CPSSs may degrade under such a highly dynamic operating environment.

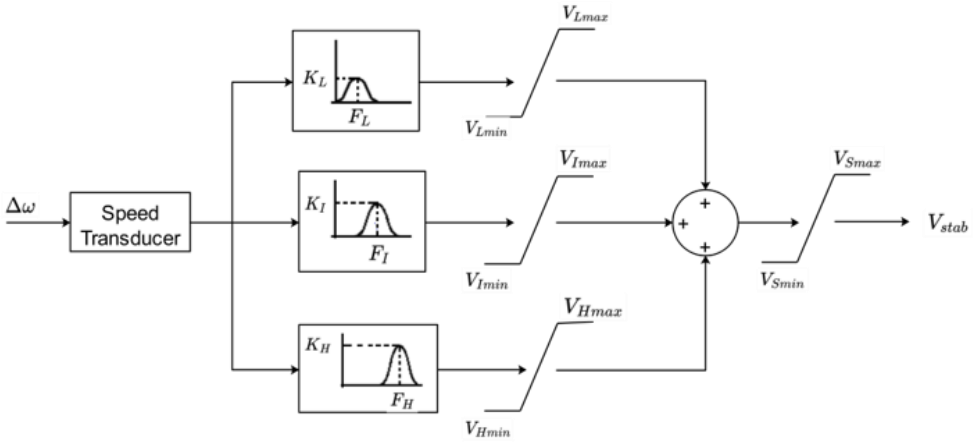

Figure 5 - 5 MB-PSS Conceptual Representation

To improve the adaptability of CPSSs, many techniques are proposed to refine the design or parameters turning, such as neural networks [83, 84, 85], fuzzy logic [86], intelligent optimization algorithms (e.g., simulated annealing, genetic algorithm, evolutionary programming, particle swarm optimization and tabu search) [87, 88, 89, 90, 91] and synergetic control theory [92]. For more studies using nonlinear techniques and variable control, the reader is referred for an extensive review in [78].

The majority of the previous advanced designs assume an available mathematical model of the system under control. However, the high-accuracy modeling task is made progressively more challenging in the industrial practice with the high share of renewable

energy resources (RESs), undocumented alternations of components, and models existing only in the form of tabulated data or computer code (see Chapter 1). The development of ICT in power systems makes vast quantities of data accessible; accordingly, data-driven analysis has the potential to revolutionize how the modern power grid is modeled, monitored, and controlled. Therefore, our proposition, the pure data-driven ESO-Koopman-MPC control framework, has great potential to be applied in the power system oscillations damping controller design.

5.2 Oscillation Damping Control Strategies and Data Collection

This section presents two control strategies of the oscillation damping controller design and illustrates the dynamical data collection procedures to prepare for the data-driven model identifications.

5.2.1 Two Control Strategies: Integration of AVR&PSS and PSS

The purpose of this dissertation is to find an effective and efficient control algorithm to regulate the generators voltages and damp out long-time persistent electromechanical oscillations in power systems. As depicted in Figure 5-2, AVR maintains the excitation field E_{fd} in the rotor windings to keep the terminal voltage V_t at the reference set-point V_{ref}. PSS generates a supplementary signal V_{pss} to provide additional damping torque to the rotor. In practice, both E_{fd} and V_{pss} have upper and lower limits.

For simplicity, the typical exciter dynamics in (5-1) are ignored, with the output of AVR V_R being equal to the excitation field E_{fd}.

$$E_{fd} = V_R \frac{1}{K_e + sT_e} \tag{5-1}$$

The single generator dynamical system with local control can be expressed by a set of differential-algebraic equations (DAEs) in (5-2).

$$\begin{aligned} \dot{x} &= f(x,u,v,\alpha) \\ 0 &= h(x,u,v,\alpha) \end{aligned} \tag{5-2}$$

where x consists of states of the generator and the primary regulators; u is the system inputs; v stands for algebraic variables and α represents system parameters. For the oscillation damping controller design, we consider the accessible measurements (observables) as

$$z = g(x) = [\delta, \Delta\omega, V_t, P_t, Q_t]^T \tag{5-3}$$

where $\delta(rad)$ is the rotor angle of the generator; $\Delta\omega(rad/s)$ is the rotor speed deviation; $V_t(pu)$ is the generator terminal voltage; $P_t(pu), Q_t(pu)$ are the terminal active and reactive power respectively. Note that the rotor angle typically cannot be measured directly but can be estimated from local measurements [93]. A most recent work [94] contains not only an effective algorithm for estimation of the generator angle δ, but also quantifies its performance under faults and for significant machine parameter mismatches.

To achieve a linear controlled system in the standard format of DMDc, the control variables in Figure 5-2 need to be specified and measured for the data-driven controller design. Two different control strategies shown in Figure 5-6 and Figure 5-7 are considered, viewing different components of the dynamical system as an entity to be controlled. The dynamical system under control is shadowed colorfully.

- Figure 5-6: **Integration of AVR and PSS (EKM AVR & PSS)**

  System input: $u = [P_{ref}, E_{fd}]^T$;

- Figure 5-7: **Only PSS (EKM PSS)**

  System input: $u = [P_{ref}, V_{ref}, V_{pss}]^T$

* EKM stands for ESO-Koopman-MPC

where P_{ref} is the active power reference for the turbine governor.

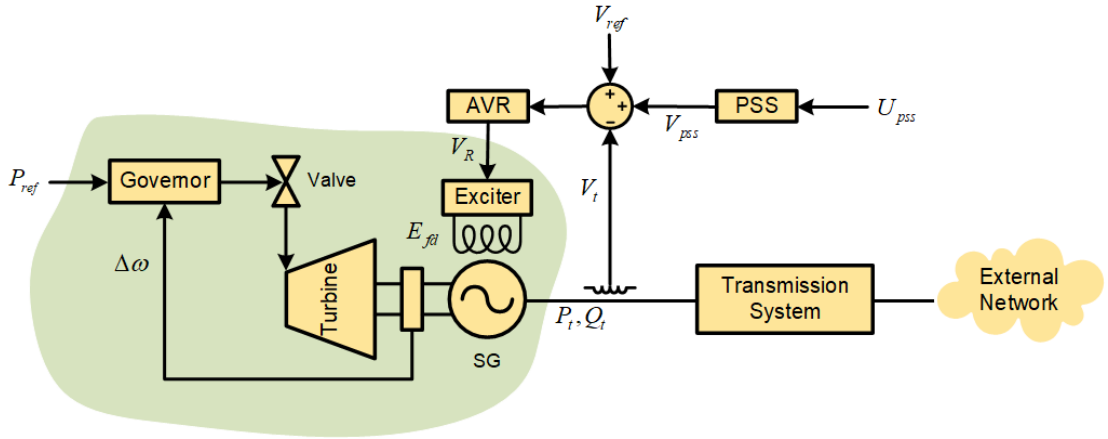

Figure 5 - 6 Oscillation Damping Controller of Integrated AVR & PSS

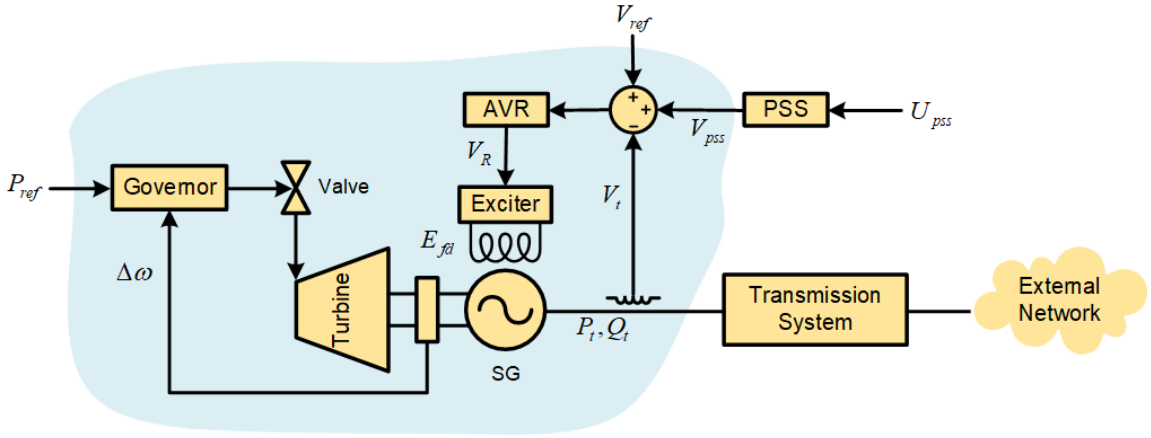

Figure 5 - 7 Oscillation Damping Controller of Only PSS

Among all the control variables in the two design strategies, only E_{fd} and V_{pss} are

tunable while P_{ref} and V_{ref} are supervised by secondary controls, which is beyond the scope of our work. For the integration of AVR and PSS in Figure 5-6, the controller generates the excitation field E_{fd} directly; thus, the system under control is the generator equipped with the mechanical power governor. As to the design of the control strategy of only PSS in Figure 5-7, both AVR and the turbine governor are assumed to be installed by default, and their dynamics are part of the controlled system.

5.2.2 The Dynamical Data Collection Procedures

To illustrate the data collection procedures, we consider the example of a single machine infinite bus system (SMIB) in Figure 5-8, where the synchronous machine applied is model 1.1 in [76] with the field circuit and one equivalent damper on the q-axis. Magnetic saturation is either neglected or considered by using saturated values of the mutual inductances. In most cases, the saturation effects are generally negligible when conducting dynamic simulations.

The synchronous machine equations are as follows,

$$\begin{cases} \dfrac{d\delta}{dt} = \omega_B (S_m - S_{m0}) \\ \dfrac{dS_m}{dt} = \dfrac{1}{2H}[-D(S_m - S_{m0}) + T_m - T_e] \\ \dfrac{dE_q^{'}}{dt} = \dfrac{1}{T_{d0}^{'}}[-E_q^{'} + (x_d - x_d^{'})i_d + E_{fd}] \\ \dfrac{dE_d^{'}}{dt} = \dfrac{1}{T_{q0}^{'}}[-E_d^{'} - (x_q - x_q^{'})i_q] \end{cases} \tag{5-4}$$

where all symbols in (5-4) are summarized in Table 5-1, and $S_m = \dfrac{\omega - \omega_B}{\omega_B}$ is the rotor speed deviation in pu; generally, the initial operating speed is equal to the nominal speed,

so $S_{m0}=0$. The electrical torque is expressed in terms of the state variables $E_d^{'}$, $E_q^{'}$ and non-state variables i_d, i_q,

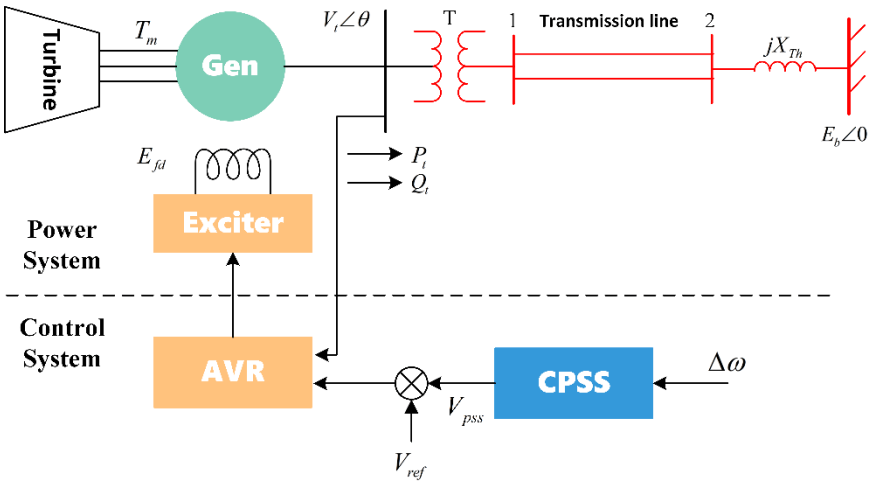

Figure 5 - 8 Block Diagram of Single Machine Infinite Bus (SMIB) System

$$T_e = E_d^{'} i_d + E_q^{'} i_q + (x_d^{'} - x_q^{'}) i_d i_q \tag{5-5}$$

where non-state variables i_d, i_q can be obtained by combining the stator algebraic equations and the external network equations. It is assumed that the external network connecting the synchronous machine to the infinite bus is linear two-port, and all loads are of constant impedance type. Ignoring the stator transients and rotor speed variations, the direct and quadratic-axis currents can be solved by the following nonlinear equations,

$$\begin{bmatrix} (x_d^{'} + z_I) & -(\mathrm{R}_a + \mathrm{Z}_R) \\ -(\mathrm{R}_a + \mathrm{Z}_R) & -(x_q^{'} + \mathrm{Z}_I) \end{bmatrix} \begin{bmatrix} i_d \\ i_q \end{bmatrix} = \begin{bmatrix} f_1(\delta) - E_q^{'} \\ f_d(\delta) - E_d^{'} \end{bmatrix} \tag{5-6}$$

$$f_1(\delta) = h_1 E_b \cos\delta + h_2 E_b \sin\delta,$$
$$f_2(\delta) = h_2 E_b \cos\delta - h_1 E_b \sin\delta$$

where $(z_R + jz_I)$ is the input impedance of the external network viewed from the generator terminal with the infinite bus shorted; $(h_1 + jh_2)$ is the voltage gain at the generator

terminal with the armature open; other variables can be found in Table 5-1.

Table 5-1 List of Synchronous Machine Symbols

ω_B	Base angular frequency (rad/s)
D	Mechanical damping coefficient of the generator (pu)
H	Inertial constant (sec)
T_m, T_e	Mechanical and electrical torque (pu)
$E_d^{'}$, $E_q^{'}$	Transient electro-motive force (EMF) in the quadratic/direct axis (pu)
$T_{q0}^{'}$, $T_{d0}^{'}$	Quadratic/direct-axis open-circuit transient time constant (sec)
i_d, i_q	Direct/quadratic-axis components of the armature current (pu)
x_d, x_q	Direct/quadratic-axis components of the synchronous reactance (pu)
$x_d^{'}, x_q^{'}$	Direct/quadratic-axis components of the transient reactance (pu)
R_a	Armature resistance (pu)
E_b	Infinite bus voltage (pu, $E_b = 1.0$)

The excitation system of the SMIB is a static exciter with a single time constant, represented as,

$$\frac{dV_R}{dt} = \frac{1}{T_A}[K_A(V_{in} - V_t) - V_R], \quad E_{fd\max} = 6,\ E_{fd\min} = -6 \tag{5-7}$$

with the input $V_{in} = V_{ref} + V_{pss}$. The PSS employed in SMIB is a $\Delta\omega$-PSS with one lead-lag compensator, and all parameters of this case can be found in the Appendix. SMIB Parameters Table. The system diagram of the SMIB is shown in Figure 5-9.

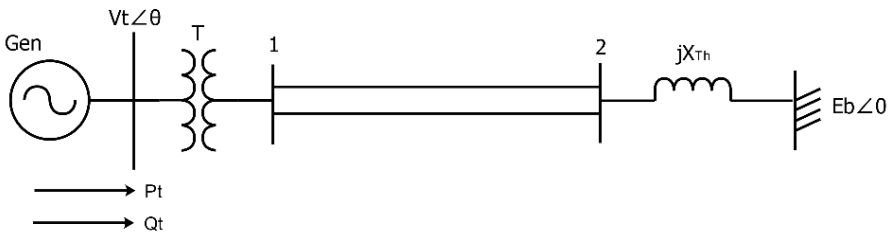

Figure 5 - 9 SMIB System Diagram

The steady-state operating conditions of the studied SMIB are determined by the loading status: transmitted active and reactive power P_t, Q_t [76]. To collect the system dynamics in a wide operating range, 100 initial settings of the power loadings are randomly selected from $P_t \in [0.2, 1.2], Q_t \in [-0.2, 0.2]$ (pu). After the system enters steady state, a short-term pulse disturbance is exerted on V_{ref} and measurements in (5-3) together with the control signals for two different control strategies are sampled in 2 sec post-disturbance in a sampling rate of $\Delta T = 1/25\text{s}$, as shown in Figure 5-10. In the case of SMIB, the voltage reference disturbance lasts for 10 cycles ($f_B = 50Hz$) and for each loading status, we apply $\Delta V_{ref} \in [\pm 0.02, \pm 0.04, \pm 0.06]$ respectively. Therefore, 600 trajectories with different initial conditions and disturbances are acquired and organized to be the measurement matrix $Z \in R^{5\times 30000}$ and the control input matrix $U \in R^{2\times 30000}$ (EKM AVR & PSS) or $U \in R^{3\times 30000}$ (EKM PSS) on which DMDc is implemented. The matrix column dimension 30000 is the number of snapshots of the dynamical system.

The collected representative trajectories are displayed in Figure 5-11. Since the SMIB model considered does not include a prime mover, the mechanical torque T_m is sampled instead of the power reference P_{ref} due to the incomplete modeling. The data acquisition procedures can be extended to multi-machine systems on each generation unit, e.g., Kundur

two-area system and IEEE 39-bus system in a straightforward way. Different from SMIB, the initial conditions of the multi-machine system are derived from randomly selected power reference $P_{ref} \in [0.2,1.2]$ and the voltage reference $V_{ref} \in [0.9,1.1]$ for each synchronous machine to generate trajectories over a wide range of operating conditions. The hyperparameters for the data collection on various test benchmarks are contained in Table 5-2. The disturbance to trigger the system dynamics is not limited to V_{ref} variations, as multiple fault scenarios like three-phase faults, load sheddings, and topological network changes are also optional.

Note that on the stage of data acquisition, it does not matter which type of CPSS or AVR is utilized, and any V_{pss} or E_{fd} would work. Even randomly generated control signals are effective as long as the dynamics of the system under control are excited [61]. Actually, DMDc is learning the (open-loop) system dynamics, but not the control actions when collecting dynamical data.

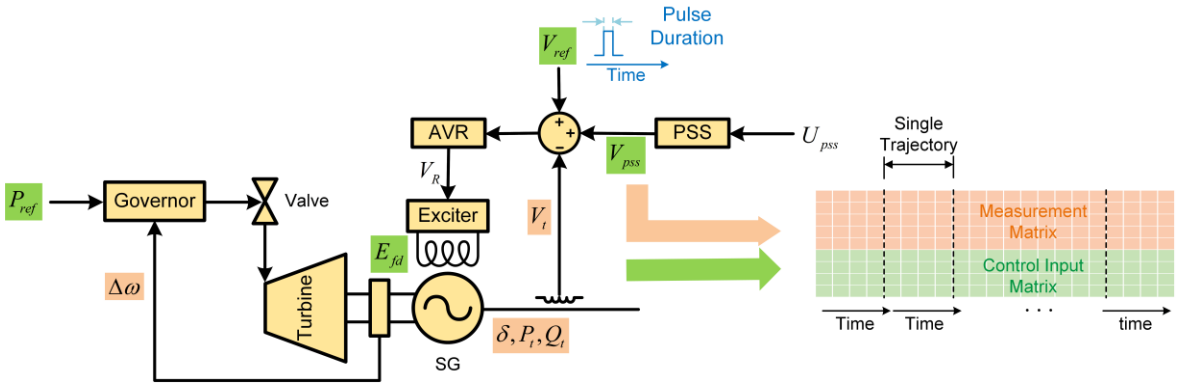

Figure 5 - 10 Data Collection under Voltage Reference Disturbances

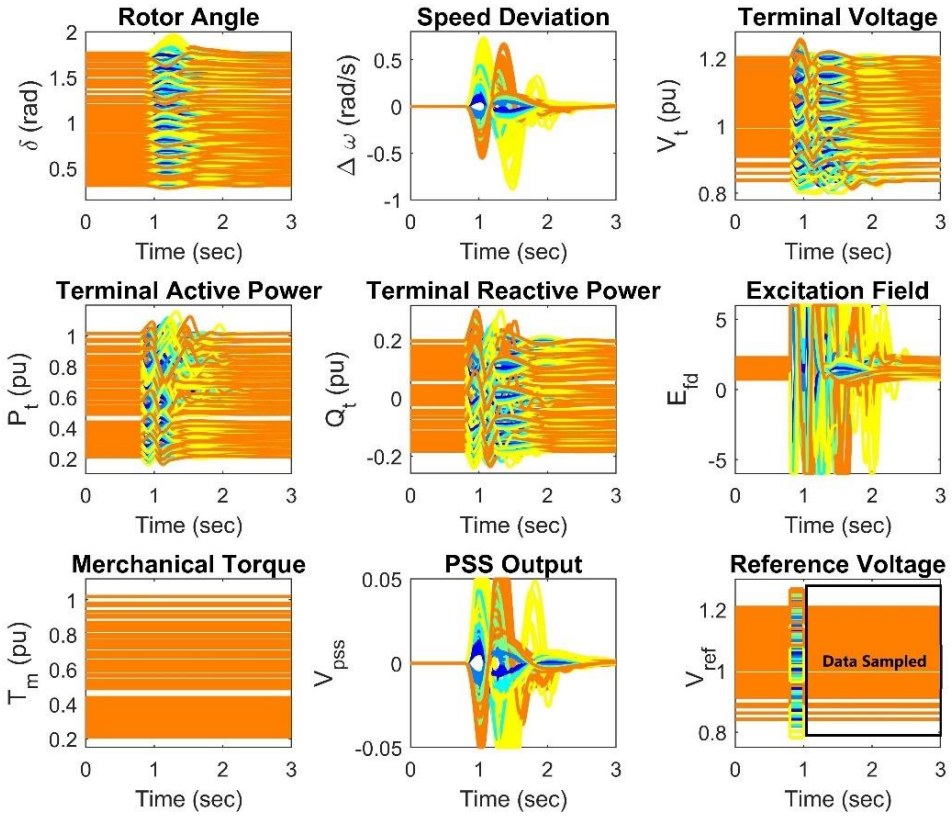

Figure 5 - 11 Collected Dynamical Trajectories of SMIB

5.3 Prediction Ability of the Identified Model

The collected dynamical data is divided into a training set (90%, 540 trajectories) and a test set (10%, 60 trajectories). Applying DMDc on the training set, a discrete-time linear model of the underlying complicated, nonlinear, and high-dimensional system is obtained. To check the prediction ability of the identified linear model, it is first utilized to predict the trajectories in the test set. We mainly focus on the prediction accuracies on the rotor speed deviation $\Delta\omega$ and the terminal voltage V_t, since they are essential variables involved in the MPC objective function of the proposed EKM-based damping controllers. Then, the identified model is further tested to predict trajectories under new disturbances different from those on the data collection stage.

Table 5-2 Data Collection Settings

	SMIB	Kundur Two-Area	IEEE-39 Bus
# of Initial Conditions	100	100	100
Base Frequency	50Hz	60Hz	60Hz
Disturbance ΔV_{ref}	$[\pm 0.02, \pm 0.04, \pm 0.06]$	$[\pm 0.02, \pm 0.04, \pm 0.06]$	$[\pm 0.05, \pm 0.10, \pm 0.15]$
Duration of ΔV_{ref}	10 Cycles	12 Cycles	12 Cycles
Sample Rate	25/sec	30/sec	30/sec
Post-disturbance Sample Duration	2 sec	5 sec	5 sec

5.3.1 Prediction Performances in SMIB

The mean absolute multi-step prediction error (MAE) of the terminal voltage V_t and the speed deviation $\Delta\omega$ across all test trajectories of SMIB are displayed in Figure 5-12, where the two control strategies demonstrate acceptable prediction accuracies. Although the prediction error is accumulated with prediction steps, relatively accurate predictions in a limited number of steps are solid enough to allow the application of MPC. Besides, the control strategy of integrating AVR and PSS enjoys a better prediction accuracy than the strategy of just the PSS. One possible reason is that the dynamical system studied by the PSS control strategy is more complicated since AVR is involved. To illustrate the dynamical prediction clearly, one trajectory from the test set is randomly picked, and multi-step predicted trajectories from some specified starting points are displayed in Figure 5-13.

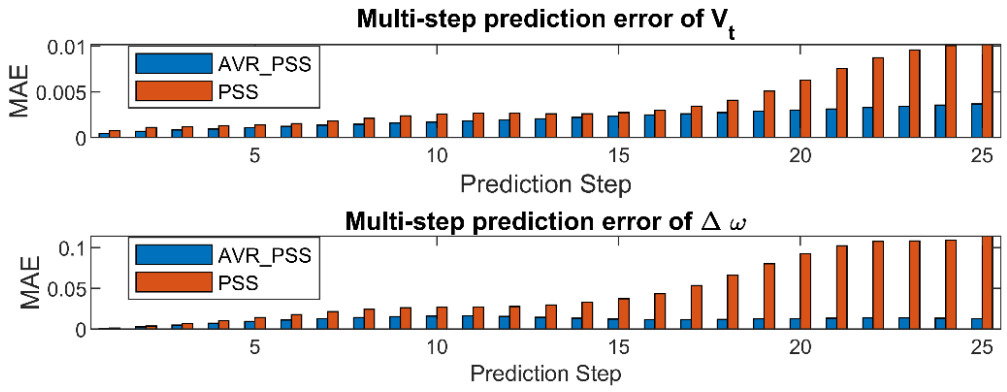

Figure 5 - 12 Mean Absolute Multi-Step Prediction Error of V_t and $\Delta\omega$ in SMIB

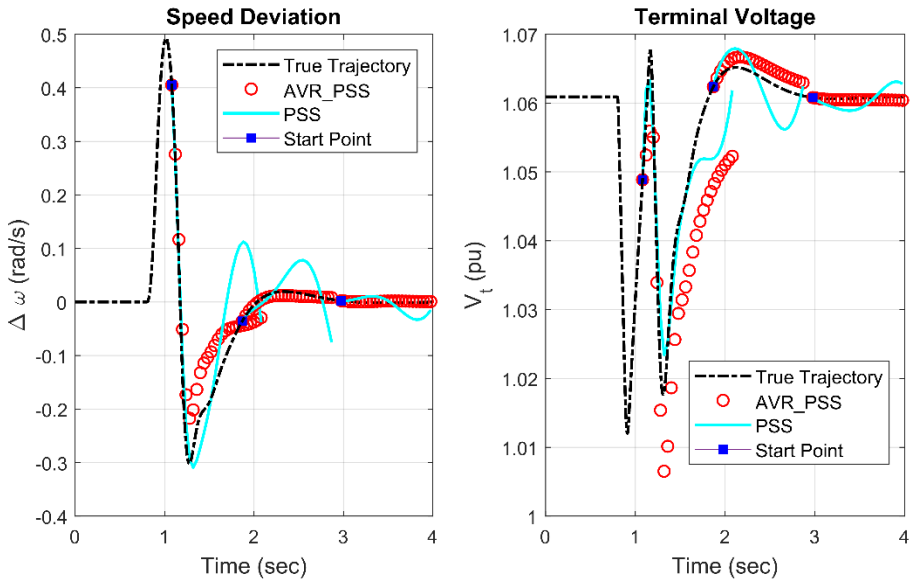

Figure 5 - 13 Prediction Performance (Test Set) of the Identified Models in SMIB

As shown in Figure 5-13, the identified linear models based on the two control strategies can both track the true trajectory well. Starting with a snapshot of measurements in (5-3), the identified model is assumed to keep receiving real-time control inputs and achieves consecutive predictions of the future measurements. The control strategy integrating AVR and PSS has a much lower prediction error on the speed deviation $\Delta\omega$ and the terminal voltage V_t compared to only PSS, which is consistent with the graphical statistical conclusion in Figure 5-12. To further investigate the prediction ability of the identified

model, new study cases with disturbances not involved in the training and test set are checked carefully. Here, we consider four scenarios listed below with the same initial condition in Appendix. SMIB Parameters Table, marked as “Test Initial Condition”.

- Test Scenario 1: Step increase of the voltage reference V_{ref} by 0.05 pu at t = 1s,
- Test Scenario 2: Step increase of the mechanical torque T_m by 0.1 pu at t = 1s,
- Test Scenario 3: Step increase of E_b by 0.1 pu at t =1s (E_b is the infinite bus voltage),
- Test Scenario 4: Three-phase fault at the sending end of one of transmission lines (two parallel transmission lines shown in Figure 5-9), followed by clearing at the end of 4 cycles (The faulted line connecting bus 1 and 2 is tripped) at t = 1s.

The prediction performances of the identified model under the test scenarios mentioned above are shown in Figure 5-14 to Figure 5-17, respectively. The predicted trajectories of the two control strategies under different disturbances are checked and compared. Same as before, the control strategy integrating AVR and PSS enjoys a much better prediction accuracy than the strategy of only PSS, especially for the transient dynamics. The prediction horizon is $N_p = 25$, and two control strategies considered here show acceptable prediction accuracies in the first few steps, which supports the combination with MPC.

Secondly, the first two scenarios (Figure 5-14, Figure 5-15) are examples of variations of external system inputs (reference), V_{ref} and T_m, but the system dynamics remain unchanged; while for scenarios in Figure 5-16 and 5-17, the system dynamics are different from that at the stage of data collection. For example, in scenario 4, the external network topology is altered after the faulted line is tripped. We believe that the active and reactive power P_t , Q_t can capture the influence of the external network on the controlled generator

to some extent. To summarize, the model identified with ΔV_{ref} pulse disturbances, has acceptable prediction ability even when it is extended to various test cases.

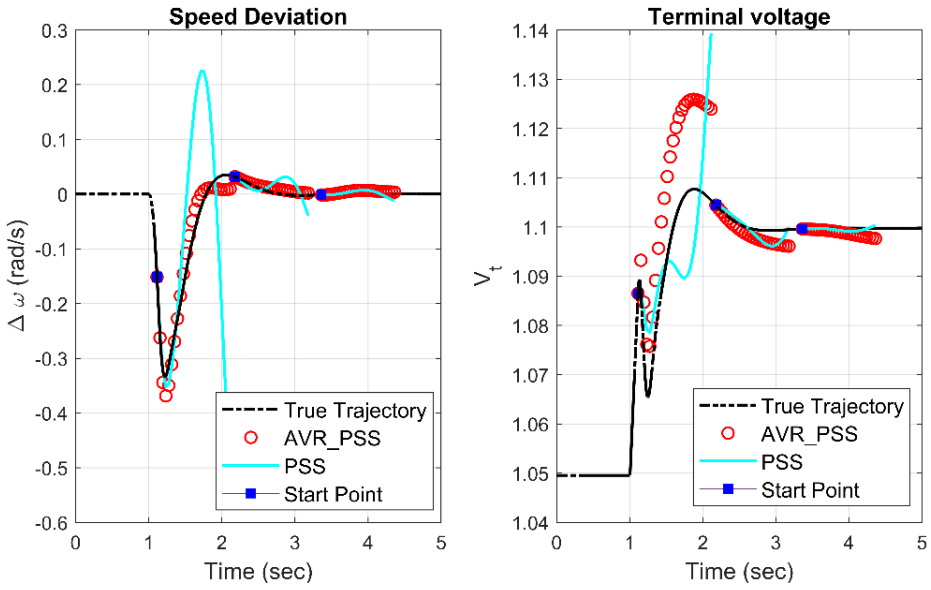

Figure 5 - 14 Prediction of Scenario 1: Voltage Reference Step Change

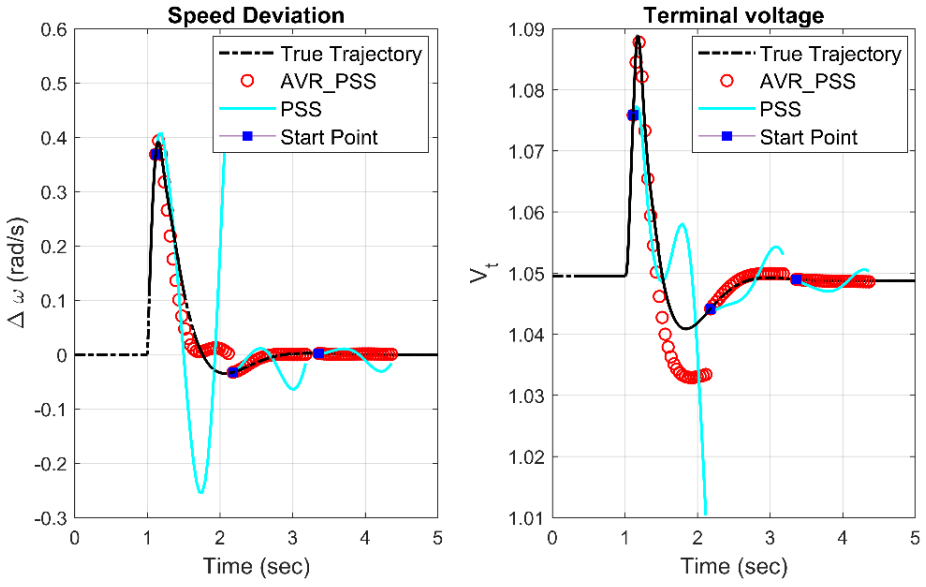

Figure 5 - 15 Prediction of Scenario 2: Mechanical Torque Step Change

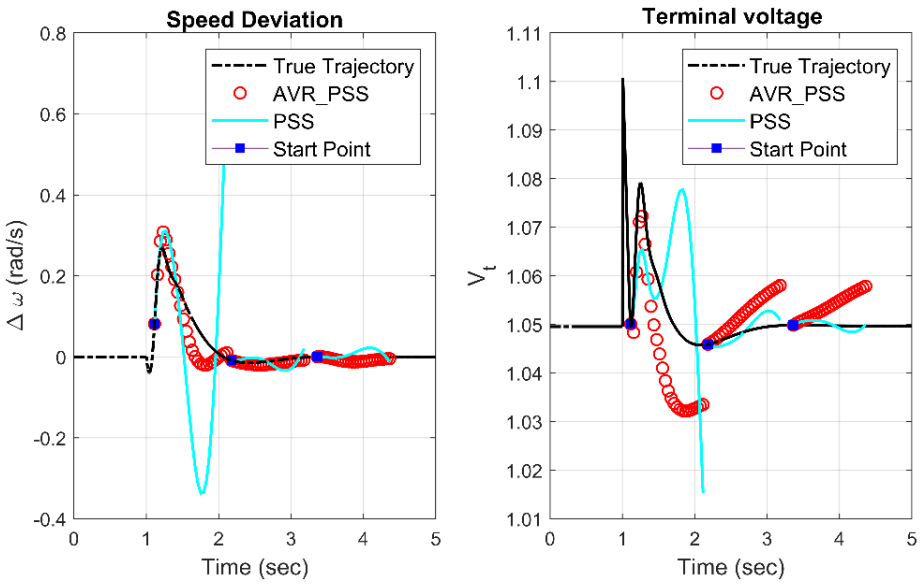

Figure 5 - 16 Prediction of Scenario 3: Infinite Bus Voltage Step Change

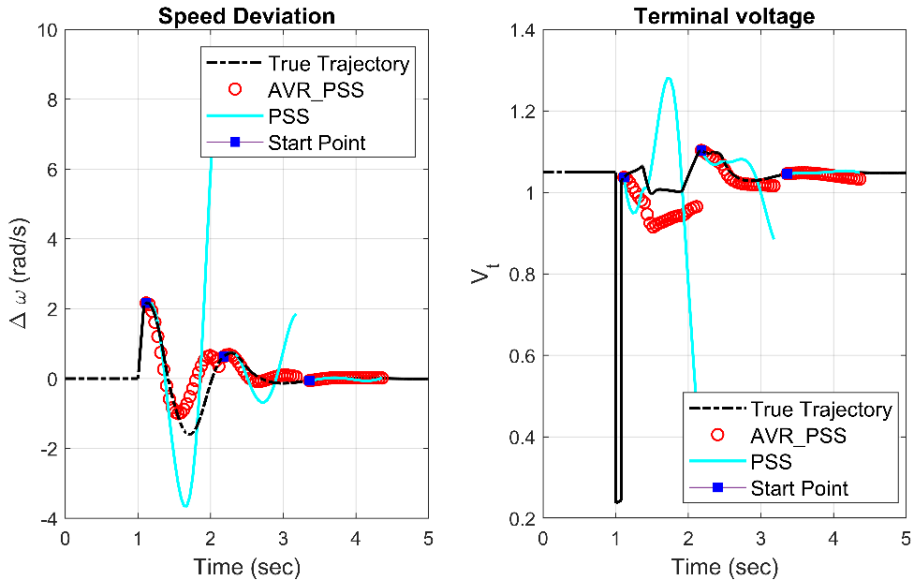

Figure 5 - 17 Prediction of Scenario 4: Three-phase Fault at One Transmission Line

On the other hand, the modeling error, which results in the deviation of the predicted trajectory from the true value, may degrade the transient dynamics and cause offset of reference tracking. To address the inevitable modeling inaccuracy, multi-channel ESO is embedded to estimate the mismatch from real-time system input and output measurements.

(see Chapter 3)

5.3.2 Prediction Performances on Multi-Machine Benchmarks

In addition to the SMIB system, the data collection and model identification are also conducted on multi-machine benchmarks: Kundur two-area system and IEEE 39 bus system. The modeling of the generation unit with local control is quite detailed and practical with a complete tandem-compound steam prime mover system, IEEE type-1 synchronous machine voltage regulator, and different types of CPSSs in the simulation environment of Simulink [95], [96]. The data collection hyperparameter settings are contained in Table 5-2.

- **Kundur Two-Area System**

Kundur two-area system was specifically designed to study low-frequency electromechanical oscillations in interconnected power systems. Two fully symmetrical areas linked together by two 230 kV lines of 220 km length, and each area is equipped with two identical round rotor generators rated 20 kV/900 MVA. The synchronous machines in the two regions have identical parameters, except for the generator inertias [69]. The load is represented as constant impedances and split between the areas so that area 1 is exporting 413MW to area 2, which makes the system somewhat stressed. The system diagram is displayed in Figure 5-18. The normal operating status for all generators is assumed as,

$$V_{ref} = [1.0, 1.0, 1.0, 1.0], P_{ref} = [0.777778\ 0.777689\ 0.798889\ 0.777778] \quad (5\text{-}8)$$

When collecting dynamical data, all generators are equipped with $\Delta\omega$-PSS, whose parameters can be found in [95]. Taking G1 as an example, its power and voltage references are randomly selected with $P_{ref,1} \in [0.2, 1.2], V_{ref,1} \in [0.9, 1.1]$ while the other generators

remain the initial settings in (5-8). In this case, G4 is chosen as the rotor angle reference. Same as before, the system model is identified based on the training set (90% data) and then verified on the test set (10% data). The average prediction error of G1 on the test set is demonstrated in Figure 5-19.

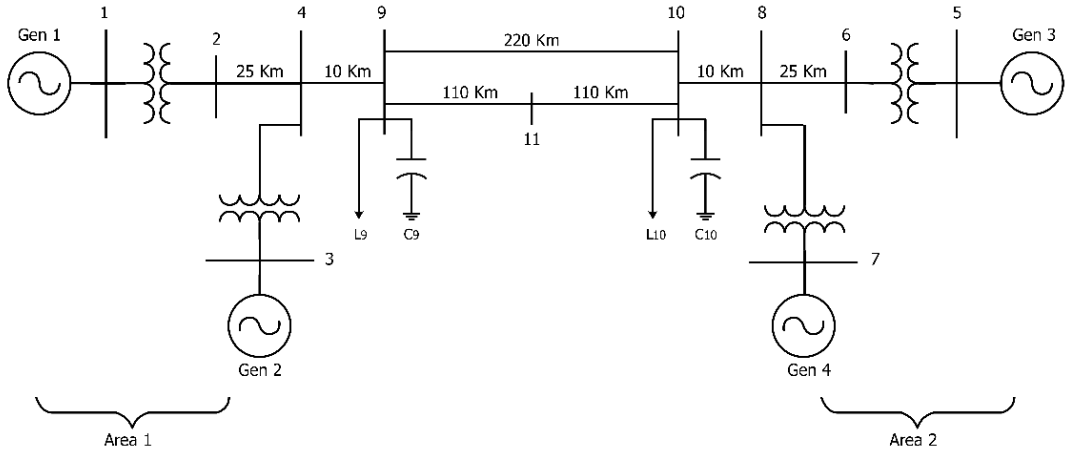

Figure 5 - 18 Diagram of Kundur Two-Area System

Compared with the prediction performances in Figure 5-12, the prediction accuracies of the two control strategies in Kundur two-area system do not display a significant difference. However, the prediction accuracies of V_t and $\Delta\omega$ are comparable to the case of SMIB. Again, one trajectory from the test set is chosen to illustrate the multi-step trajectory tracking performance of the identified models, shown in Figure 5-20 ($N_p = 30$). The control strategy integrating AVR and PSS displays a better trajectory tracking accuracy, especially for the transient process, and both control strategies enjoy great tracking performances when the system becomes steady. The identified models display acceptable prediction accuracies at least for the first few steps.

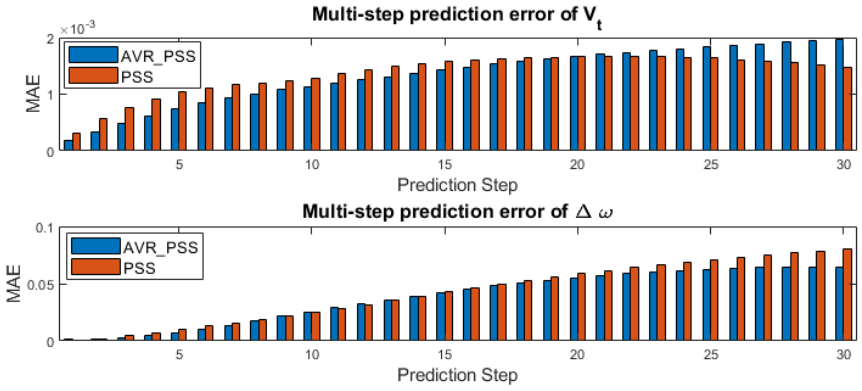

Figure 5 - 19 Mean Absolute Multi-Step Prediction Error on V_t and $\Delta\omega$ of G1 in Kundur Two-Area System

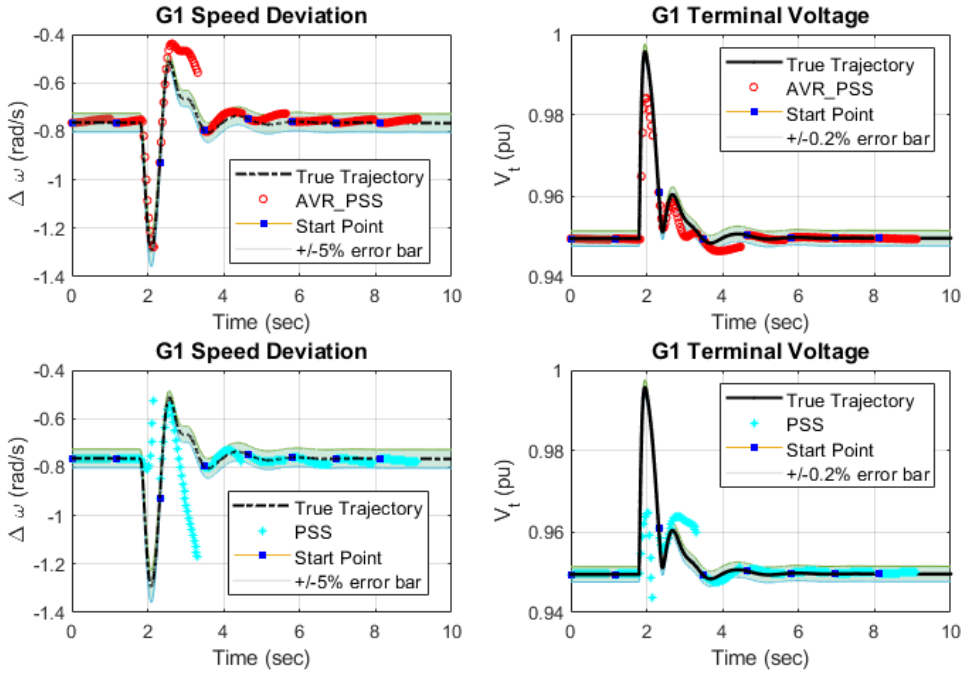

Figure 5 - 20 Multi-Step Trajectory Prediction of G1 in Kundur Two-Area System

- **IEEE-39 Bus System**

IEEE 39-bus system, commonly known as "the 10-machine New England Power System", has been extensively employed in the oscillation damping control studies. It consists of 10 generators and 39 buses, where G1 is an area-equivalent model representing the New York system to which the New England system is connected. The diagram of the system is shown

in Figure 5-21. The data acquisition procedures are implemented on G2 and G7 individually. The area-equivalent generator G1 is picked as the rotor angle reference. When collecting data, all generators are supplied with a multiband-PSS (MB-PSS) with typical settings. The parameters of generators, AVRs, $\Delta\omega$-PSSs, loads and other components can be found in [97].

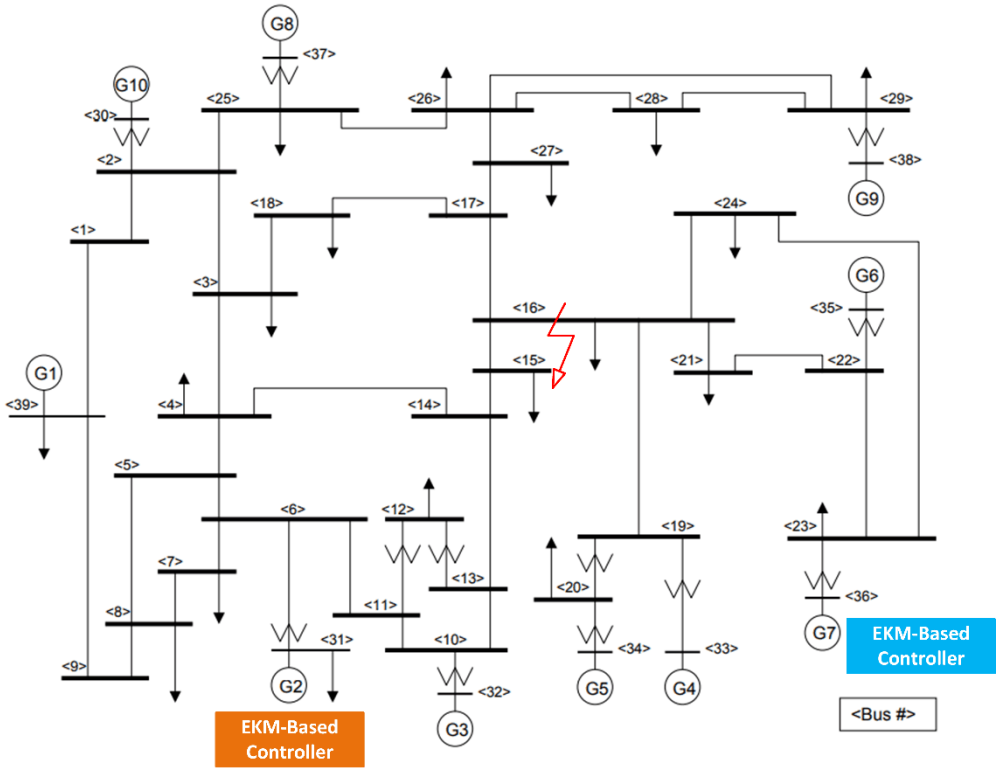

Figure 5 - 21 Diagram of IEEE-39 Bus Network

The linear model identified by DMDc from the training set is exploited to predict one trajectory randomly picked from the test set of G2 and G7 respectively, see Figure 5-22 and 5-23. The predictions of the speed deviation $\Delta\omega$ and the terminal voltage V_t of the two generators are quite accurate and mostly within the error bar range, +/-5% for $\Delta\omega$ and +/-0.2% for V_t. The modeling error may be larger when the identified model is applied to predict trajectories suffering other disturbances. Therefore, the proposed multi-channel

ESO is necessary to estimate the mismatch, which is then mitigated in the design of MPC-based damping controllers.

5.4 Data-Driven Oscillation Damping Controller Design

Revisiting the data-driven control framework in Chapter 4, the schematics of ESO-Koopman-MPC (EKM) is demonstrated in Figure 5-24. The control target of the oscillation damping controller in power systems involves two performance indexes:

(1) regulating the generator terminal voltage to V_{ref}, and

(2) the damping effect on the rotor speed deviation $\Delta\omega$.

Embedding the identified linear model by DMDc into the MPC structure, with the model-plant discrepancy or other uncertain disturbances (external forces or internal variations) estimated by a multi-channel ESO, the optimization problem of the novel power system oscillation damping controller is formulated as

$$\min_{(\tilde{u}_i)_{i=0}^{N_p-1}} \sum_{i=0}^{N_p} (\| \Delta\tilde{\omega}_i \|_{Q_w} + \| \Delta\tilde{V}_i \|_{Q_v}) + \sum_{i=0}^{N_p-1} \| \tilde{u}_i \|_R \tag{5-9}$$

subject to

$$\begin{aligned} &\hat{z}_{i+1} = A\hat{z}_i + Bu_i + \hat{d}_i \\ &\hat{z}_0 = g(x(t_k)) = [\delta(t_k), \Delta\omega(t_k), V_t(t_k), P_t(t_k), Q_t(t_k)]^T \\ &\tilde{u}_{\min} \le \tilde{u}_i \le \tilde{u}_{\max}, i = 0,1,...,N_p - 1 \\ &\hat{d}_{i+1} = \hat{d}_i, i = 0,1,...,N_p - 2 \end{aligned} \tag{5-10}$$

where $\Delta\tilde{\omega} = \Delta\hat{\omega} - \Delta\omega_{ref}$, $\Delta\tilde{V} = \hat{V}_t - V_{ref}$ denotes the rotor speed deviation and the terminal voltage tracking error respectively; the control input vector u_i involves the given (unchangeable) references and adjustable control variables depending on the control strategy; $\tilde{u}_i$ represents the adjustable variable E_{fd} or V_{pss} which is the optimization

variable in (5-9). The system measurements in (5.3) at time t_k are represented by $\hat{z}_0 = g(x(t_k))$, which are functions of the system states.

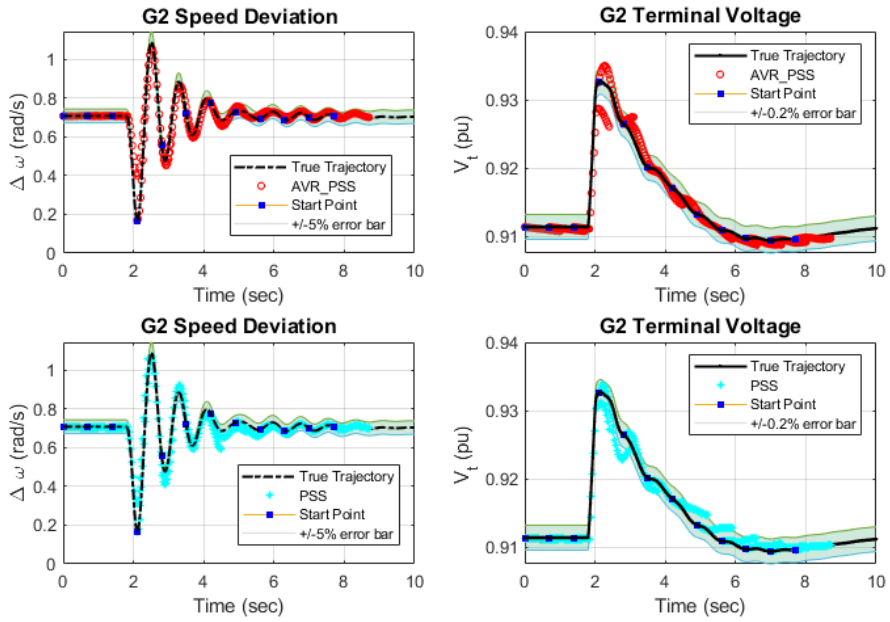

Figure 5 - 22 Multi-Step Trajectory Prediction of G2 in IEEE-39 Bus System

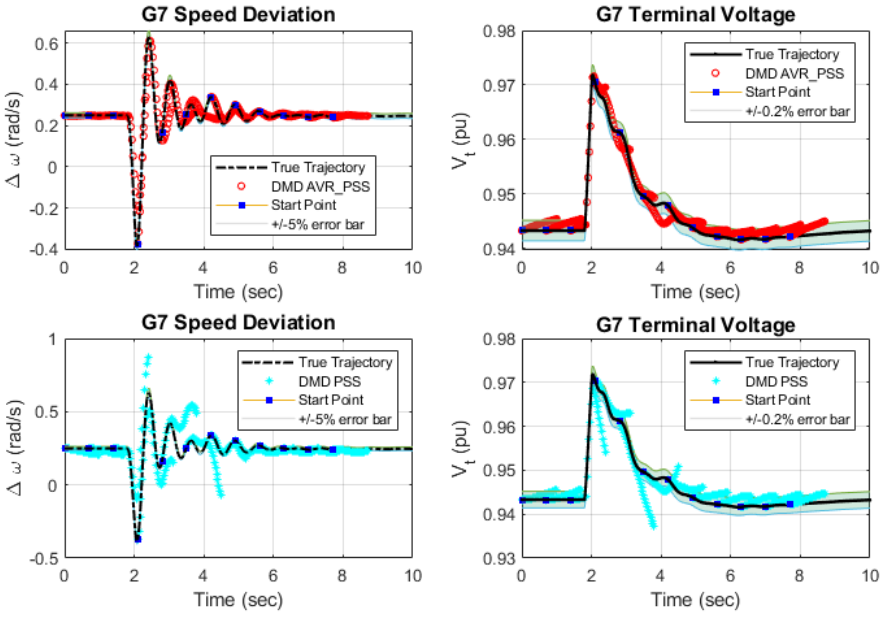

Figure 5 - 23 Multi-Step Trajectory Prediction of G7 in IEEE-39 Bus System

The cost function in (5-9) aims to damp the rotor speed oscillations and regulate the

terminal voltage to the given reference V_{ref} in the meanwhile. However, there exists a tradeoff between the two targets: strong damping of the rotor oscillations often makes the regulation time of the terminal voltage long; on the contrary, fast-tracking of the reference voltage brings significant oscillations to the rotor speed. In the proposed oscillation damping controller design, the two indexes are balanced by a weighted sum with penalty weights Q_ω, Q_V and R for the speed oscillations, voltage error, and control efforts, respectively. The optimization problem at each time step is convex quadratic since the system predictor in (5-10) is linear, allowing rapid solvers and thus making real-time control implementable. The speed deviation reference $\Delta\omega_{ref}$ is set as 0 when the system works under a normal condition with appropriate frequency control; or $\Delta\omega_{ref}$ can be selected as the center of inertia (COI) frequency in a large-scale power system. The compensation variable d_i is taken as constant in the prediction horizon of MPC. At each time step, d_0 is estimated by the multi-channel LESO according to the input and output from the last step.

5.5 Case Studies of the EKM-based Oscillation Damping Controllers

The proposed oscillation damping controller based on ESO-Koopman-MPC has been applied to SMIB, Kundur two-area system, and IEEE 39-bus system. Various scenarios are tested to compare the control performances of EKM-based controllers with CPSSs. The parameters of the proposed EKM-based controllers can be found in Appendix. EKM-based Damping Controller Parameters.

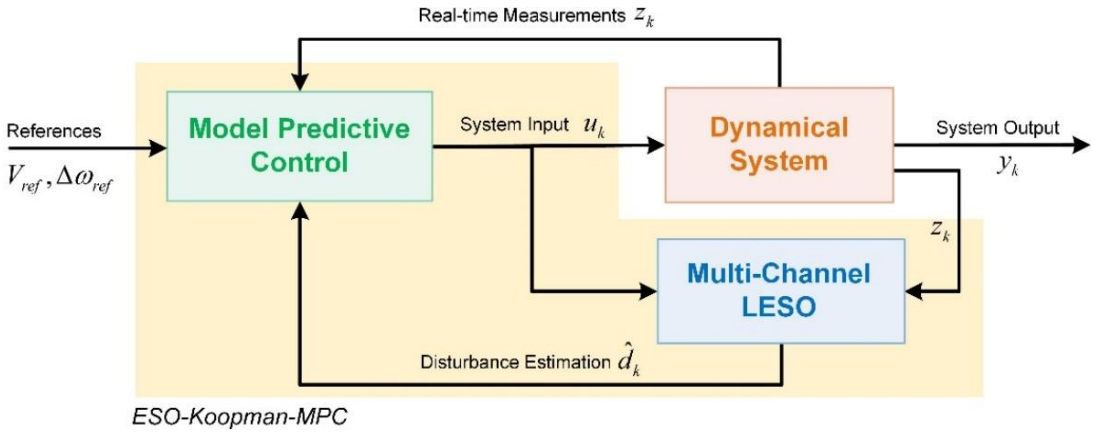

Figure 5 - 24 Schema of ESO-Koopman-MPC

5.5.1 Test Cases in SMIB: Simulation Results and Analysis

First, the control performances of the EKM-based damping controllers in terms of the two considered control strategies (EKM AVR&PSS and EKM PSS) are compared with the model-based CPSSs ($\Delta\omega$-PSS) in SMIB system. The dynamical trajectory without PSS is also presented as a comparison reference. All simulation results are shown from Figure 5-25 to Figure 5-28 for the test scenarios listed in subsection 5.3.1.

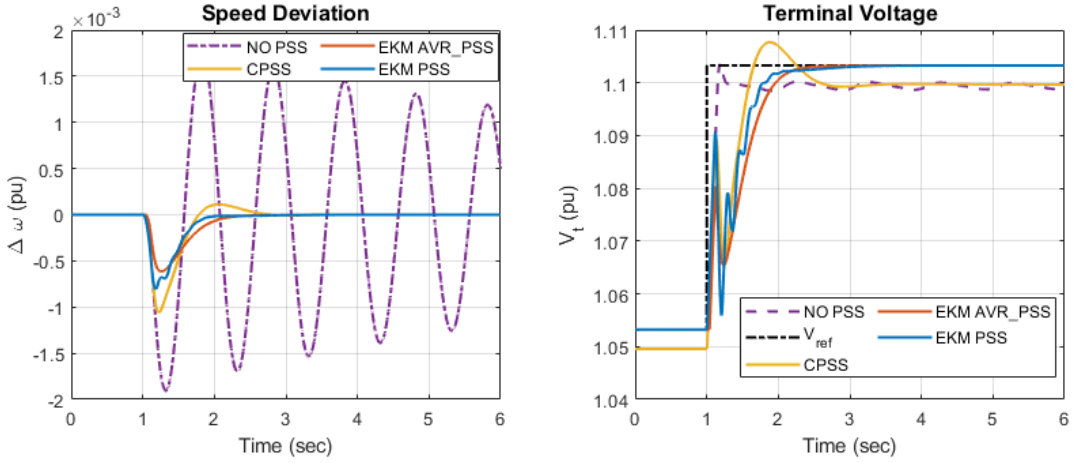

Figure 5 - 25 Voltage Reference Step Increase of 0.05 pu

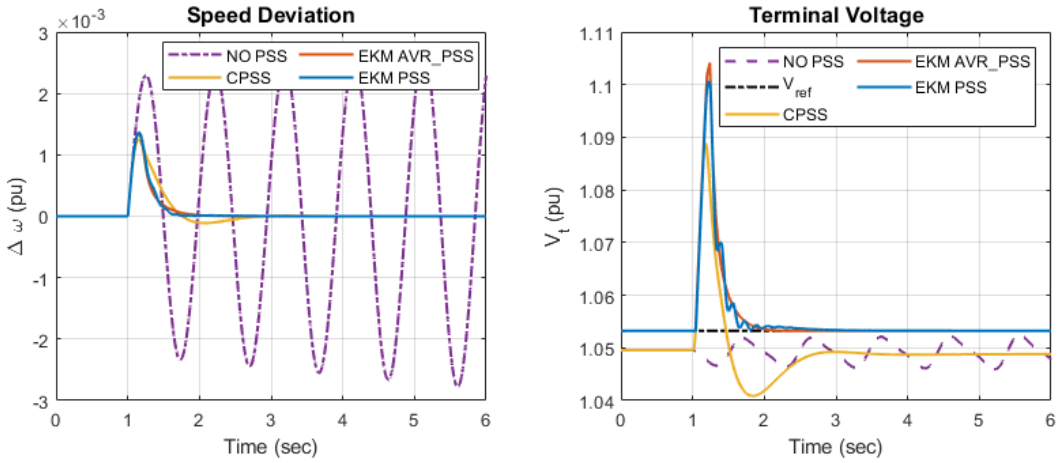

Figure 5 - 26 Mechanical Torque Step Increase of 0.1 pu

In Figure 5-25, EKM-based controllers yield better damping effects on the rotor speed with smaller oscillation amplitude. In addition, EKM-based controllers outperform CPSS on the terminal voltage regulation with no overshoots and zero tracking error, while CPSS displays a non-negligible offset before and after the voltage reference step change. Figure 5-26 corresponds to the case of mechanical torque T_m step increase of 0.1 pu at $t = 1s$. EKM-based controllers damp the rotor oscillations effectively with shorter settling time and regulate the terminal voltage with no steady-state offset and zero-undershoot.

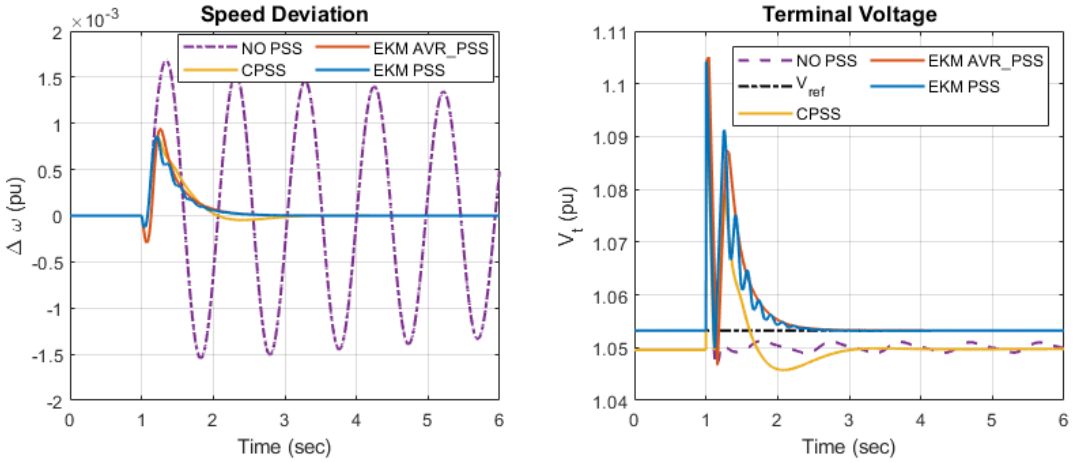

Figure 5 - 27 Infinite Bus Voltage Step Increase of 0.1 pu

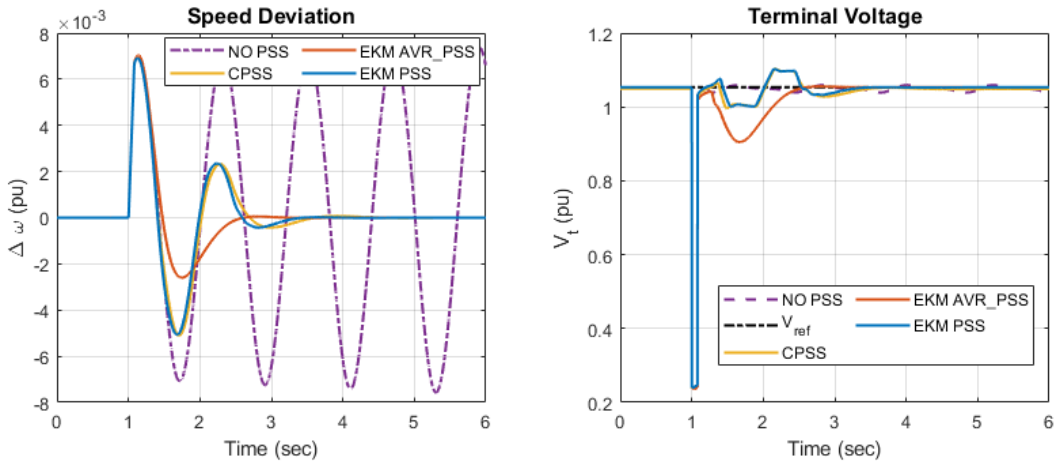

Figure 5 - 28 Three-phase Fault at One Transmission Line

Then, Figure 5-27 shows the control dynamics when a step increase of 0.1 pu occurs on the infinite bus voltage E_b. EKM-based damping controllers remain acceptable damping abilities, comparable to the CPSS. As to the terminal voltage regulation, EKM-based AVR & PSS has a smooth trajectory that restores the terminal voltage to the reference with no undershoot, no offset, and relatively short settling time. However, jittering exits for the control strategy of only PSS in the transient process. A possible solution is to apply magnitude limitations on the variation of the adjustable control signal V_{pss}.

The test case of the three-phase fault in Figure 5-28 is a more severe disturbance, and we can observe that EKM-based AVR & PSS has a significantly better damping performance than CPSS. In addition, the terminal voltage dynamics of EKM-based AVR & PSS show a larger drop at the first oscillation cycle while it can still restore the voltage to V_{ref} in a shorter settling time and zero offset (CPSS V_t offset: 0.0046 (pu)). The performance of EKM-based PSS is almost equivalent to CPSS because of the output limits on PSS. Consequently, the integration of AVR and PSS possesses more control flexibility since it is only subject to the AVR output limitations.

A more challenging event is illustrated in Figure 5-29 where we assume a mid-station at the middle point of the transmission lines, and a three-phase fault occurs at the sending end of one of the two transmission lines. The faulted line between the sending end and the mid-station is tripped after 10 cycles. In this scenario, only EKM-based integration of AVR and PSS can maintain the synchronism and stabilize the dynamical system. Besides, the terminal voltage can be restored to the reference value within 5 sec by the EKM-based AVR & PSS. On the other hand, CPSS and EKM-based PSS are not able to resume the system to the normal operation, and they have similar dynamics on the rotor speed as well as the terminal voltage, which is probably due to the strict magnitude limitations on the supplementary signal V_{pss} . Therefore, the EKM-based AVR & PSS has an enhanced damping ability to guarantee the reliable operation of power networks, especially when suffering severe disturbances.

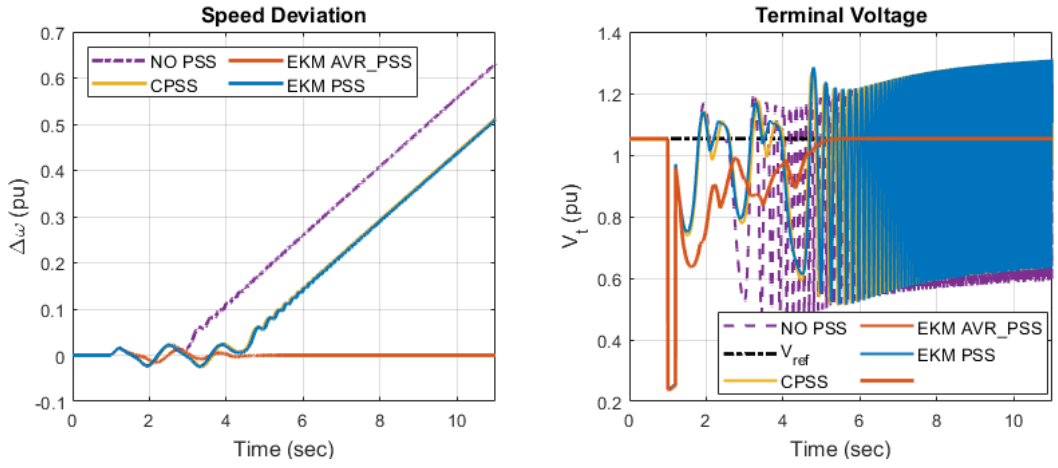

Figure 5 - 29 Three-Phase Fault with Mid-Station

5.5.2 Test Cases in Kundur Two-Area System: Simulation Results and Analysis

In this case, no frequency control is considered, and $\Delta\omega_{ref}$ is chosen as the rotor speed deviation of the reference generator (G4). G1 is equipped with EKM-based oscillation

damping controllers, while other generators have $\Delta\omega$-PSSs installed. The performances under various disturbances are compared with different kinds of CPSSs: multi-band PSS (MB-PSS), $\Delta\omega$-PSS, and the acceleration power PSS (ΔP_a-PSS); see subsection 5.1.3 for details.

Due to the symmetric structure, local oscillatory modes of the two areas have very close frequency (1.12Hz and 1.16Hz, respectively), and an inter-area mode of lower frequency (0.64Hz) is also observable in the tie-line transmitted active power. Well-designed PSSs are expected to effectively provide simultaneous damping on both the inter-area and local electromechanical oscillation modes. Four test cases are designed to study and compare the damping performances of the model-based and data-driven controller designs, which are listed below. The simulation results are presented in Figure 5-30 to Figure 5-33.

- Scenario 1: Voltage reference step increase on G1 (0.96 pu to 1.06 pu)
- Scenario 2: Voltage reference pulse change lasting for 12 cycles (magnitude randomly chosen in [-0.2, 0.2] pu) on G1
- Scenario 3: Three-phase fault occurred at the middle-point of one transmission line (bus 11 in Figure 5-18) and is cleared after 12 cycles. The faulted transmission line is tripped 8 cycles after the fault.
- Scenario 4: Load change lasting for 0.2s at area 1 (+10% of the original PQ load)

It is observed in Figure 5-30 that EKM-based AVR & PSS and PSS can damp out both the local and inter-area oscillations effectively. The data-driven oscillation damping controllers are superior to the model-based CPSSs with significantly damped oscillations and fewer fluctuation cycles on the rotor speed dynamics and the transmitted active power.

The generator terminal voltage can also be regulated well with almost no offset and no overshoot in a much shorter settling time than all CPSSs. Accordingly, EKM-based controller well solves the contradiction between the fast regulation and overshoot.

Fig. 5-31 corresponds to scenario 2 with a voltage reference pulse change 0.16629 pu) lasting for 12 cycles on G1. All CPSSs can restore the system in a short settling time while EKM-based AVR & PSS enjoys better performances with remarkably damped oscillations on both the local and inter-area oscillatory modes. Again, the terminal voltage is appropriately regulated back to the nominal value, and EKM-based AVR & PSS has the smallest overshoot. On the other hand, EKM-based PSS shows better damping effects on rotor speed oscillations than all CPSSs and almost equivalent performance on the tie-line active power to the best-performing CPSS (ΔP_a -PSS).

The study scenario in Figure 5-32 is a three-phase fault at the middle point (110km) of one transmission line with the faulted line tripped after 8 cycles. Under such a severe disturbance, G1 will lose step with the rest of the network without the supplementary control of PSS. The EKM-based controllers can effectively damp out local electromechanical oscillations and have better damping performances on the transmitted active power than CPSSs. Additionally, EKM-based controllers can restore the terminal voltage to the desired value in a much shorter settling time than the CPSSs. Figure 5-33 shows the test case with short-time load switching (12 cycles) at area 1. The load constituting the disturbance is 96.7MW/10MVAR/-18.7MVAR, about 10% of the original PQ load at the same spot. EKM-based controllers have better damping effects on the local and inter-area oscillations. The rotor speed deviation dynamics and transmitted active power at the tie-line are quite smooth with fewer fluctuations than CPSSs. Additionally,

EKM-based controllers can regulate the terminal voltage back to the nominal value.

To summarize, for all considered test scenarios in the Kundur two-area system, the two oscillation damping control strategies based on EKM can damp local and inter-area mode oscillations more effectively than CPSSs. Besides, the terminal voltage regulation performances of EKM-based controllers are superior to the CPSSs with almost no overshoot, no steady-state offset as well as short transition time.

5.5.3 Test Cases in IEEE-39 Bus System: Simulation Results and Analysis

Same as the case of the Kundur two-area system, the speed deviation reference $\Delta\omega_{ref}$ comes from the reference generator G1, which represents the New York power grid. Dynamical simulations are performed for the same test case in the report [97]: a three-phase fault at bus 16 in Figure 5-21, cleared after 10 cycles. The EKM-based controllers are deployed at G2 and G7 simultaneously, and all other generators are equipped with the conventional $\Delta\omega$-PSSs. The simulation results are presented in Figure 5-34 and 5-35 for G2 and G7 individually.

The simulation results demonstrate that EKM-based integration of AVR and PSS has notably improved damping effects on the rotor oscillations, observed in G2 and G7 with fewer oscillation cycles and smaller amplitudes, which makes the rotor speed dynamics much smoother compared to $\Delta\omega$-PSS. The damping performance of EKM-based PSS on the rotor speed is better than $\Delta\omega$-PSS in G7 while almost equivalent to CPSS in G2. All controllers can regulate the terminal voltages back to the nominal value, and EKM-based integration of AVR and PSS has the smallest overshoot and shortest settling time.

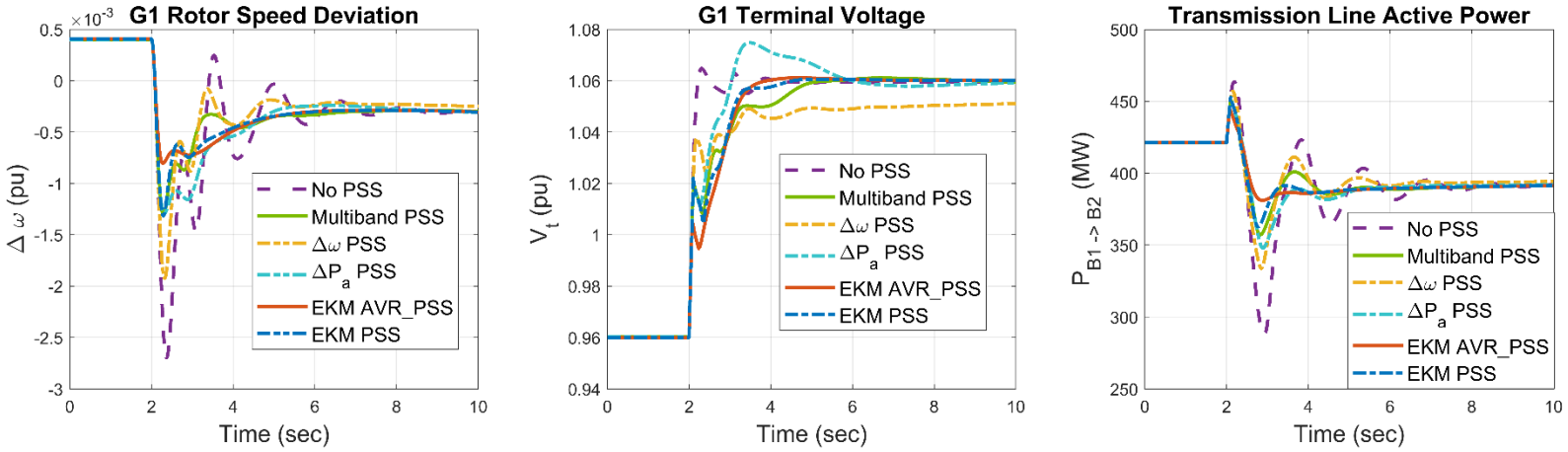

Figure 5 - 30 Kundur Two-Area System Scenario 1: Voltage Reference Step Increase on G1

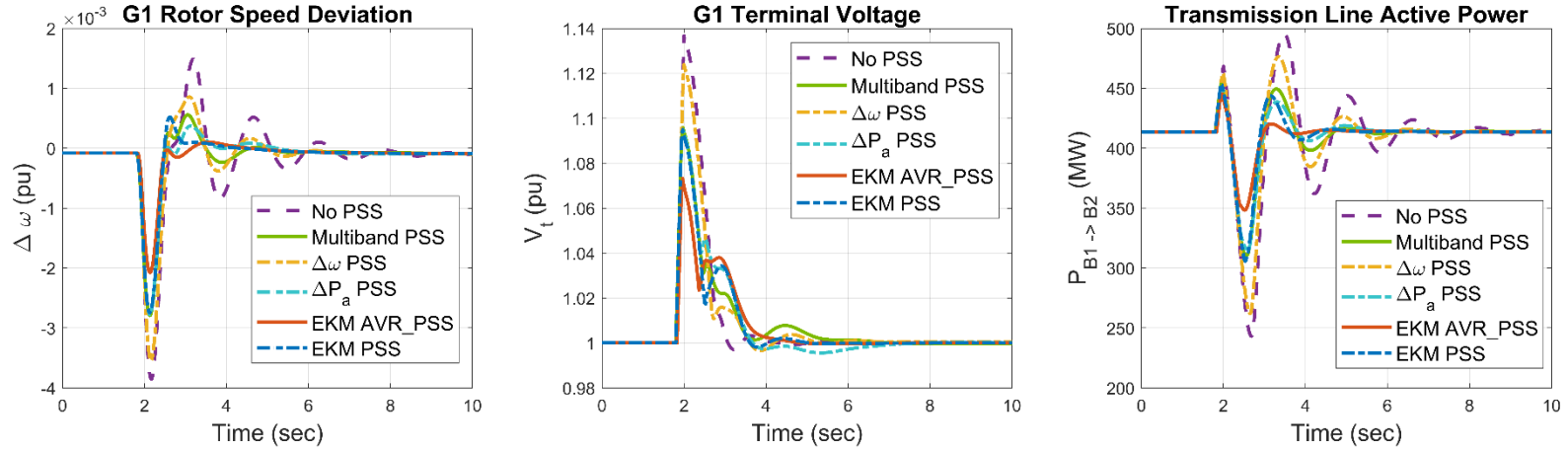

Figure 5 - 31 Kundur Two-Area System Scenario 2: Voltage Reference Pulse Change on G1

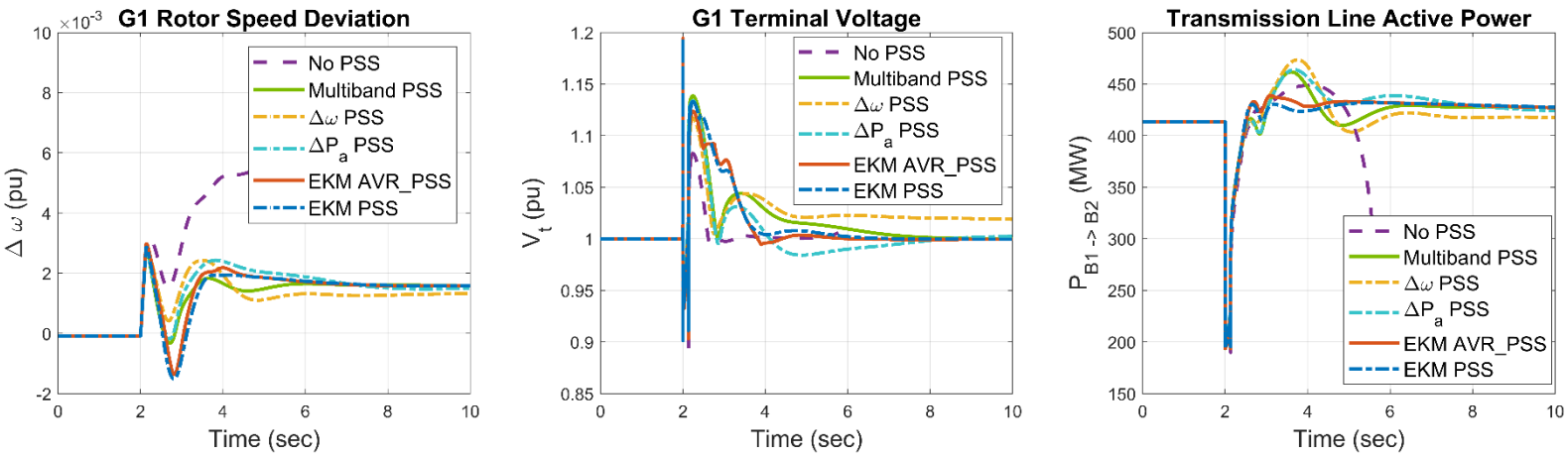

Figure 5 - 32 Kundur Two-Area System Scenario 3: Three-phase Fault on One Transmission Line

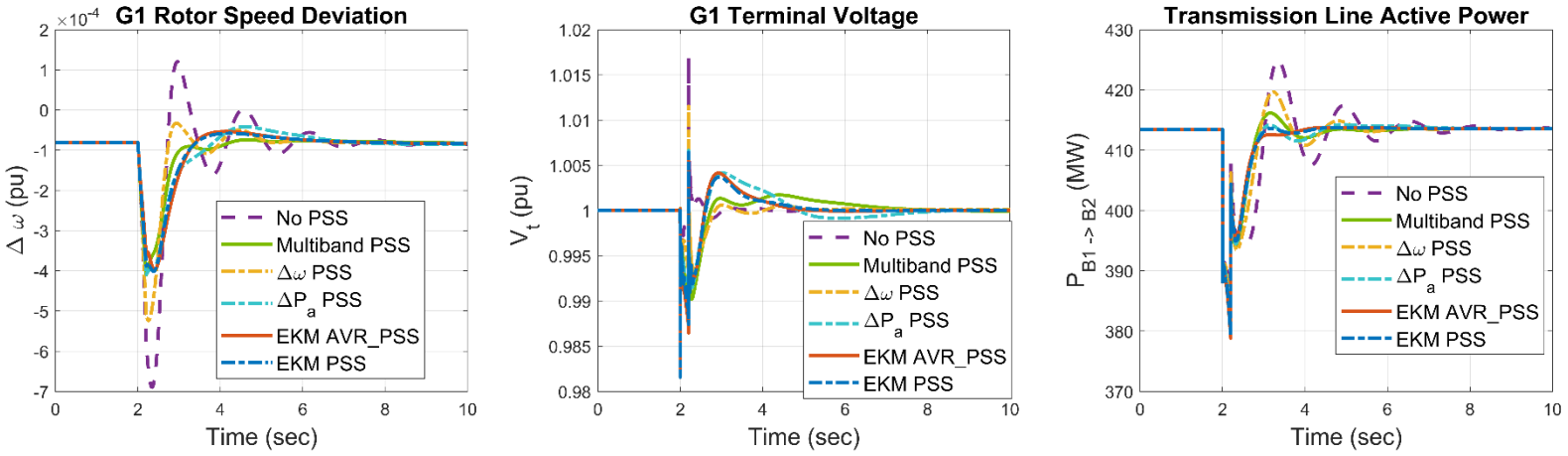

Figure 5 - 33 Kundur Two-Area System Scenario 4: Load Change at Area 1

5.6 The Effects of Multi-Channel ESO

The simulation studies in section 5.5 show that EKM-based controllers exhibit enhanced electromechanical oscillation damping ability compared with CPSSs on different platforms. Meanwhile, the voltage regulation dynamics display reduced or almost no overshoot and a shorter settling time. This section mainly studies the indispensability of the multi-channel ESO to remove the steady-state offsets, especially for the terminal voltage. The control performances with and without the assistance of a multi-channel ESO are presented, compared, and analyzed within a wide range of operating conditions.

First, a test case in SMIB is presented in Figure 5-36, which corresponds to the test scenario 1 in subsection 5.3.1. The voltage regulation performances of the EKM-based oscillation damping controllers without the multi-channel ESO are displayed (compare with Figure 5-25). As discussed before, the linear model identified based on the control strategy of only PSS has a higher modeling error. Thus, the voltage regulation dynamics show an obvious steady-state offset when this low-accuracy model is used in the MPC structure directly without the compensation from the multi-channel ESO.

To further analyze the function of multi-channel ESO, the real-time estimations of the modeling mismatch for the two considered control strategies are presented in Figure 5-37. The estimated values in all channels have rapid and significant variations when the disturbance (V_{ref} step change) occurs at $t = 1s$. For EKM AVR & PSS, the estimated modeling mismatches in different channels stay close to zero when the system becomes steady. Conversely, the ESO outputs for EKM PSS are relatively large (see channels 2~5). The estimated modeling error $\hat{d}(t)$ by the multi-channel ESO is then involved in the MPC predictive model and mitigated by being assumed constant in the prediction horizon.

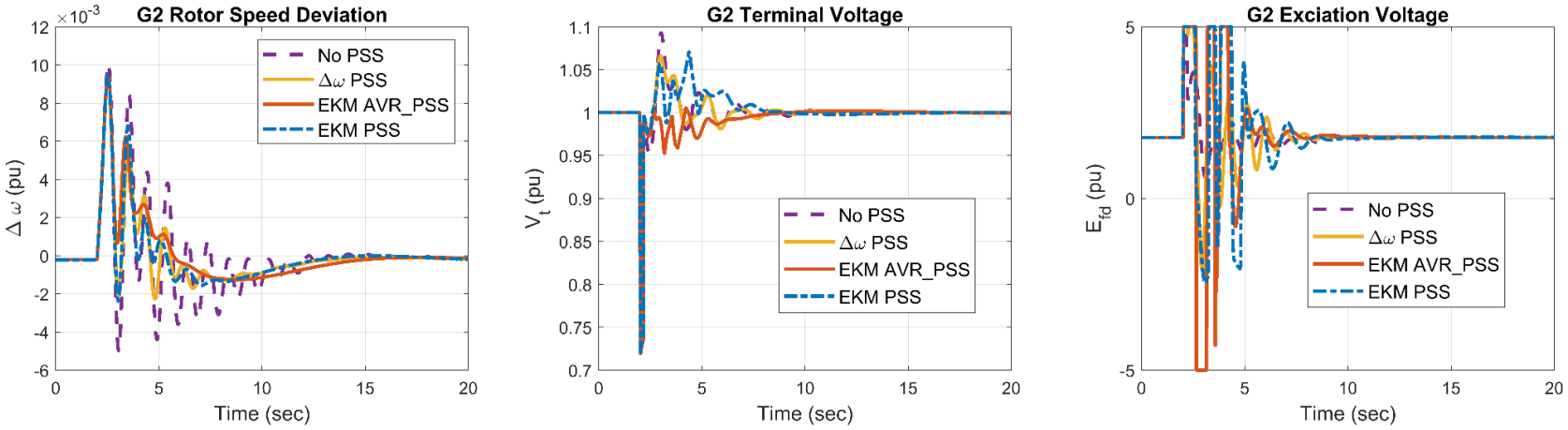

Figure 5 - 34 IEEE-39 Bus System G2: Three-phase Fault at Bus 16

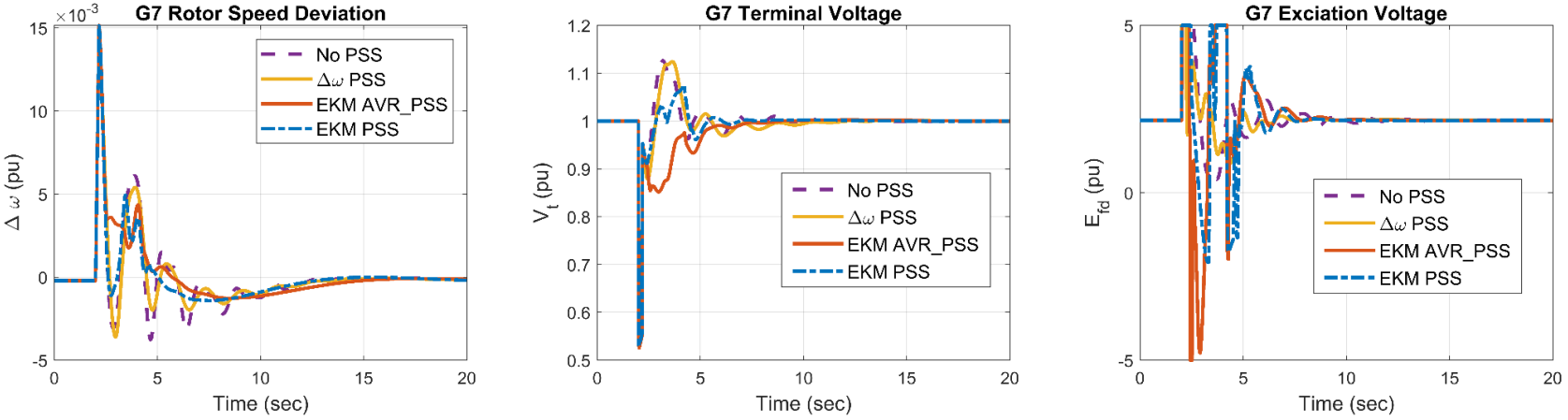

Figure 5 - 35 IEEE-39 Bus System G7: Three-phase Fault at Bus 16

In the multi-machine test platforms, the effects of the multi-channel ESO are checked in a wide range of operating conditions. For example, 100 randomly generated initial conditions are applied for all generators with $P_{ref} \in [0.1,1]$ and $V_{ref} \in [0.9,1.1]$ in Kundur two-area system. Some of the operating conditions may be impractical, they are used to check the voltage regulation performance. The test settings are the same as those in subsection 5.5.2, and we focus on the terminal voltage steady-state offsets with and without a multi-channel ESO. The performances of CPSSs are provided as comparison references. The simulation results are exhibited in Figure 5-38. It is worth noting that the voltage offsets among different CPSSs are the same.

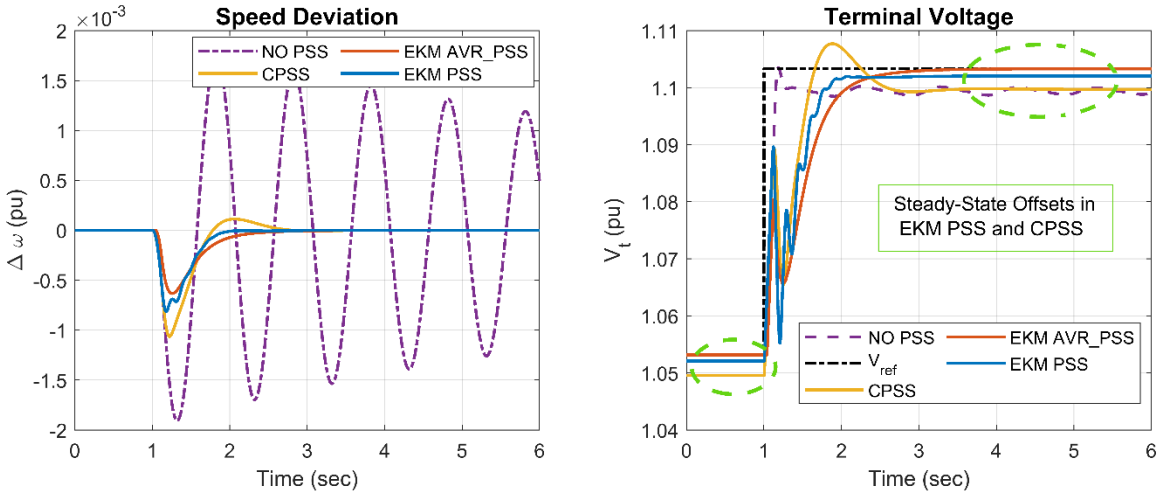

Figure 5 - 36 Voltage Reference Step Increase of 0.05 pu without Multi-Channel ESO

Secondly, we use the IEEE 39-bus system as the test system where G2 and G7 are equipped with various controllers at the same time. 100 random experiments are performed where the active power and voltage references of G2-10 are randomly selected from $P_{ref} \in [0.1,1]$ and $V_{ref} \in [0.9,1.1]$. The terminal voltage steady-state offsets of G2 and G7 are statistically summarized in Figure 5-39 and 5-40.

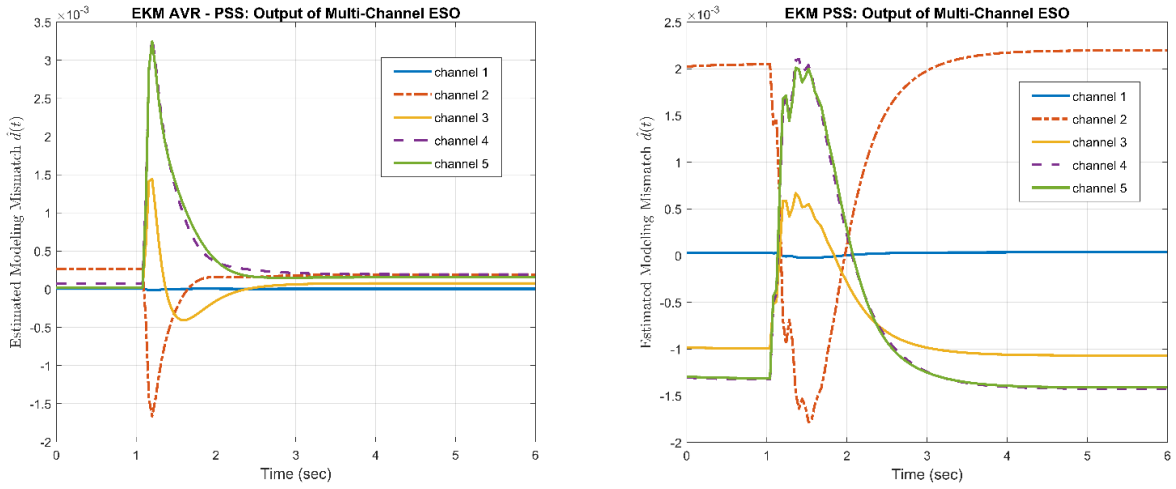

Figure 5 - 37 Multi-Channel ESO Outputs of EKM AVR & PSS and EKM PSS

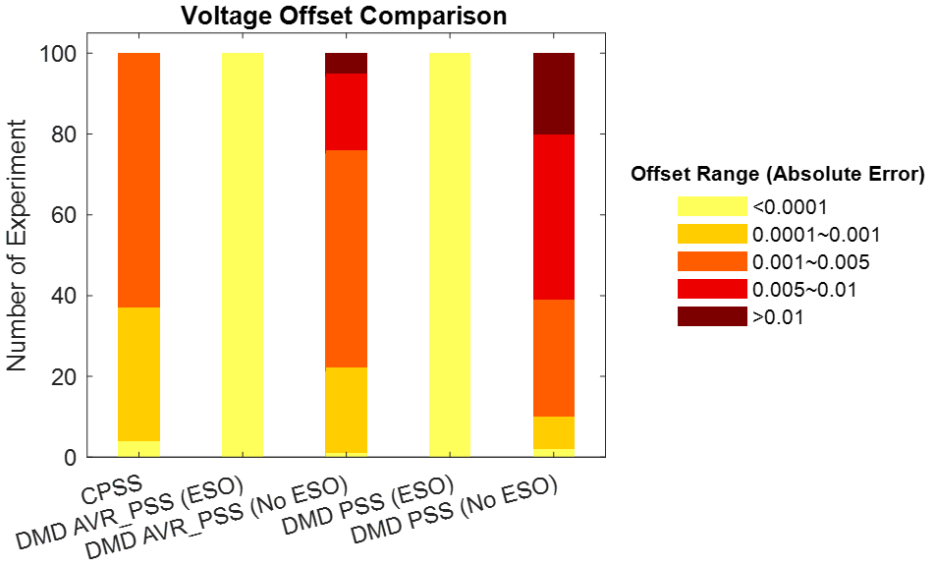

Figure 5 - 38 Terminal Voltage Offsets of G1 in Kundur Two-Area System

According to statistical summaries in Figure 5-39 and 5-40, the model-plant mismatch between the (linear) model identified via DMDc and the true dynamical system is detrimental to the performance of MPC. The mismatch may induce non-negligible terminal voltage steady-state offsets or even cause instabilities (out of step cases in IEEE-39 bus system). With the assistance of the multi-channel ESO, online estimation of the

discrepancy keeps updating the identified model and makes it adaptive in a wide range of operating conditions. In this way, the accuracy of the predictive model in the MPC optimization problem (5-10) is improved, and the proposed EKM-based oscillation damping controllers achieve enhanced robustness and exhibit a feature not shared by various CPSSs: zero-offset regulation of the terminal voltage.

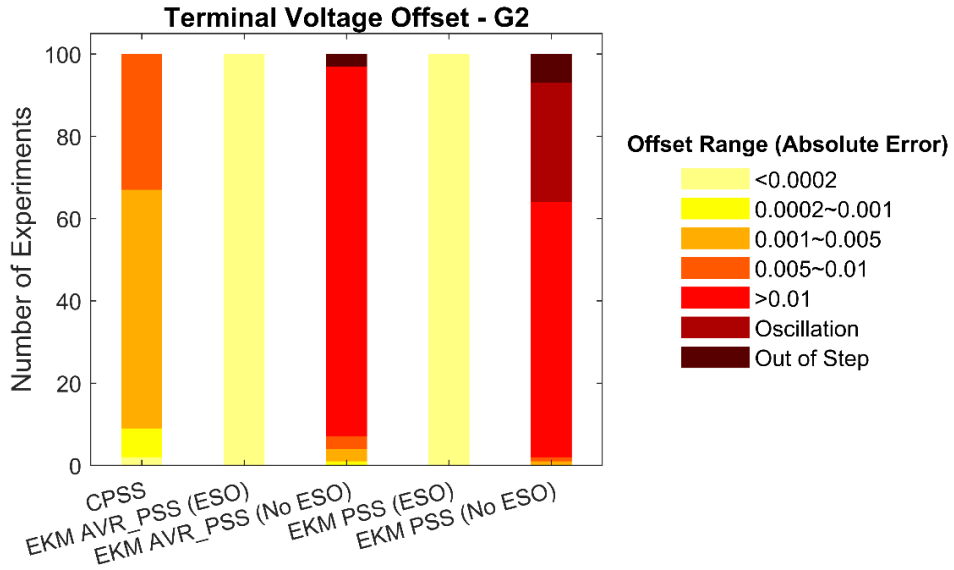

Figure 5 - 39 Terminal Voltage Offsets of G2 in IEEE-39 Bus System

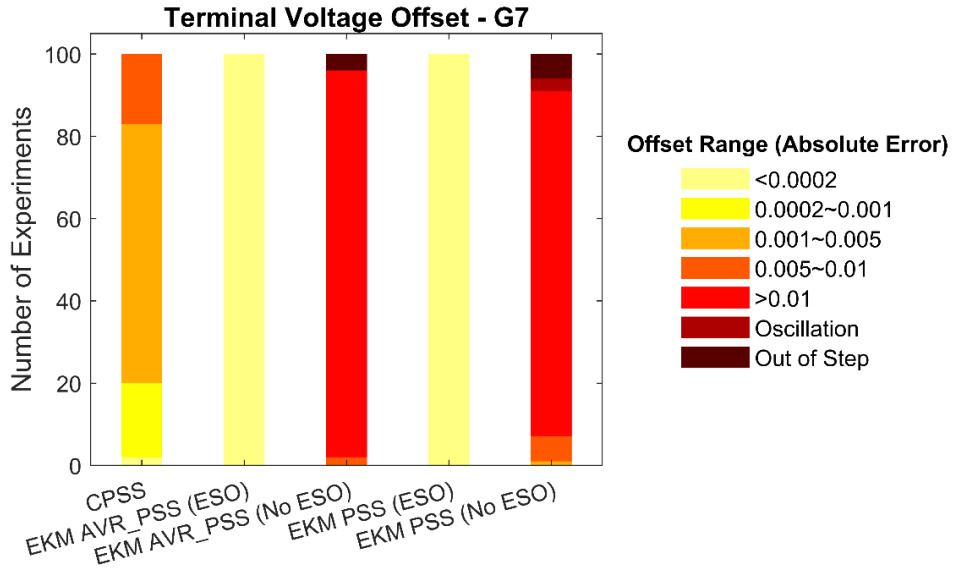

Figure 5 - 40 Terminal Voltage Offsets of G7 in IEEE-39 Bus System

5.7 EKM Summary: Real-time Implementation and Characteristics

In this section, we first evaluate the computational time required to solve the MPC optimization problem and ensure that the real-time implementations of the proposed damping controllers are allowed in practice. Secondly, some further analysis about the characteristics of the EKM-based oscillation damping controller design is performed.

5.7.1 Computational Time of the MPC Optimization Problem

One significant benefit of DMDc is the linearity of the identified model even when the underlying dynamical system is highly nonlinear, e.g., multi-machine power system networks. With a linear model embedded into the MPC structure and compensated by a multi-channel LESO, the optimization problem in (5-9, 5-10) is a (convex) quadratic programming problem, which is solved by an online active set strategy, qpOASES [98] in MATLAB R2020a, in our work. The simulations in this chapter are performed within the environment of Intel(R) Core(TM) i7-7700 CPU at 3.60 GHz with a 16 GB RAM and an ×64-based processor running Windows 10 Enterprise. Considering the requirement of real-time implementations, the computational time at each time step must be strictly limited, at least much smaller than the sampling period. The average computation time of the EKM-based controllers required to evaluate the control input on different test platforms is shown in Table 5-3. Clearly, the control action evaluation time is far shorter than the MPC control sampling period, and thus the online implementation of EKM-based damping controllers is realizable.

Table 5-3 Average Calculation Time of Control Input

Test Platform	SMIB	Kundur Two-Area	IEEE – 39 Bus	
			G2	G7
Evaluation Time	0.84ms	0.80ms	1.95ms	1.98ms
MPC Sampling Time	40ms	1/30s	1/30s	1/30s

5.7.2 Characteristics of the EKM Control Framework

- ***No Requirement of System Modeling***

A globally valid linear model is identified via DMDc from dynamical data without any mathematical modeling procedures of the studied system. On the stage of data collection, it does not matter which kind of CPSS is applied, even randomly generated E_{fd} or V_{pss} can work. What DMDc learned is not the control actions but the system dynamics. However, pre-known dynamics (if exist) should be leveraged in the system identification and the design of multi-channel ESOs.

- ***Distributed Architecture***

The design and operation of EKM-based controllers only depend on local measurements in (5-3), and a fully distributed architecture is formulated accordingly. The choice of system measurements is the foundation, and we believe the active and reactive power P_t, Q_t capture the influence of the external network on the controlled generator to some extent. Therefore, the interplay among all distributed controllers, system variations, or occurrence of emergency events is manifested in the terminal power flow P_t and Q_t. One indicative illustration of this property is the test case where a three-phase fault is cleared by tripping the faulted line. The system topology is changed afterward, but EKM-based

controllers still work properly even though the system dynamics are different from that on which the data acquisition is conducted.

- ***Low-order Model***

The order of the linear model learned by DMDc is equal to the number of observables and has nothing to do with the original order of the underlying dynamical system. Generally, the number of observables is far smaller than the intrinsic dimension of the real system. Such a low-order linear system embedded in MPC helps to reduce the computational burden further. In this work, the data-driven linear model used in MPC is only 5-th order (Eqn. (5-3) has 5 local measurements) even when the system underlying is a much higher-dimensional system, e.g., hundreds of dimensions for the IEEE-39 bus system.

- ***Adaptability***

The predictive model in MPC keeps being adaptively updated by the compensation from the multi-channel ESO according to the real-time system inputs and outputs measurements. The accuracy of the predictive model is thus improved, and the robustness of the controller is enhanced, especially when emergency events happen.

Chapter 6

Conclusion and Future Work

The proposition of the smart grid and the development of internet and communication technology (ICT) herald a new era of big data in power systems. Data-driven discovery is now revolutionizing how we model, predict, and control this cyber-physical system (CPS). With the high share of renewable energy resources (RESs) and other unpredictable system variations, the power system modeling is made progressively more challenging in the industrial practice. Therefore, the model-based viewpoint of controller design is not amenable to such a nonlinear and high-dimensional dynamical system with multi-scale characteristics in time and space. The availability of vast and increasing quantities of data in modern power systems drives the control paradigm to data-driven approaches.

This dissertation works to build a data-driven control framework and designs power system oscillation damping controllers based on the proposed framework, ESO-Koopman-MPC (EKM). The control framework contains three key elements:

(1) the system identification via dynamic mode decomposition with control (DMDc),

(2) online estimation and compensation of the model-plant mismatch by the extended state observer (ESO) techniques, and

(3) a linear model predictive control (MPC) structure.

DMDc is a numerical approximation of the Koopman operator, and the system dynamics are extracted from system observable measurements and the applied control actions. The identified model is guaranteed to be linear and has a global validness. The quality and correctness of the identified model are investigated in terms of the prediction accuracy of system trajectories. The inevitable deviation between the prediction and true trajectory may result in significant oscillations or non-zero steady-state offsets if the raw model is embedded into MPC directly. In the power system oscillation damping controller design, the model-plant discrepancy may induce the voltage regulation offsets or even instabilities.

A component, referred to as multi-channel ESO, leveraging the identified dynamics via DMDc and the idea of standard ESO, is introduced to realize estimation of the model-plant mismatch in a real-time manner. The multi-channel ESO treats the discrepancy as an extended state and tries to estimate it based on the system inputs and outputs measurements. The estimated variable compensates the identified model, especially when external disturbances or any internal changes occur. The compensated model is incorporated into the MPC structure, and owing to the assistance of ESO, the predictive model keeps being adaptively updated according to the system measurements. Therefore, the prediction accuracy is improved, and the stability and dynamic performances of the data-driven controllers are enhanced.

The EKM-based oscillation damping controller in power systems has two goals:

(1) damping of long-time persisting oscillations in the rotor speed and power flows, and

(2) regulation of the generator terminal voltage.

Accordingly, two control strategies are considered in this dissertation:

(1) integration of automatic voltage regulator (AVR) and power system stabilizer (PSS),

(2) only PSS.

The control goals are realized in the objective function of MPC by a weighted sum. The proposed data-driven oscillation damping controller only relies on the local measurements, and in this sense, a fully distributed control architecture is formulated. Owing to the linearity of the Koopman operator, the MPC optimization is a (convex) quadratic programming problem and allows rapid solvers to be applied. Besides, the dimensionality of the identified system has nothing related to the underlying complicated dynamical system but is equal to the number of selected measurements. Overall, the convexity and low-dimension guarantee the reduced computational burden, control stability, and real-time implementations.

The proposed data-driven oscillation damping controller and the model-based conventional PSS (CPSS) are tested and compared on different-scale test platforms recommended by the IEEE Force, such as the single machine infinite bus system (SMIB), Kundur two-area system, and the IEEE-39 bus system. The simulation results verify that the data-driven controllers present enhanced oscillation damping effects in terms of multiple oscillation modes. The control strategy of integration of AVR and PSS shows superior damping performance to the strategy of just PSS since the integration of AVR and PSS has more control flexibility. On the other side, the terminal voltage regulation performances of the data-driven controllers are checked in a wide range of operating conditions. The simulation results demonstrate that the EKM-based controllers exhibit a feature not shared by CPSSs: zero-offset regulation of the terminal voltage.

Finally, some directions for future work are listed below:

- Perform tests on larger power systems and check the oscillation damping performances

when multiple generators are equipped with the EKM-based damping controllers simultaneously (competition effects).

- Apply other Koopman approximation numerical methods when identification based on DMDc is not accurate enough, e.g., EDMDc, neural network-based EDMDc, etc.
- Search minimal and optimal measurements set for the data-driven dynamics discovery.
- Investigate other potential applications of the proposed control framework EKM.

Appendix

Table Appendix-1 SMIB Parameters

Generator:	$R_a = 0.00327$	$x_d = 1.7572$	$x_q = 1.5845$	$H = 3.542$	$D = 0$
	$x_d^{'} = 0.4245$	$x_q^{'} = 1.04$	$T_{d0}^{'} = 6.66$	$T_{q0}^{'} = 0.44$	
Transformer:	$R_t = 0.0$	$x_t = 0.1364$			
Transmission Line:	$R_l = 0.08593$	$x_l = 0.8125$	$B_c = 0.1184$	(per circuit)	

(The transmission line parameters are representative of a 400 kV, 400 km long line with 50% shunt compensation)

Excitation System:	$K_A = 400$	$T_A = 0.025$	$E_{fd,\max} = 6, E_{fd,\min} = -6$	
$\Delta\omega$ *-PSS:*	$K = 15$	$T_1 = 0.75$	$T_2 = 0.3$	$T_w = 10$
	$V_{pss,\max} = 0.05, V_{pss,\min} = -0.05$			

Other Parameters: $x_{th} = 0.13636$ (Thevenin's impedance of the receiving end system)

Test Initial Condition: $E_b = 1.0$ $P_t = 0.6$ $Q_t = 0.02224$ $V_t = 1.05$ $\theta = 21.65^{\circ}$

* Terminal Voltage: $V_t \angle \theta$

Table Appendix-2 EKM-based Damping Controller Parameters

		Controller	N_p	Q_ω	Q_V	R	T_c *(sec)*	Ω_0
SMIB		EKM-AP	10	15	500	0.001	1/25	0.6
		EKM-PSS	8	15	600	0.001	1/25	0.8
Kundur Two-Area System		EKM-AP	10	15	2000	0.001	1/30	0.8
		EKM-PSS	10	15	5000	0.01	1/30	0.8
IEEE-39 Bus System	**Gen 2**	EKM-AP	27	20	2500	0.005	1/30	0.8
		EKM-PSS	27	25	4500	0.01	1/30	0.8
	Gen 7	EKM-AP	27	30	1500	0.005	1/30	0.8
		EKM-PSS	27	25	2500	0.01	1/30	0.8

* EKM-AP : EKM-based Integration of AVR & PSS

* EKM-PSS: EKM-based PSS

Bibliography

[1] Zhu, Ting, Sheng Xiao, Qingquan Zhang, Yu Gu, Ping Yi, and Yanhua Li. "Emergent technologies in big data sensing: a survey." International Journal of Distributed Sensor Networks 11, no. 10 (2015): 902982.

[2] Zhang, Yang, Tao Huang, and Ettore Francesco Bompard. "Big data analytics in smart grids: a review." Energy informatics 1, no. 1 (2018): 1-24.

[3] Han, Wenjie, Gang Wang, and Alex M. Stankovic. "Active disturbance rejection control in fully distributed automatic generation control with co-simulation of communication delay." Control Engineering Practice 85 (2019): 225-234.

[4] Mishra, Debi Prasad, Subhransu Ranjan Samantaray, and Geza Joos. "A combined wavelet and data-mining based intelligent protection scheme for microgrid." IEEE Transactions on Smart Grid 7, no. 5 (2015): 2295-2304.

[5] Kar, Susmita, S. R. Samantaray, and M. Dadash Zadeh. "Data-mining model based intelligent differential microgrid protection scheme." IEEE Systems Journal 11, no. 2 (2015): 1161-1169.

[6] Hashemi, Farid, Mohammad Mohammadi, and Amin Kargarian. "Islanding detection method for microgrid based on extracted features from differential transient rate of change of frequency." IET Generation, Transmission & Distribution 11, no. 4 (2017): 891-904.

[7] De Santis, Enrico, Lorenzo Livi, Alireza Sadeghian, and Antonello Rizzi. "Modeling and recognition of smart grid faults by a combined approach of dissimilarity learning and one-class classification." Neurocomputing 170 (2015): 368-383.

[8] Zhang, Yuchen, Yan Xu, Zhao Yang Dong, Zhao Xu, and Kit Po Wong. "Intelligent early warning of power system dynamic insecurity risk: Toward optimal accuracy-earliness tradeoff." IEEE Transactions on Industrial Informatics 13, no. 5 (2017): 2544-2554.

[9] Susuki, Yoshihiko, and Igor Mezić. "Nonlinear Koopman modes and power system stability assessment without models." IEEE Transactions on Power Systems 29, no. 2 (2013): 899-907.

[10] Dimitrovska, Teodora, Urban Rudež, and Rafael Mihalič. "Fast contingency screening based on data mining." In IEEE EUROCON 2017-17th International Conference on Smart Technologies, pp. 794-798. IEEE, 2017.

[11] Papadopoulos, Panagiotis N., Tingyan Guo, and Jovica V. Milanović. "Probabilistic framework for online identification of dynamic behavior of power systems with renewable generation." IEEE Transactions on Power Systems 33, no. 1 (2017): 45-54.

[12] Netto, Marcos, and Lamine Mili. "A robust data-driven Koopman Kalman filter for power systems dynamic state estimation." IEEE Transactions on Power Systems 33, no. 6 (2018): 7228-7237.

[13] Balouji, Ebrahim, and Ozgul Salor. "Classification of power quality events using deep learning on event images." In 2017 3rd International Conference on Pattern Recognition and Image Analysis (IPRIA), pp. 216-221. IEEE, 2017.

[14] Kekatos, Vassilis, Georgios B. Giannakis, and Ross Baldick. "Grid topology identification using electricity prices." In 2014 IEEE PES general meeting| conference & exposition, pp. 1-5. IEEE, 2014.

[15] Wu, Wenbin, and Mugen Peng. "A data mining approach combining $ k $-means clustering with bagging neural network for short-term wind power forecasting." IEEE

Internet of Things Journal 4, no. 4 (2017): 979-986.

[16] Kong, Weicong, Zhao Yang Dong, Youwei Jia, David J. Hill, Yan Xu, and Yuan Zhang. "Short-term residential load forecasting based on LSTM recurrent neural network." IEEE Transactions on Smart Grid 10, no. 1 (2017): 841-851.

[17] https://www.theiet.org/media/1289/pnjv-1-15.pdf

[18] Han, Wenjie and Alex M. Stankovic. " Koopman Model Predictive Control-based Power System Stabilizer Design." In 2020 North American Power Symposium (NAPS), pp. 1-6. IEEE, 2021.

[19] Han, Wenjie and Alex M. Stankovic. " A Data-Driven Model-Predictive Control Design for Power System Oscillation Damping.", submitted to IEEE transactions on Power Systems.

[20] Han, Wenjie, Gang Wang, and Alex M. Stankovic. "Application of ultra-local models in automatic generation control with co-simulation of communication delay." In 2017 North American Power Symposium (NAPS), pp. 1-6. IEEE, 2017.

[21] Koopman, Bernard O. "Hamiltonian systems and transformation in Hilbert space." Proceedings of the national academy of sciences of the united states of america 17, no. 5 (1931): 315.

[22] Neumann, J. V. "Proof of the quasi-ergodic hypothesis." Proceedings of the National Academy of Sciences 18, no. 1 (1932): 70-82.

[23] Mezić, Igor. "Spectral properties of dynamical systems, model reduction and decompositions." Nonlinear Dynamics 41, no. 1 (2005): 309-325.

[24] Mauroy, Alexandre, Y. Susuki, and I. Mezić. The Koopman Operator in Systems and Control. Springer, 2020.

[25] Mezić, Igor. "Spectrum of the Koopman operator, spectral expansions in functional spaces, and state-space geometry." Journal of Nonlinear Science (2019): 1-55.

[26] Brunton, Steven L., and J. Nathan Kutz. Data-driven science and engineering: Machine learning, dynamical systems, and control. Cambridge University Press, 2019.

[27] Lusch, Bethany, J. Nathan Kutz, and Steven L. Brunton. "Deep learning for universal linear embeddings of nonlinear dynamics." Nature communications 9, no. 1 (2018): 1-10.

[28] Schmid, Peter J. "Dynamic mode decomposition of numerical and experimental data." Journal of fluid mechanics 656 (2010): 5-28.

[29] Williams, Matthew O., Ioannis G. Kevrekidis, and Clarence W. Rowley. "A data–driven approximation of the koopman operator: Extending dynamic mode decomposition." Journal of Nonlinear Science 25, no. 6 (2015): 1307-1346.

[30] Takeishi, Naoya, Yoshinobu Kawahara, and Takehisa Yairi. "Learning Koopman invariant subspaces for dynamic mode decomposition." arXiv preprint arXiv:1710.04340 (2017).

[31] Mezic, I., 2020. On numerical approximations of the koopman operator. arXiv preprint arXiv:2009.05883.

[32] Mezić, Igor. "Analysis of fluid flows via spectral properties of the Koopman operator." Annual Review of Fluid Mechanics 45 (2013): 357-378.

[33] Arbabi, Hassan. "Introduction to Koopman operator theory of dynamical systems." (2018).

[34] Rowley, Clarence W., I. G. O. R. MEZI?, Shervin Bagheri, Philipp Schlatter, and Dans Henningson. "Spectral analysis of nonlinear flows." Journal of fluid mechanics 641, no. 1 (2009): 115-127.

[35] Susuki, Yoshihiko, and Igor Mezić. "A prony approximation of Koopman mode decomposition." In 2015 54th ieee conference on decision and control (cdc), pp. 7022-7027. IEEE, 2015.

[36] Takens, Floris. "Detecting strange attractors in turbulence." In Dynamical systems and turbulence, Warwick 1980, pp. 366-381. Springer, Berlin, Heidelberg, 1981.

[37] Proctor, Joshua L., Steven L. Brunton, and J. Nathan Kutz. "Dynamic mode decomposition with control." SIAM Journal on Applied Dynamical Systems 15, no. 1 (2016): 142-161.

[38] Eckart, Carl, and Gale Young. "The approximation of one matrix by another of lower rank." Psychometrika 1, no. 3 (1936): 211-218.

[39] Tu, Jonathan H., Clarence W. Rowley, Dirk M. Luchtenburg, Steven L. Brunton, and J. Nathan Kutz. "On dynamic mode decomposition: Theory and applications." arXiv preprint arXiv:1312.0041 (2013).

[40] Han, J. Q. (1995). The extended state observer of a class of uncertain systems. Control and decision, 10(1), 85-88.

[41] 韩京清. 自抗扰控制技术: 估计补偿不确定因素的控制技术. 国防工业出版社, 2008 (in Chinese).

[42] Luenberger, David G. "Observing the state of a linear system." IEEE transactions on military electronics 8, no. 2 (1964): 74-80.

[43] Khalil, Hassan K. "High-gain observers in nonlinear feedback control." In 2008 International conference on control, automation and systems, pp. xlvii-lvii. IEEE, 2008.

[44] Han, Jingqing. "From PID to active disturbance rejection control." IEEE transactions on Industrial Electronics 56, no. 3 (2009): 900-906.

[45] Radke, Aaron, and Zhiqiang Gao. "A survey of state and disturbance observers for practitioners." In 2006 American Control Conference, pp. 6-pp. IEEE, 2006.

[46] Franklin, Gene F., J. David Powell, and Michael L. Workman. Digital control of dynamic systems. Vol. 3. Reading, MA: Addison-wesley, 1998.

[47] Umeno, Takaji, and Yoichi Hori. "Robust speed control of DC servomotors using modern two degrees-of-freedom controller design." IEEE Transactions on industrial electronics 38, no. 5 (1991): 363-368.

[48] Schrijver, Erwin, and Johannes Van Dijk. "Disturbance observers for rigid mechanical systems: equivalence, stability, and design." J. Dyn. Sys., Meas., Control 124, no. 4 (2002): 539-548.

[49] Miklosovic, Robert, Aaron Radke, and Zhiqiang Gao. "Discrete implementation and generalization of the extended state observer." In 2006 American Control Conference, pp. 6-pp. IEEE, 2006.

[50] Miklosovic, Robert, and Zhiqiang Gao. "A dynamic decoupling method for controlling high performance turbofan engines." IFAC Proceedings Volumes 38, no. 1 (2005): 532-537.

[51] Huang, Yi, Kekang Xu, Jingqing Han, and James Lam. "Flight control design using extended state observer and non-smooth feedback." In Proceedings of the 40th IEEE Conference on Decision and Control (Cat. No. 01CH37228), vol. 1, pp. 223-228. IEEE, 2001.

[52] Xu, Zhuang, Tianru Zhang, Yuli Bao, He Zhang, and Chris Gerada. "A nonlinear extended state observer for rotor position and speed estimation for sensorless IPMSM drives." IEEE Transactions on Power Electronics 35, no. 1 (2019): 733-743.

[53] Gao, Zhiqiang. "Scaling and bandwidth-parameterization based controller tuning." In Proceedings of the American control conference, vol. 6, pp. 4989-4996. 2006.

[54] Gao, Zhiqiang. "Active disturbance rejection control: a paradigm shift in feedback control system design." In 2006 American control conference, pp. 7-pp. IEEE, 2006.

[55] Garcia, Carlos E., David M. Prett, and Manfred Morari. "Model predictive control: Theory and practice—A survey." Automatica 25, no. 3 (1989): 335-348.

[56] Qin, S. Joe, and Thomas A. Badgwell. "An overview of nonlinear model predictive control applications." Nonlinear model predictive control (2000): 369-392.

[57] Allgower, Frank, Rolf Findeisen, and Zoltan K. Nagy. "Nonlinear model predictive control: From theory to application." Journal-Chinese Institute Of Chemical Engineers 35, no. 3 (2004): 299-316.

[58] Hedengren, John D., Reza Asgharzadeh Shishavan, Kody M. Powell, and Thomas F. Edgar. "Nonlinear modeling, estimation and predictive control in APMonitor." Computers & Chemical Engineering 70 (2014): 133-148.

[59] Ohtsuka, Toshiyuki. "A continuation/GMRES method for fast computation of nonlinear receding horizon control." Automatica 40, no. 4 (2004): 563-574.

[60] Kutz, J. Nathan, Steven L. Brunton, Bingni W. Brunton, and Joshua L. Proctor. Dynamic mode decomposition: data-driven modeling of complex systems. Society for Industrial and Applied Mathematics, 2016.

[61] Korda, Milan, and Igor Mezić. "Linear predictors for nonlinear dynamical systems: Koopman operator meets model predictive control." Automatica 93 (2018): 149-160.

[62] Wu, Chao, Kang Song, and Hui Xie. "Control of the common rail pressure in gasoline engines through an extended state observer based MPC." Control Theory and Technology

17, no. 2 (2019): 156-166.

[63] Shengquan, Li, Li Juan, Tang Yongwei, Shi Yanqiu, and Cao Wei. "Model-based model predictive control for a direct-driven permanent magnet synchronous generator with internal and external disturbances." Transactions of the Institute of Measurement and Control 42, no. 3 (2020): 586-597.

[64] Lv, Tong, Yanhua Yang, and Li Chai. "Extended state observer based MPC for a quadrotor helicopter subject to wind disturbances." In 2019 Chinese Control Conference (CCC), pp. 8206-8211. IEEE, 2019.

[65] Hou, Xiaoqiang, Ming Yue, Jian Zhao, and Xiaohua Zhang. "An ESO-based integrated trajectory tracking control for tractor–trailer vehicles with various constraints and physical limitations." International Journal of Systems Science 49, no. 15 (2018): 3202-3215.

[66] Liu, Chenguang, Rudy R. Negenborn, Huarong Zheng, and Xiumin Chu. "A state-compensation extended state observer for model predictive control." European Journal of Control 36 (2017): 1-9.

[67] Canizares, C., T. Fernandes, E. Geraldi, L. Gerin-Lajoie, M. Gibbard, I. Hiskens, J. Kersulis et al. "Benchmark models for the analysis and control of small-signal oscillatory dynamics in power systems." IEEE Transactions on Power Systems 32, no. 1 (2016): 715-722.

[68] Liu, Hui, Jinshuo Su, Yude Yang, Zhijun Qin, and Canbing Li. "Compatible Decentralized Control of AVR and PSS for Improving Power System Stability." IEEE Systems Journal (2020).

[69] Kundur, Prabha. "Power system stability." Power system stability and control (2007):

7-1.

[70] Rogers, Graham. Power system oscillations. Springer Science & Business Media, 2012.

[71] Ye, Hua, and Yutian Liu. "Design of model predictive controllers for adaptive damping of inter-area oscillations." International Journal of Electrical Power & Energy Systems 45, no. 1 (2013): 509-518.

[72] Qiu, Wenzheng, Vijay Vittal, and Mustafa Khammash. "Decentralized power system stabilizer design using linear parameter varying approach." IEEE Transactions on Power Systems 19, no. 4 (2004): 1951-1960.

[73] Prakash, Tapan, Vinay Pratap Singh, and Soumya R. Mohanty. "Cyber-attack resilient design of wide-area pss considering practical communication constraints." IEEE Systems Journal 14, no. 2 (2019): 2012-2022.

[74] Kosterev, Dmitry N., Carson W. Taylor, and William A. Mittelstadt. "Model validation for the August 10, 1996 WSCC system outage." IEEE transactions on power systems 14, no. 3 (1999): 967-979.

[75] Andersson, Göran, Peter Donalek, Richard Farmer, Nikos Hatziargyriou, Innocent Kamwa, Prabhashankar Kundur, Nelson Martins et al. "Causes of the 2003 major grid blackouts in North America and Europe, and recommended means to improve system dynamic performance." IEEE transactions on Power Systems 20, no. 4 (2005): 1922-1928.

[76] Padiyar, K. R. Power system dynamics: stability & control. BS publications, 2010.

[77] Elgerd, Olle I., and Charles E. Fosha. "Optimum megawatt-frequency control of multiarea electric energy systems." IEEE transactions on power apparatus and systems 4 (1970): 556-563.

[78] Obaid, Zeyad Assi, L. M. Cipcigan, and Mazin T. Muhssin. "Power system oscillations and control: Classifications and PSSs' design methods: A review." Renewable and Sustainable Energy Reviews 79 (2017): 839-849.

[79] Follum, James D., Francis K. Tuffner, Luke A. Dosiek, and John W. Pierre. Power system oscillatory behaviors: Sources, characteristics, & analyses. No. PNNL-26375. Pacific Northwest National Lab.(PNNL), Richland, WA (United States), 2017.

[80] IEEE Working Group. "IEEE Guide for Identification, Testing and Evaluation of the Dynamic Performance of Excitation Control Systems." IEEE Standard: 421-2.

[81] Cai, Deyu, Pawel Regulski, Mark Osborne, and V. Terzija. "Wide area inter-area oscillation monitoring using fast nonlinear estimation algorithm." IEEE Transactions on Smart Grid 4, no. 3 (2013): 1721-1731.

[82] Kamwa, I., R. Grondin, and G. Trudel. "IEEE PSS2B versus PSS4B: the limits of performance of modern power system stabilizers." IEEE transactions on power systems 20, no. 2 (2005): 903-915.

[83] Zhang, Y., G. P. Chen, O. Pr Malik, and G. S. Hope. "An artificial neural network based adaptive power system stabilizer." IEEE transactions on energy conversion 8, no. 1 (1993): 71-77.

[84] Segal, Ravi, Avdhesh Sharma, and M. L. Kothari. "A self-tuning power system stabilizer based on artificial neural network." International journal of electrical power & energy systems 26, no. 6 (2004): 423-430.

[85] Liu, Wenxin, Ganesh K. Venayagamoorthy, and Donald C. Wunsch. "Adaptive neural network based power system stabilizer design." In Proceedings of the International Joint Conference on Neural Networks, 2003., vol. 4, pp. 2970-2975. IEEE, 2003.

[86] El-Metwally, K. A., G. C. Hancock, and O. P. Malik. "Implementation of a fuzzy logic PSS using a micro-controller and experimental test results." IEEE transactions on energy conversion 11, no. 1 (1996): 91-96.

[87] Abido, M. A. "Robust design of multimachine power system stabilizers using simulated annealing." IEEE transactions on Energy conversion 15, no. 3 (2000): 297-304.

[88] de Vargas Fortes, Elenilson, Percival Bueno de Araujo, and Leonardo H. Macedo. "Coordinated tuning of the parameters of PI, PSS and POD controllers using a specialized chu–Beasley's genetic algorithm." Electric Power Systems Research 140 (2016): 708-721.

[89] Abido, M. A., and Y. L. Abdel-Magid. "Optimal design of power system stabilizers using evolutionary programming." IEEE Transactions on Energy Conversion 17, no. 4 (2002): 429-436.

[90] Abido, M. A. "Optimal design of power-system stabilizers using particle swarm optimization." IEEE transactions on energy conversion 17, no. 3 (2002): 406-413.

[91] Abido, M. A. "A novel approach to conventional power system stabilizer design using tabu search." International Journal of Electrical Power & Energy Systems 21, no. 6 (1999): 443-454.

[92] Jiang, Zhenhua. "Design of a nonlinear power system stabilizer using synergetic control theory." Electric Power Systems Research 79, no. 6 (2009): 855-862.

[93] Transtrum, Mark K., Andrija T. Sarić, and Aleksandar M. Stanković. "Information geometry approach to verification of dynamic models in power systems." IEEE Transactions on Power Systems 33, no. 1 (2017): 440-450.

[94] Ghahremani, Esmaeil, and Innocent Kamwa. "Local and wide-area PMU-based decentralized dynamic state estimation in multi-machine power systems." IEEE

Transactions on Power Systems 31, no. 1 (2015): 547-562.

[95] https://www.mathworks.com/help/physmod/sps/ug/performance-of-three-pss-for-interarea-oscillations.html;jsessionid=229cc2eb31c9d165e7ccacbbc8ed

[96] Moeini, A., I. Kamwa, P. Brunelle, and G. Sybille. "Open data IEEE test systems implemented in SimPowerSystems for education and research in power grid dynamics and control." In 2015 50th International Universities Power Engineering Conference (UPEC), pp. 1-6. IEEE, 2015.

[97] Hiskens, Ian. "IEEE PES task force on benchmark systems for stability controls." Technical Report (2013).

[98] Ferreau, Hans Joachim, Christian Kirches, Andreas Potschka, Hans Georg Bock, and Moritz Diehl. "qpOASES: A parametric active-set algorithm for quadratic programming." Mathematical Programming Computation 6, no. 4 (2014): 327-363.